# Receptivity of hypersonic boundary layers to kinetic fluctuations

by

Luke Edwards



A Dissertation Submitted to the Faculty of the

Graduate Interdisciplinary Program
in Applied Mathematics

In Partial Fulfillment of the Requirements
For the Degree of

Doctor of Philosophy

In the Graduate College

The University of Arizona

2 0 2 0

THE UNIVERSITY OF ARIZONA
GRADUATE COLLEGE

As members of the Dissertation Committee, we certify that we have read the dissertation prepared by: Luke Edwards
titled: Receptivity of Hypersonic Boundary Layers to Kinetic Fluctuations

and recommend that it be accepted as fulfilling the dissertation requirement for the Degree of Doctor of Philosophy.

Anatoli Tumin
Anatoli Tumin — Date: Dec 9, 2019

MoyseyBrio
MoyseyBrio — Date: Jan 2, 2020

Joceline Lega
Joceline Lega — Date: Dec 9, 2019

Karl Glasner
Karl Glasner — Date: Dec 9, 2019

Final approval and acceptance of this dissertation is contingent upon the candidate's submission of the final copies of the dissertation to the Graduate College.

I hereby certify that I have read this dissertation prepared under my direction and recommend that it be accepted as fulfilling the dissertation requirement.

Anatoli Tumin
Anatoli Tumin — Date: Dec 9, 2019
Anatoli Tumin

# Acknowledgments

Thanks are owed to many colleagues, mentors and friends for assistance, direct and indirect, in completing this dissertation. First and foremost, the guidance and support of my advisor, Anatoli Tumin, has been invaluable, and his good nature has helped ensure that I will look back on my graduate school years with fondness. I would also like to thank the other members of my committee, Moysey Brio, Joceline Lega, and Karl Glasner, all of whom have served as mentors or contributed to my growth as a scientist over the past several years. Finally, special thanks are owed to Alexander Fedorov and colleagues, whose research inspired and informed much of the work presented in this dissertation.

The support of the Program in Applied Mathematics has been essential throughout my time in Tucson. A substantial debt of gratitude is owed in particular to Stacey LaBorde for her tireless assistance on many fronts during my time in the program. This work was supported in part by the U.S. Air Force Office of Scientific Research and several teaching assistantships from the Department of Mathematics.

# Table of Contents

TABLE OF CONTENTS—*Continued*

# List of Figures

List of Figures—*Continued*

List of Figures—*Continued*

# Abstract

The receptivity of high-speed compressible boundary layers to kinetic fluctuations (KF) is considered within the framework of fluctuating hydrodynamics. The formulation is based on the idea that KF-induced dissipative fluxes can lead to the generation of unstable modes in the boundary layer. Using linear stability theory (LST) and a variety of asymptotic methods, the KF-receptivity problem is solved for a range of high-speed flat plate boundary layer configurations. Approaches for solving the KF-receptivity problem in cases where the dominant modes exhibit long scale near-neutral behavior or when two modes of the discrete spectrum coalesce are developed and explored in detail.

# Receptivity of hypersonic boundary layers to kinetic fluctuations

Luke Edwards, Ph.D.
The University of Arizona, 2020

Director: Anatoli Tumin

The receptivity of high-speed compressible boundary layers to kinetic fluctuations (KF) is considered within the framework of fluctuating hydrodynamics. The formulation is based on the idea that KF-induced dissipative fluxes can lead to the generation of unstable modes in the boundary layer. Using linear stability theory (LST) and a variety of asymptotic methods, the KF-receptivity problem is solved for a range of high-speed flat plate boundary layer configurations. Approaches for solving the KF-receptivity problem in cases where the dominant modes exhibit long scale near-neutral behavior or when two modes of the discrete spectrum coalesce are developed and explored in detail.

# Chapter 1

# Introduction

The development of a complete theory behind the transition of boundary layer flows from laminar to turbulent has been a decades long pursuit. Despite a substantial amount of progress, particularly towards understanding the intermediate stages prior to transition, a complete understanding of the process remains elusive. The difficulty is in large part due to the multitude of factors influencing the phenomenon, including environmental conditions and the details of the aerodynamic body. Reviews of the fundamental aspects of the problem can be found in Refs. [88, 83, 84, 74].

Much of the modern interest in understanding laminar-turbulent transition stems from the importance of the phenomenon in the design of aircraft traveling at hypersonic speeds, i.e. at a Mach number of five or greater. At high Mach numbers, a turbulent boundary layer is associated with a dramatic increase in the aerodynamic heating of the vehicle body. A cartoon of the boundary layer over a flat plate is provided in figure 1.1, along with the conventional labeling of the three-dimensional coordinate system. The coordinates $x, y$ and $z$ will be referred to as the streamwise, wall-normal, and span-wise coordinates throughout this work. The ability to predict the streamwise location along the surface of a body where the flow is likely

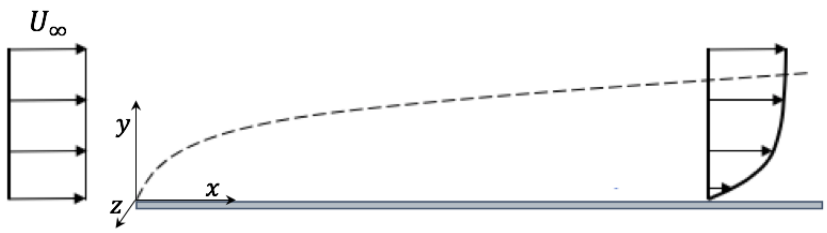


Figure 1.1. Cartoon of the boundary layer over a flat plate.

to be turbulent is critical for the efficient design of heat shields and flight control mechanisms.

The picture of the transition phenomenon that has developed over the last several decades is summarized in Figure 1.2, reproduced from any number of reviews on the topic [74, 105, 27]. A key principle is that the path to transition fundamentally depends on the type and level of disturbances present in the environment, either within the boundary layer or immediately external to it. These may include acoustic waves, vorticity and entropy perturbations, atmospheric particulates, wall vibrations or roughness, or, as will be discussed in this dissertation, kinetic fluctuations (also referred to as thermal noise). *Receptivity* is the mechanism by which environmental disturbances generate instability waves within the boundary layer [73, 111]. The diagram in Figure 1.2 indicates the possible paths to turbulent breakdown in boundary layers, with the level of forcing due to environmental factors increasing from left to right.

Because this work is primarily concerned with atmospheric flight and quiet wind tunnel conditions where disturbance levels are relatively low [98, 92, 95], we restrict our attention to path 'a'. In this scenario, boundary layer eigenmodes are excited via receptivity mechanisms by some forcing. Assuming their amplitudes are initially small, these modes undergo selective linear amplification as they propagate downstream. If the induced disturbances have space to become sufficiently amplified, non-linear effects begin to dominate and ultimately breakdown to transition occurs [27]. Nothing is said in the present work about stages of the transition phenomenon beyond the linear regime.

The approaches to studying the receptivity problem, and the problem of transition more generally, may be broadly classified as either experimental or theoretical. Experimental approaches may be either physical or computational, i.e. direct numerical simulation (DNS) [3, 21, 64, 65, 66, 103, 104], and have the advantage of incorporating all (or most) of the relevant physics. In the case of hypersonic flight, however, the

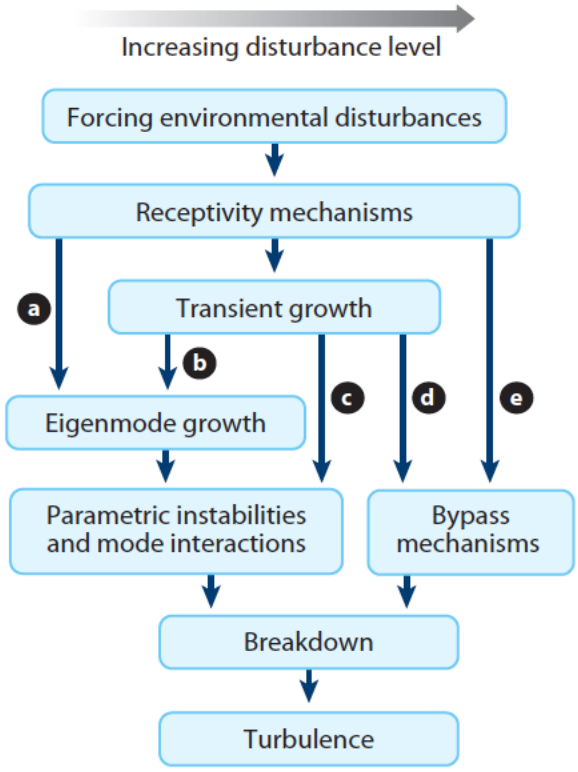


FIGURE 1.2. Paths to laminar-turbulent transition in a boundary layer, reproduced from Ref. [27]

situation is especially difficult. Refs. [92, 93, 94, 96] comprise a good summary of experimental results for both wind tunnel and atmospheric flight tests in the hypersonic regime over the last few decades. High Mach number wind-tunnel experiments may not be a good predictor of the transition phenomenon in atmospheric flight due to dramatic differences in the disturbance environment and flow conditions. Actual atmospheric flight tests are possible but come with price tags in the millions and require years of planning. Accurate and informative flow measurements are also difficult in such extreme conditions. Highly efficient theoretical approaches, which are able to provide a simplified view of the complex physics observed in experiment, are thus critical, particularly towards the goal of understanding transition in extremely high speed flows. Theoretical investigation exposes new features of receptivity mechanisms and helps guide the direction of and explain the results of experiments [27]. Empirical results in turn motivate new directions in theory and help validate theoretical results.

The work herein is primarily a coupling of asymptotic methods with linear stability theory (LST), the latter of which benefits from an extensive body of research [67, 68, 69, 89, 72, 70, 71, 82] and has been extensively validated through DNS [103, 103, 26] and experiment [98]. In recent decades, much attention has been given to the incorporation of receptivity analysis into the standard linear stability theory (LST) framework [30]. This is due to the potential for amplitude based methods [68, 30] to yield improved transition onset locus prediction compared to methods based on LST alone, i.e. the conventional $e^N$ method. The bulk of recent receptivity studies have focused on the excitation of unstable modes by free stream disturbances such as acoustic waves or vorticity and entropy perturbations [111, 107, 105, 37, 1, 2, 45, 44, 32, 33], wall-induced disturbances including roughness, vibration and blowing-suction [10, 35, 26], or interaction with other external elements such as atmospheric particulates [36, 29, 30].

The primary goal of this dissertation is to further the understanding of receptivity to kinetic fluctuations (KF), also referred to as thermal noise, in high speed boundary

layer flows. The idea that disorder on the molecular scale could excite boundary layer modes and ultimately lead to transition was first proposed by Betchov [6] in the 1960's. The relevant receptivity mechanisms were first explored quantitatively in low-speed boundary layers using asymptotic methods by Zavolskii and Reutov in 1984 [109]. More recently, the problem has been studied by Luchini [59, 58, 60, 61] in the context of low-speed incompressible boundary layers, and by Fedorov and Averkin [31], Fedorov [30], and Fedorov and Tumin [39], in connection to high speed transition.

Due to the magnitude of the initial disturbances induced by thermal noise, it is not possible to validate KF-receptivity calculations directly using currently available instrumentation. It is also challenging in any particular experiment to rule out the presence of other environmental disturbances that could play a role in the transition phenomenon, particularly in atmospheric flight tests where thorough measurement of the flow is not possible. However, correlations between transition locations observed empirically and those predicted theoretically provide compelling indirect evidence [30]. As an example, Ref. [30] showed that vorticity and entropy perturbations as well as atmospheric particulates could both be ruled out as likely causes of transition for the HIFiRE-1 flight test [56]. KF-induced transition was proposed as an alternative explanation, and indeed, analysis of the flight configuration showed that the theoretically predicted KF-induced transition onset locus was not far from the experimentally observed location. Through similar means, the KF-receptivity mechanism has also been shown to be relevant at other flight conditions [39]. Analysis of experimental data in the Langley Mach 3.5 quiet wind tunnel indicates that KF could also play a role in triggering laminar-turbulent transition at quiet flow conditions in a wind tunnel [28]. Importantly, due to the indispensable nature of thermal noise in any environment of practical interest, the theoretically predicted KF-induced transition location can be usefully thought of as an upper bound beyond which transition cannot be avoided [60]. Thus, there is value in developing robust methodologies for computing receptivity to KF even for cases in which transition is potentially induced

by some other forcing such as atmospheric turbulence or particulates.

The solution to the receptivity problem used in Refs. [28, 30, 39, 20] relies on assumptions about the LST spectrum topology which are not valid for a broad range of hypersonic configurations. In order to study the role of KF-receptivity in such cases, alternative methodologies are necessary. The development of such approaches is the primary focus of this dissertation. The content of the next four chapters is as follows. Chapter 2 serves as an in depth introduction to the theory underlying the work in Chapters 3-5, which represent the primary contributions of this dissertation. We begin with an introduction to fluctuating hydrodynamics which lays the theoretical framework for the incorporation of kinetic fluctuations into the hydrodynamic equations. We then proceed with a derivation of the forced, compressible, linearized boundary layer disturbance equations. Finally, we provide an overview of LST in the context of hypersonic boundary layers and link the normal mode analysis to the solution of the receptivity problem.

Chapter 3 is an exploration of the role that so called real gas effects have on receptivity to kinetic fluctuations and the stability of hypersonic boundary layers. We compare receptivity and stability results based on two different boundary layer mean flow models, a calorically perfect gas model and a 5-species model for air. We identify new features of the stability spectrum that may have important physical implications. In this chapter, KF-receptivity is computed along the lines of Ref. [39].

In Chapter 4, we develop an alternative approach to computing KF-receptivity which is applicable in cases where the method employed in Chapter 3 is insufficient or invalid. In particular, we develop a solution that does not require any assumption about the length or structure of the mode-excitation region. The approach is used to gain insight into the receptivity phenomenon, particularly for high-hypersonic cases where the dominant mode growth rate exhibits nuanced behavior near the instability onset.

Finally, in Chapter 5 we present a method for computing KF-receptivity in cases

where a branching of the discrete spectrum occurs near the region of primary excitation for the dominant mode. In such cases, it is necessary to account for two modes of the discrete spectrum in order to resolve a singularity that arises in the single-mode approximation. We show that the KF-induced disturbance in the vicinity of the discrete mode branching is governed by a forced Airy equation which may be solved analytically to obtain a regular solution to the receptivity problem.

# Chapter 2

# Governing Equations and the Linear Stability Eigenvalue Problem

This chapter provides the theoretical foundation that is common to Chapters 3-5 of this dissertation. The discussion includes three primary components. The first is a brief review of *fluctuating hydrodynamics* which lays the theoretical groundwork for the inclusion of kinetic fluctuations into the hydrodynamic equations. The next is a derivation of the forced, three-dimensional, linearized boundary layer disturbance equations from the compressible Navier-Stokes equations. Finally, we highlight the important aspects of LST in the context of hypersonic boundary layer flows.

## 2.1 Fluctuating hydrodynamics

The theory that deals with the incorporation of thermal noise into fluid flow is known as *fluctuating hydrodynamics*. The basic ideas of the theory that are relevant for the present work are summarized here for completeness. The end result will be a clear picture of how the hydrodynamic equations should be augmented to include kinetic fluctuations in the case of a one component compressible fluid.

Development of the fluctuating hydrodynamics theory [54, 53, 55, 57] was motivated by the fact that all fluids are comprised of discrete molecular components which exhibit fundamentally random behavior. In certain situations, it may be necessary to account for this underlying randomness through viewing the field variables associated with dissipative phenomena as being comprised of a mean and a random component. The random components, known as *fluctuating dissipative fluxes*, constitute an additional forcing in the hydrodynamic equations. Although small, these random fluctuations may become important in systems such as a convectively

unstable boundary layer where disturbances may be amplified exponentially. The fluctuating hydrodynamics theory was originally developed in the context of thermodynamic equilibrium. Since then, its extension to nonequilibrium flows has seen both theoretical and experimental justification, provided that an assumption of local equilibrium may be applied [78, 79, 90, 91]. In particular, fluctuating hydrodynamics has been shown to lead to results consistent with those obtained from microscopic theories based on mode-coupling [85] and kinetic theory [14] as well those based on Fokker-Plank [42, 112] and master equation [46] approaches. Fluctuating hydrodynamics has been employed broadly, including in the study of instability development in low-speed shear and channel flows [16, 97, 79, 80, 4, 23], in reactive and multi-species flows [7, 77, 47] and in the study of diffusive transport [17, 18] and convection [108, 99].

The Gibbs-Duhem equation for specific entropy $s$ is expressed as

$$T\mathrm{d}s = \mathrm{d}u + p\mathrm{d}v - \sum_k \mu_k \mathrm{d}c_k, \tag{2.1.1}$$

where $T$ is temperature, $u$ is the internal energy of the system, $v = \rho^{-1}$ is the specific volume, $\rho$ is the mass density, and $\mu_k$ and $c_k$ are the chemical potential and mass fraction of species $k$ in the fluid. Thermodynamic relations like (2.1.1) were originally developed in the context of thermodynamic equilibrium. To extend them to the context of non-equilibrium flows, we must assume that such relations hold locally for subsystems that are infinitesimally small relative to the macroscopic scale but that still contain a sufficiently large number of molecules for averaging in the sense of equilibrium statistical physics to be valid [78]. In conjunction with the continuum hypothesis, this allows the equilibrium thermodynamic quantities to be replaced by corresponding fields which vary continuously in space and time.

Assuming a one component fluid, all but the first two terms on the right side of (2.1.1) vanish. By applying the continuum hypothesis and a local equilibrium assumption to (2.1.1) and utilizing the conservation laws for mass, momentum, and

energy, we obtain the following balance law for entropy

$$\frac{\partial}{\partial t}(\rho s) + \nabla \cdot \left( (\rho s)\boldsymbol{v} + \frac{1}{T}\boldsymbol{Q} \right) = \dot{S}, \tag{2.1.2}$$

where the source term $\dot{S}$, the *entropy-generation-rate density*, is defined by

$$\Psi = T\dot{S} = -\boldsymbol{Q} \cdot \frac{\nabla T}{T} + \Pi : (\nabla \mathbf{v})^{(s)}. \tag{2.1.3}$$

Here $(\nabla \mathbf{v})^{(s)} = (1/2)\left(\partial v_i/\partial x_j + \partial v_j/\partial x_i\right)$ is the symmetric part of the velocity gradient tensor, $\boldsymbol{Q}$ is the heat flux vector, and $\Pi$ is the (symmetric) deviatoric stress tensor. The logic behind the particular grouping of components into the flux and source term in (2.1.2) is explained in detail in Ref. [15] and is one among several possible conventions [78]. The *dissipation function* $\Psi$ is the sum of a dot product and double dot product $\boldsymbol{a} : \boldsymbol{b} = a_{ij}b_{ij}$ (contraction and double contraction) of terms with the same tensorial character, and is thus a scalar quantity. Each contraction contains one of the *dissipative fluxes*, $\Pi$ and $\boldsymbol{Q}$, and the terms with which the dissipative fluxes are contracted are known as the *conjugate thermodynamic forces*.

The dissipative fluxes represent additional field variables which are unknown. For a flow in equilibrium, these fluxes vanish (as do their conjugate thermodynamic forces), and thus they cannot be incorporated into local equilibrium equations of state as can be done with an equilibrium variable such as pressure. In order to close the equations governing the evolution of the flow, the dissipative fluxes must be related to thermodynamic forces through velocity and temperature gradients and transport coefficients. To this end, note that the dissipation function $\Psi$ can be expressed in the more general form [78, 15, 52]:

$$\Psi = \sum_{\alpha} J_\alpha(\mathbf{r}, t)\, X_\alpha(\mathbf{r}, t), \tag{2.1.4}$$

where $J_\alpha$ and $X_\alpha$ represent dissipative fluxes and thermodynamic forces, respectively. In general, we expect the dissipative fluxes to be non-linear, analytic functions $J =$

$J\big(X_\alpha(\mathbf{r},t)\big)$ of the thermodynamic forces. In practice, however, for a one-component fluid we adopt the linear approximation

$$J_\alpha(\mathbf{r},t) = \sum_\beta M_{\alpha\beta}(\mathbf{r},t)\, X_\beta(\mathbf{r},t)\,, \tag{2.1.5}$$

where $M_{\alpha\beta}(\mathbf{r},t)$ are known as the Onsager coefficients. In fluctuating hydrodynamics, the phenomenological relationships (2.1.5) are assumed to hold in the average even in the presence of random fluctuations [54]. This suggests the augmented relationship

$$J_\alpha(\mathbf{r},t) = \sum_\beta M_{\alpha\beta}(\mathbf{r},t)\, X_\beta(\mathbf{r},t) + \delta J_\alpha(\mathbf{r},t)\,, \quad \overline{\delta J_\alpha(\mathbf{r},t)} = 0, \tag{2.1.6}$$

where the random components $\delta J_\alpha$ are known as *fluctuating dissipative fluxes* and the overbar represents an ensemble average. The Fluctuation-Dissipation Theorem provides expressions for the correlations between these random fluxes, which take the form [78, 15, 57]

$$\overline{\delta J_\alpha(\mathbf{r},t)\cdot\delta J_\beta(\mathbf{r}',t')} = 2k_B T M_{\alpha\beta}(\mathbf{r},t)\,\delta(\mathbf{r}-\mathbf{r}')\,\delta(t-t')\,. \tag{2.1.7}$$

The delta functions in (2.1.7) reflect the relative difference between the molecular length scales on which the fluxes are spatio-temporally correlated and the hydrodynamic scales at which we resolve the flow. The assumption about the ratio of spatial scales is expressed as $l/\Delta \ll 1$ where $l$ and $\Delta$ are representative of the mean free path and the boundary layer thickness respectively. A thorough discussion of the fundamental relationships between kinetic and hydrodynamic length scales in the development of the fluctuating hydrodynamics theory can be found in Refs. [50, 51].

In the case of a one-component compressible fluid, the coefficients $M_{\alpha\beta}(\mathbf{r},t)$ in (2.1.7) relating the dissipative fluxes and thermodynamic forces in (2.1.3) come from Fourier's law of heat transfer

$$\boldsymbol{Q}(\boldsymbol{r},t) = -\lambda\nabla T(\boldsymbol{r},t), \tag{2.1.8}$$

and Newton's law of viscosity

$$\Pi_{ij}^{(s)} = \mu\left(\frac{\partial v_i}{\partial x_j} + \frac{\partial v_j}{\partial x_i}\right) + \left(\mu_2 - \frac{2}{3}\mu\right)\delta_{ij}\frac{\partial v_k}{\partial x_k}, \tag{2.1.9}$$

where $\mu$ and $\lambda$ are viscosity and thermal conductivity, respectively, and $\mu_2$ is the bulk viscosity. In this work we are not interested in non-Newtonian fluids, however, discussion of how fluctuating hydrodynamics can be extended to fluids for which the shear viscosity is a function of the shear rate is provided in Ref. [78]. The Onsager coefficients are easily extracted from these fundamental relationships, yielding, in accordance with (2.1.7), the correlations [54, 57]:

$$\overline{\delta Q_i\left(\mathbf{r},t\right)\cdot\delta Q_j\left(\mathbf{r}',t'\right)} \;=\; 2k_B\lambda T^2\delta_{ij}\delta\left(\mathbf{r}-\mathbf{r}'\right)\delta\left(t-t'\right), \tag{2.1.10}$$

$$\overline{\delta\Pi_{i,j}\left(\mathbf{r},t\right)\cdot\delta\Pi_{kl}\left(\mathbf{r}',t'\right)} = 2k_BT\left[\mu\left(\delta_{ik}\delta_{jl}+\delta_{il}\delta_{jk}\right)+\left(\mu_2-\frac{2}{3}\mu\right)\delta_{ij}\delta_{kl}\right]\delta\left(\mathbf{r}-\mathbf{r}'\right)\delta\left(t-t'\right), \tag{2.1.11}$$

where $k_B$ is the Boltzmann constant. The cross correlations vanish in accordance with the Curie principle, which says that thermodynamic forces of different tensorial character do not couple [15]. The white noise correlation functions (2.1.10)-(2.1.11) have an important implication for the receptivity problem. In particular, they suggest that the power spectrum of kinetic fluctuations, which is constant and non-zero everywhere, will always completely contain the unstable band dictated by the flow field. This is in contrast with external disturbances such as acoustic waves which are often characterized by a narrow frequency-wavenumber dispersion relation and may need to undergo non-linear interactions before effectively exciting unstable modes [105].

Applying this theory in the context of the compressible Navier-Stokes equations for a one component fluid results in the inclusion of Langevin forcing terms corresponding to fluctuating shear stress $\delta\Pi_{ij}$ and fluctuating heat flux $\delta Q_i$. This ultimately leads to the formulation of the main object of interest in this work, the set of forced linear equations for the evolution of small disturbances excited by kinetic fluctuations in the boundary layer. An outline of how these equations are derived is provided next.

## 2.2 Governing equations

### 2.2.1 Equations of fluctuating hydrodynamics

To begin, we consider three-dimensional unsteady compressible flow with velocity $\boldsymbol{u} = (u_1, u_2, u_3)$, density $\rho$, pressure $p$, and temperature $T$ which are functions of time $t$ and coordinates $r_1, r_2$, and $r_3$. In this section superscript $\cdot^*$ indicates a dimensional quantity. The flow is governed by the Navier-Stokes equations which may be written in dimensional form using index notation as follows:

$$\frac{\partial \rho^*}{\partial t^*} + \mathrm{div}\rho^* \boldsymbol{u}^* = 0, \tag{2.2.1}$$

$$\rho^* \left[ \frac{\partial u_i^*}{\partial t^*} + (\boldsymbol{u}^* \cdot \nabla^*) u_i^* \right] = -\frac{\partial p^*}{\partial r_i^*} + \frac{\partial \Pi_{ik}^*}{\partial r_k^*}, \tag{2.2.2}$$

$$\rho^* T^* \left( \frac{\partial s^*}{\partial t^*} + (\boldsymbol{u}^* \cdot \nabla^*) s^* \right) = \frac{1}{2} \Pi_{ik}^* \left( \frac{\partial u_i^*}{\partial r_k^*} + \frac{\partial u_k^*}{\partial r_i^*} \right) - \frac{\partial Q_i^*}{\partial r_i^*}, \tag{2.2.3}$$

$$p^* = \rho^* R_g^* T^*, \tag{2.2.4}$$

where $R_g^*$ is the gas constant per unit mass and (2.2.4) is a perfect gas equation of state. The conditions under which this choice is valid are discussed in Chapter 3. Note that equation (2.2.3) can be obtained directly from the entropy balance equation (2.1.2). This is done by expanding the derivatives in (2.1.2), multiplying the equation by $T$, then using the mass conservation equation (2.2.1) and the definition of the dissipation function $\Psi = T\dot{S}$. In this process, the first term in the definition of $\Psi$ is cancelled out so that the heat flux $\boldsymbol{Q}$ only appears in (2.2.3) under the divergence. The stress tensor $\Pi_{ij}^*$ and the heat flux vector $Q_i^*$, now augmented with random fluctuating dissipative fluxes, are given by

$$\Pi_{ik}^* = \mu^* \left( \frac{\partial u_i^*}{\partial r_k^*} + \frac{\partial u_k^*}{\partial r_i^*} \right) + \left( \mu_2^* - \frac{2}{3}\mu^* \right) \delta_{ik} \mathrm{div}\, u^* + \delta\Pi_{ik}^*, \tag{2.2.5}$$

$$Q_i^* = -\lambda^* \frac{\partial T^*}{\partial r_i^*} + \delta Q_i^*, \tag{2.2.6}$$

where $s^*$ is entropy per unit mass. The fluctuating shear stress and fluctuating heat flux are represented by the mean-zero Langevin source terms $\delta\Pi_{ik}^*$ and $\delta Q_i^*$. The spatiotemporal correlations between these terms are given by (2.1.10) and (2.1.11).

Equations (2.2.1)-(2.2.4) are non-dimensionalized using boundary-layer thickness length-scale $\Delta^*$, free-stream velocity $U_\infty^*$, time-scale $\Delta^*/U_\infty^*$, doubled dynamic pressure $\rho_\infty^* U_\infty^{*2}$ and temperature $T_\infty^*$. The correlations (2.1.10) and (2.1.11) are expressed in dimensional form as

$$\overline{\delta Q_i^*(\mathbf{r}^*, t^*)\delta Q_j^*(\mathbf{r}^{*\prime}, t^{*\prime})} = \frac{\lambda^* k_B T_\infty^{*2} U_\infty^*}{\Delta^{*4}} 2T^2 \delta_{ij}\delta(\mathbf{r}-\mathbf{r}')\delta(t-t'), \tag{2.2.7}$$

$$\overline{\delta\Pi_{ik}^*(\mathbf{r}^*, t^*)\delta\Pi_{lm}^*(\mathbf{r}^{*\prime}, t^{*\prime})} = \frac{k_B T_\infty^* \mu_\infty^* U_\infty^*}{\Delta^{*4}} 2T \times \left[\mu\left(\delta_{il}\delta_{km} + \delta_{im}\delta_{kl}\right) + \left(\mu_2 - \frac{2}{3}\mu\right)\delta_{ik}\delta_{lm}\right]\delta(\mathbf{r}-\mathbf{r}')\delta(t-t'). \tag{2.2.8}$$

Introducing the natural nondimensional forms of the Langevin source terms as

$$\delta Q_i = \left[\frac{\lambda^* k_B T_\infty^{*2} U_\infty^*}{\Delta^{*4}}\right]^{-1/2} \delta Q_i^*, \quad \delta\Pi_{ik} = \left[\frac{k_B T_\infty^* \mu_\infty^* U_\infty^*}{\Delta^{*4}}\right]^{-1/2} \delta\Pi_{ik}^*, \tag{2.2.9}$$

yields the non-dimensional correlations

$$\overline{\delta Q_i(\mathbf{r}, t)\delta Q_j(\mathbf{r}', t')} = 2T^2\delta_{ij}\delta(\mathbf{r}-\mathbf{r}')\delta(t-t'), \tag{2.2.10}$$

$$\overline{\delta\Pi_{ik}(r, t)\delta\Pi_{lm}(r', t')} = 2T\mu\left[\left(\delta_{il}\delta_{km} + \delta_{im}\delta_{kl} - \frac{2}{3}\delta_{ik}\delta_{lm}\right) + \frac{\mu_2}{\mu}\delta_{ik}\delta_{lm}\right]\delta(\mathbf{r}-\mathbf{r}')\delta(t-t'). \tag{2.2.11}$$

The nondimensional governing equations are

$$\frac{\partial \rho}{\partial t} + \mathrm{div}\rho\boldsymbol{u} = 0, \tag{2.2.12}$$

$$\rho\left(\frac{\partial u_i}{\partial t}+(\boldsymbol{u}\cdot\nabla)u_i\right)= \\ -\frac{\partial p}{\partial r_i}+\frac{1}{R}\frac{\partial}{\partial r_k}\left[\mu\left[\left(\frac{\partial u_i}{\partial r_k}+\frac{\partial u_k}{\partial r_i}\right)+\left(\frac{\mu_2}{\mu}-\frac{2}{3}\right)\delta_{ik}\mathrm{div}\,\boldsymbol{u}\right]\right]+\epsilon_L\frac{\partial\delta\Pi_{ik}}{\partial r_k}, \quad (2.2.13)$$

$$\rho\left(\frac{\partial T}{\partial t}+(\boldsymbol{u}\cdot\nabla)T\right)= \\ (\gamma-1)M^2\left(\frac{\partial p}{\partial t}+(\boldsymbol{u}\cdot\nabla)p\right)+\frac{1}{R\,\mathrm{Pr}}\frac{\partial}{\partial r_i}\left(\mu\frac{\partial T}{\partial r_i}\right)+\frac{(\gamma-1)M^2}{R}\Phi+ \\ \epsilon_L(\gamma-1)M^2\frac{1}{2}\delta\Pi_{ik}\left(\frac{\partial u_i}{\partial r_k}+\frac{\partial u_k}{\partial r_i}\right)-\epsilon_L\left[\frac{(\gamma-1)\,M^2}{\mathrm{Pr}}\right]^{1/2}\frac{\partial\delta Q_i}{\partial r_i}, \quad (2.2.14)$$

$$p=\frac{1}{\gamma M^2}\rho T, \quad (2.2.15)$$

where

$$\Phi=\frac{\mu}{2}\left[\left(\frac{\partial u_i}{\partial r_k}+\frac{\partial u_k}{\partial r_i}\right)+\left(\frac{\mu_2}{\mu}-\frac{2}{3}\right)\delta_{ik}\,\mathrm{div}\,\boldsymbol{u}\right]\left(\frac{\partial u_i}{\partial r_k}+\frac{\partial u_k}{\partial r_i}\right). \quad (2.2.16)$$

Here $R=U^*_\infty\rho^*_\infty\Delta^*/\mu^*_\infty=U^*_\infty\Delta^*/\nu^*_\infty$ is the Reynolds number, $\mathrm{Pr}=\mu^*c^*_p/\lambda^*$ is the Prandtl number, $M=U^*_\infty/a^*_\infty$ is the Mach number, and

$$\epsilon_L=\frac{1}{R^2}\left(\frac{k_BT^*_\infty U^*_\infty\rho^{*2}_\infty}{\mu^{*3}_\infty}\right)^{1/2} \quad (2.2.17)$$

is a small dimensionless parameter characterizing the magnitude of kinetic fluctuations. In the above derivations, we have made use of the calorically perfect gas relations

$$\frac{p^*_\infty}{\rho^*_\infty U^{*2}_\infty}=\frac{1}{\gamma M^2},\qquad c_P=\frac{\gamma}{\gamma-1}R_g, \quad (2.2.18)$$

where $c_P$ is the specific heat at constant pressure and $\gamma$ is the specific heats ratio.

### 2.2.2 Boundary layer disturbance equations

We now derive the equations governing the linear evolution of small disturbances in the boundary layer in the presence of kinetic fluctuations. From here on out we utilize the standard notation: $(r_1, r_2, r_3) = (x, y, z)$, $(U_1, U_2, U_3) = (U_s, V_s, W_s)$, $(u_1, u_2, u_3) = (u, v, w)$, and $T = \theta$. The flow field is decomposed into a steady two-dimensional base flow and an unsteady disturbance as

$$\Psi(x, y, z, t) = \Psi_s(x, y) + \epsilon_L \psi(x, y, z, t). \tag{2.2.19}$$

The disturbance quantities appear proportional to the small parameter $\epsilon_L$, reflecting the magnitude of the random forcing. The steady base flow is a two-dimensional laminar boundary layer over a flat plate which is independent of the span-wise coordinate $z$ and only weakly varying in the streamwise coordinate $x$. This motivates the definition of a slow coordinate $x_1 = x^*/L^*$ with which the mean flow varies, where $L^*$ is a characteristic length of the plate. Because the boundary layer thickness $\Delta^* = \sqrt{\nu_\infty^* L^*/U_\infty^*}$ is small relative to the plate length, it is convenient to introduce the small parameter $\Delta^*/L^* = \epsilon \ll 1$. This latter assumption is equivalent to assuming $R = U_\infty^* \Delta^*/\nu_\infty^* = \sqrt{U_\infty^* L^*/\nu_\infty^*} = \epsilon^{-1}$ is large. From the definition of $\epsilon$, we also have the simple relation $x_1 = \epsilon x$. We take advantage of the slowly varying structure of the underlying medium by expressing the base flow in terms of the slow variable $x_1$ as

$$U_s = U(x_1, y),\ V_s = \epsilon V(x_1, y),\ P_s = P(x_1),\ T_s = T(x_1, y). \tag{2.2.20}$$

In this dissertation, the mean flow profiles are computed using one of two gas models which are described in Chapter 3. In either case, the base flow is assumed to be self-similar. Equations (2.2.12)-(2.2.16) are first linearized about the two dimensional base flow and terms $O(\epsilon_L^2)$ and higher are neglected. The validity of neglecting the nonlinear random terms may be established through comparison with the microscopic theory as is discussed in detail in Ref. [112]. The argument again essentially hinges

on the notion of local thermodynamic equilibrium, particularly in relation to the transport coefficients $\mu, \mu_2$ and $\lambda$. Dividing through by $\epsilon_L$ and accounting for the slow variation of the base flow, terms through order $O(\epsilon)$ are maintained to account for the weak non-parallel evolution of the boundary layer. This yields the following system of linear disturbance equations:

$$\frac{\partial \rho}{\partial t} + \frac{\partial}{\partial x}\left(\rho_s u + U\rho\right) + \frac{\partial}{\partial y}\left(\rho_s v + \epsilon\rho V\right) + \rho_s \frac{\partial w}{\partial z} = 0, \tag{2.2.21}$$

$$\begin{aligned}\rho_s\left(\frac{\partial u}{\partial t} + \frac{\partial}{\partial x}\left(uU\right) + v\frac{\partial U}{\partial y} + V\frac{\partial u}{\partial y}\right) = -\frac{\partial p}{\partial x} + \\ \frac{1}{R}\Bigg\{\frac{\partial}{\partial x}\left[\mu_s\left(r\frac{\partial u}{\partial x} + m\frac{\partial v}{\partial y} + m\frac{\partial w}{\partial z}\right) + \mu\left(r\frac{\partial U}{\partial x} + \epsilon m\frac{\partial V}{\partial y}\right)\right] + \\ \frac{\partial}{\partial y}\left[\mu_s\left(\frac{\partial u}{\partial y} + \frac{\partial v}{\partial x}\right) + \mu\left(\frac{\partial U}{\partial y}\right)\right] + \frac{\partial}{\partial z}\left[\mu_s\left(\frac{\partial w}{\partial x} + \frac{\partial u}{\partial z}\right)\right]\Bigg\} + \\ \left(\frac{\partial \delta\Pi_{xx}}{\partial x} + \frac{\partial \delta\Pi_{xy}}{\partial y} + \frac{\partial \delta\Pi_{xz}}{\partial z}\right),\end{aligned} \tag{2.2.22}$$

$$\begin{aligned}\rho_s\left(\frac{\partial v}{\partial t} + U\frac{\partial v}{\partial x} + \epsilon\frac{\partial}{\partial y}\left(vV\right)\right) = -\frac{\partial p}{\partial y} + \frac{1}{R}\Bigg\{\frac{\partial}{\partial x}\left[\mu_s\left(\frac{\partial u}{\partial y} + \frac{\partial v}{\partial x}\right)\right] + \frac{\partial \mu}{\partial x}\frac{\partial U}{\partial y} + \\ \frac{\partial}{\partial y}\left[\mu_s\left(m\frac{\partial u}{\partial x} + r\frac{\partial v}{\partial y} + m\frac{\partial w}{\partial z}\right) + \mu\left(m\frac{\partial U}{\partial x} + \epsilon r\frac{\partial V}{\partial y}\right)\right] + \\ \frac{\partial}{\partial z}\left[\mu_s\left(\frac{\partial v}{\partial z} + \frac{\partial w}{\partial y}\right)\right]\Bigg\} + \left(\frac{\partial \delta\Pi_{yx}}{\partial x} + \frac{\partial \delta\Pi_{yy}}{\partial y} + \frac{\partial \delta\Pi_{yz}}{\partial z}\right),\end{aligned} \tag{2.2.23}$$

$$\begin{aligned}\rho_s\left(\frac{\partial w}{\partial t} + U\frac{\partial w}{\partial x} + \epsilon V\frac{\partial w}{\partial y}\right) = -\frac{\partial p}{\partial z} + \frac{1}{R}\Bigg\{\frac{\partial}{\partial x}\left[\mu_s\left(\frac{\partial w}{\partial x} + \frac{\partial u}{\partial z}\right)\right] + \\ \frac{\partial}{\partial y}\left[\mu_s\left(\frac{\partial v}{\partial z} + \frac{\partial w}{\partial y}\right)\right] + \frac{\partial}{\partial z}\left[\mu_s\left(m\frac{\partial u}{\partial x} + m\frac{\partial v}{\partial y} + r\frac{\partial w}{\partial z}\right)\right]\Bigg\} + \\ \left(\frac{\partial \delta\Pi_{zx}}{\partial x} + \frac{\partial \delta\Pi_{zy}}{\partial y} + \frac{\partial \delta\Pi_{zz}}{\partial z}\right),\end{aligned} \tag{2.2.24}$$

$$\rho_s\left(\frac{\partial\theta}{\partial t}+u\frac{\partial T_s}{\partial x}+U\frac{\partial\theta}{\partial x}+v\frac{\partial T_s}{\partial y}+\epsilon V\frac{\partial\theta}{\partial y}+w\frac{\partial T_s}{\partial z}\right)+\rho\left(U\frac{\partial T_s}{\partial x}+\epsilon V\frac{\partial T_s}{\partial y}\right)$$
$$=(\gamma-1)M^2\left[\frac{\partial p}{\partial t}+u\frac{\partial P}{\partial x}+U\frac{\partial p}{\partial x}+V\frac{\partial p}{\partial y}+\frac{1}{R}\Phi'\right]+$$
$$\frac{1}{R\,\mathrm{Pr}}\left[\frac{\partial}{\partial x}\left(\mu_s\frac{\partial\theta}{\partial x}\right)+\frac{\partial\mu}{\partial x}\frac{\partial T_s}{\partial x}+\frac{\partial}{\partial y}\left(\mu_s\frac{\partial\theta}{\partial y}+\mu\frac{\partial T_s}{\partial y}\right)+\frac{\partial}{\partial z}\left(\mu_s\frac{\partial\theta}{\partial z}\right)\right]-$$
$$\left(\frac{(\gamma-1)\,M^2}{\mathrm{Pr}}\right)^{1/2}\left(\frac{\partial\delta Q_x}{\partial x}+\frac{\partial\delta Q_y}{\partial y}+\frac{\partial\delta Q_z}{\partial z}\right)+$$
$$\frac{(\gamma-1)M^2}{2}\left[\left(\delta\Pi_{xy}+\delta\Pi_{yx}\right)\frac{\partial U}{\partial y}\right], \quad (2.2.25)$$

$$\frac{p}{P}=\frac{\theta}{T_s}+\frac{\rho}{\rho_s}, \quad (2.2.26)$$

where $\Phi'$ is the linearized dissipation function. One can find its explicit form, for example, in Ref. [75]. Note that stream-wise derivatives of mean flow quantities in the above equations are of order $\epsilon$ since $\partial/\partial x=\epsilon\partial/\partial x_1$. The coefficients $r$ and $m$ in Eqs. (2.2.22) - (2.2.24) depend on the bulk viscosity ratio $\mu_2/\mu=2e/3$ as $m=2(e-1)/3$, $r=2(e+2)/3$. Throughout this dissertation, we take $e=0$ in accordance with the Stokes hypothesis. The disturbance viscosity in equations (2.2.21) - (2.2.26) is related to the temperature disturbance as $\mu=(d\mu_s/dT)\theta$. Equations (2.2.21) - (2.2.26), with $O(\epsilon)$ terms included, are the conventional linearized, 3D, nonparallel, compressible boundary layer disturbance equations with the addition of forcing due to kinetic fluctuations.

## 2.3 Eigenmode expansion and the linear stability eigenvalue problem

In this section, we introduce the main ideas of the application of LST to hypersonic boundary layers. As a means for demonstration, we consider a representative flat plate hypersonic boundary layer in a calorically perfect gas. The choice of flow parameters, which are provided in Table 2.1, is discussed in Chapter 5. For the remainder of this chapter, all results correspond to this Mach 6 test case.

| M | $T_e^*$ (K) | $T_w^*/T_{ad}^*$ | $U_e^*$ (m/s) | $\nu_e^*$ (m/s$^2$) | Pr | $\gamma$ |
|---|---|---|---|---|---|---|
| 6.0 | 283.0 | 0.99 | 2020.0 | $1.09 \times 10^{-4}$ | 0.72 | 1.40 |

TABLE 2.1. Details of the flow parameters for the Mach 6 test case.

### 2.3.1 Boundary layer mean flow

Two different mean boundary layer profile solvers are used in this dissertation, a calorically perfect gas model (CP) and a real gas model (Air) based on a five-species model for air. Because there is no fundamental length scale in the streamwise direction for a boundary layer over a semi-infinite flat plate, it is possible to approximate the full fluid dynamic equations and obtain self similar solutions describing the base flow under both models. The CP model is the one used primarily in this work. Under this model, the mean velocity and temperature profiles may be found via numerical solution of the compressible Blasius boundary layer equations, a system of coupled non-linear ODEs. This procedure is standard and details can be found in many references, such as Ref. [89]. The second solver assumes a boundary layer of real gas based on a five-species model for air. This model is discussed further in Chapter 3 and in full detail in Ref. [20]. The error in the self-similar approximation of the mean flow versus a direct numerical simulation of the Navier-Stokes equations has been shown to be negligible across a broad range of configurations [61, 100]. The discrepancy in the stability results has also been shown to be insignificant for a hypersonic flat plate boundary layer [101].

Figures 2.1a and 2.1b show the CP self-similar mean profiles $U$ and $T$ as functions of $y = y^*/\Delta^*$, where the boundary layer length scale $\Delta^*$ is now defined explicitly as $\Delta^* = \sqrt{2\nu_\infty^* x^*/U_\infty^*}$. The mean viscosity, shown in Figure 2.1c, is computed using Sutherland's law

$$\mu(T) = \frac{(1+S)T^{3/2}}{T+S}, \quad S = \frac{110.4}{T_\infty^*}. \tag{2.3.1}$$

One notion of boundary layer width, denoted $\delta_{99}$, is defined based on the location

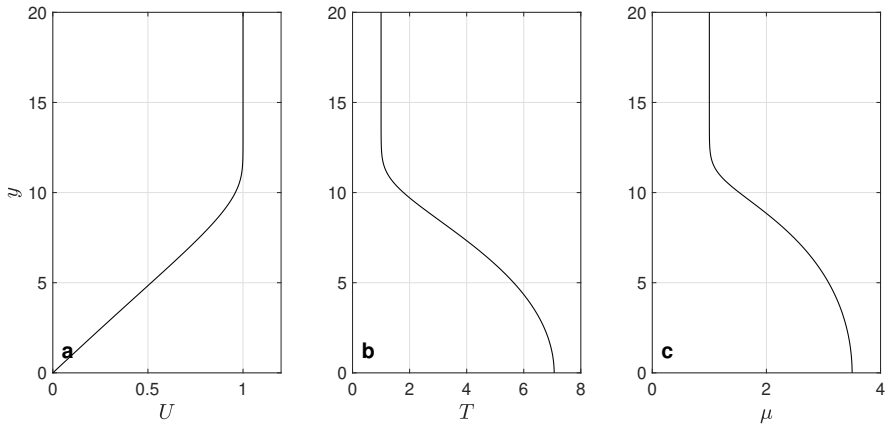


FIGURE 2.1. Mean flow profiles (a) $U$, (b) $T$ and (c) $\mu$ for the $M = 6$ test case.

where $U^*/U^*_\infty = 0.99$. Based on this definition, the edge of the boundary layer in this case is $y = 10.9$.

### 2.3.2 Expansion of disturbance field into eigenmodes

In the conventional boundary layer linear stability theory (LST), a solution to the homogeneous version of the linearized disturbance equations (2.2.22) - (2.2.26), with non-parallel effects neglected (quasi-parallel approximation), is sought as an expansion into normal modes of the form

$$\psi'(x, y, z, t) = \psi(y) \exp(i\alpha x + i\beta z - i\omega t). \tag{2.3.2}$$

Depending on the physical setup, it may be of interest to view disturbances as either evolving in time or in space. In the former case, the wavenumber is prescribed as a parameter and the complex frequency $\omega$ must be determined. In the latter framework, which is the one adopted in this dissertation, the complex streamwise wavenumber $\alpha$ is found given the real parameters $\omega$ and $\beta$.

Tumin [100] solved the spatial Cauchy problem for disturbances evolving in a two-dimensional compressible boundary layer. In his approach, the equations are recast

as a $16 \times 16$ first order linear system written in terms of the disturbance vector

$$\boldsymbol{A} = \left( u, \frac{\partial u}{\partial y}, v, p, \theta, \frac{\partial \theta}{\partial y}, w, \frac{\partial w}{\partial y}, \frac{\partial u}{\partial x}, \frac{\partial v}{\partial x}, \frac{\partial \theta}{\partial x}, \frac{\partial w}{\partial x}, \frac{\partial u}{\partial z}, \frac{\partial v}{\partial z}, \frac{\partial \theta}{\partial z}, \frac{\partial w}{\partial z} \right). \tag{2.3.3}$$

The equations are Fourier transformed in time $t$ and the spanwise direction $z$ and a Laplace transform is taken in $x$. The resulting system of first order linear ODEs is solved formally and the solution $\boldsymbol{A}_{p\beta\omega}$ is expressed as a sum of the fundamental solutions. The Laplace transform is inverted via integration over a contour in the complex $p$-plane. The input to this integral consists of a sum over $n$ residues and $2m$ integrals along either side $\gamma_m^+$ and $\gamma_m^-$ of $m$ branch cuts:

$$\boldsymbol{A}_{\omega\beta} = \sum_n \mathrm{Res}\left(\boldsymbol{A}_{p\omega\beta} e^{px}\right) - \frac{1}{2\pi i} \sum_m \left( \int_{\gamma_m^+} \boldsymbol{A}_{p\omega\beta} e^{px} \mathrm{d}p + \int_{\gamma_m^-} \boldsymbol{A}_{p\omega\beta} e^{px} \mathrm{d}p \right). \tag{2.3.4}$$

The $2m$ branch cut integrals in (2.3.4) may be expressed as $m$ single integrals in parameter $k$. Then, writing $p = i\alpha$, expression (2.3.4) may be expressed in the form

$$\boldsymbol{A}_{\omega\beta} = \sum_n \boldsymbol{A}_{\alpha_n}(y) e^{i\alpha_n x} + \sum_m \int_0^\infty \boldsymbol{A}_{\alpha_m}(y,k) e^{i\alpha_m(k)x} \mathrm{d}k \tag{2.3.5}$$

This expression is usefully viewed as an expansion of the solution into the discrete and continuous spectrum of the linear stability operator. The typical spectrum topology for a hypersonic boundary layer is discussed in §2.3.5. Although the formalism adopted in this dissertation is different from that just described, the idea of expressing the boundary layer disturbances in terms of eigenmodes will play a fundamental role.

### 2.3.3 LST eigenvalue problem

In what follows, we describe the derivation of the conventional eigenvalue problem of linear stability theory. In this dissertation, the KF-induced disturbance is expressed

using LST modes, although, the solution is not strictly speaking an expansion into the eigenfunction system. Rather, the eigenmodes represent a leading order approximation to the solution. Because the LST framework is essentially the same across Chapters 3-5, it is convenient to introduce the main ideas here and refer back to them when necessary. In this section, we consider the unforced problem governed by the homogeneous form of equations (2.2.21) - (2.2.26).

We begin by introducing the 8-component disturbance vector

$$\boldsymbol{F}(x,y,z,t) = \left(u, \frac{\partial u}{\partial y}, v, p, \theta, \frac{\partial \theta}{\partial y}, w, \frac{\partial w}{\partial y}\right), \tag{2.3.6}$$

Derivatives in the wall-normal coordinate $y$ appear in $\boldsymbol{F}$ so that (2.2.21) - (2.2.26) may be expressed as system of differential equations that are first order in $y$. Let $\hat{\boldsymbol{F}}$ be the Fourier transform of $\boldsymbol{F}$ with respect to time $t$ and the span-wise coordinate $z$, where our convention is given by

$$\hat{\boldsymbol{F}}(\omega,\beta) = \int_{-\infty}^{\infty} \boldsymbol{F}(t,z) e^{i(\omega z - \beta t)} \mathrm{d}t\mathrm{d}z, \tag{2.3.7}$$

$$\boldsymbol{F}(t,z) = \frac{1}{(2\pi)^2} \int_{-\infty}^{\infty} \hat{\boldsymbol{F}}(\omega,\beta) e^{-i(\omega z - \beta t)} \mathrm{d}\omega\mathrm{d}\beta. \tag{2.3.8}$$

The transformed homogeneous boundary layer disturbance equations can be expressed in terms of the slow coordinate $x_1$ as a first order linear PDE system with the $8 \times 8$ matrix operator $\mathrm{H}^{(np)}$ as

$$\begin{gathered} \mathrm{H}^{(np)}(y, \partial_y, x_1, \epsilon\partial_{x_1}, \omega, \beta)\hat{\boldsymbol{F}} = 0, \\ y = 0 : \hat{F}_i = 0, \ \ i = 1,3,5,7, \\ y \to \infty : |\hat{F}_i| < \infty, \ \ i = 1,3,5,7. \end{gathered} \tag{2.3.9}$$

Superscript 'np' indicates that we have maintained nonparallel terms in the linearized governing equations. The second, fourth and eighth equations in (2.3.9) represent the stream-wise, wall-normal and span-wise momentum equations respectively. The third equation is the continuity equation, and the remaining three arise from the reduction of the system to first order in $y$. The boundary conditions at $y = 0$ correspond to

a no-slip condition for the three velocity components and a vanishing temperature disturbance on the wall. The far field conditions ensure that the disturbances are bounded outside of the boundary layer. For modes of the discrete spectrum, this condition may be strengthened to require that the disturbances vanish in the far field. In this dissertation, a solution to (2.3.9) is expressed only in terms of the discrete spectrum.

An approximate solution to (2.3.9) is introduced in terms of the multiple scales Wentzel–Kramers–Brillouin (WKB) [5] type ansatz

$$\hat{\boldsymbol{F}} = \left[\boldsymbol{F}^{(0)}(x_1, y) + \epsilon \boldsymbol{F}^{(1)}(x_1, y) + \cdots\right] K(x_1), \tag{2.3.10}$$

$$K(x_1) = \exp\left[i\epsilon^{-1} \int^{x_1} \alpha(\eta; \omega, \beta) \mathrm{d}\eta\right]. \tag{2.3.11}$$

This approach is motivated by the disparity between the stream-wise scales at which the boundary layer mean profiles vary, and the comparatively small scales at which the disturbance quantities vary. Conditions for the validity of the WKB expansion are well understood (see, for example, Ref. [5]) and a case for which the approximation fails is discussed in detail in Chapter 5 of this dissertation. The leading order behavior in (2.3.11) corresponds to the quasi-parallel flow approximation. The effect of the weak downstream growth of the boundary layer, or non-parallel effects, may be captured through incorporating the higher order correction terms. In the context of LST, the WKB approximation was first introduced by Bouthier [9], Gaster [41], Nayfeh et al. [76] to study the influence of non-parallel effects on the stability of low speed boundary layers. Saric and Nayfeh [86, 87] showed that by accounting for non-parallel flow effects, one could attain better theoretical agreement with experimental neutral curve data, particularly in the presence of an adverse pressure gradient. Later on, the method was used to study the stability of weakly non-parallel compressible boundary-layer flows [81, 40, 75, 22, 102]. The method of multiple scales has also proven useful in the study of distributed receptivity. Examples include an acoustic wave interacting with a boundary layer on a smooth wall [24, 25] or a wall with distributed roughness

elements [111, 11]. One can find the mathematical details and relevant bibliography in Refs. [12, 101, 27, 113]. Kinetic fluctuations are an example of distributed forcing in a boundary-layer flow.

Inserting (2.3.11) into (2.3.9) yields a series of linear equations, one at each order in $\epsilon$:

$$O(1):\ \mathcal{L}_0 \boldsymbol{F}^{(0)} = 0 \tag{2.3.12}$$

$$O(\epsilon):\ \mathcal{L}_0 \boldsymbol{F}^{(1)} = -\left( i\frac{\partial \mathrm{H}_0}{\partial \alpha}\frac{\partial}{\partial x_1} - \mathrm{H}_1 \right) \boldsymbol{F}^{(0)} \tag{2.3.13}$$

$$\vdots$$

The linear differential operator $\mathcal{L}_0$ that appears in the problem at each order is defined by

$$\mathcal{L}_0 = \left( \frac{\partial}{\partial y} - \mathrm{H}_0 \right), \tag{2.3.14}$$

where $\mathrm{H}_0$ is an $8 \times 8$ linear operator depending on $\alpha, \beta$ and $\omega$ as well as the Reynolds number and the steady base flow $\Psi_s = \Psi_s(y; x_1)$. Its non-zero entries are provided in Appendix A.2. The problem at leading order, along with appropriate boundary conditions, is the conventional LST eigenvalue problem

$$\begin{gathered} \mathcal{L}_0 \boldsymbol{F}^{(0)} = 0, \\ y = 0 : F_i^{(0)} = 0,\ i = 1, 3, 5, 7, \\ y \to \infty : \left| F_i^{(0)} \right| < \infty,\ i = 1, 3, 5, 7. \end{gathered} \tag{2.3.15}$$

Defining an inner product $\langle \cdot, \cdot \rangle$ by:

$$\langle \boldsymbol{f}, \boldsymbol{h} \rangle = \int_0^\infty \sum_{i=1}^{8} f_i h_i^* \mathrm{d}y, \tag{2.3.16}$$

the adjoint problem corresponding to (2.3.15) may be expressed as

$$\begin{gathered} \mathcal{L}_0^\dagger \boldsymbol{B}^{(0)} = 0, \quad \mathcal{L}_0^\dagger = \left( \frac{\partial}{\partial y} + \mathrm{H}_0^H \right), \\ y = 0 : B_i^{(0)} = 0,\ i = 2, 4, 6, 8, \\ y \to \infty : \left| B_i^{(0)} \right| < \infty,\ i = 2, 4, 6, 8. \end{gathered} \tag{2.3.17}$$

Where superscript '$H$' indicates the conjugate transpose or Hermitian. Ref. [62] provides a good review of the use of adjoint problems in hydrodynamic stability and receptivity. It can be shown that the direct and adjoint eigenfunctions satisfy the biorthogonality condition [100]

$$\left\langle -i\frac{\partial \mathrm{H}_0}{\partial \alpha}\boldsymbol{F}^{(0)}_{\alpha_j}, \boldsymbol{B}^{(0)}_{\alpha_k} \right\rangle = \Gamma \Delta_{jk}, \tag{2.3.18}$$

where $\Delta_{jk}$ is the Dirac delta if both $\alpha_j$ and $\alpha_k$ belong to the continuous spectrum, and the Kronecker delta if either or both correspond to discrete modes. The factor $\Gamma$ depends on the normalization of the eigenfunctions.

Traditional LST typically starts and ends with the leading order problem (2.3.15). A higher order correction can be obtained by considering the problem at $O(\epsilon)$. In particular, eqn. (2.3.13), along with the appropriate homogeneous boundary conditions, may be used to account for the effect of the weakly nonparallel nature of the boundary layer on the discrete mode wavenumber. Since the eigenfunction is determined only up to an arbitrary normalization, we express $\boldsymbol{F}^{(0)}$ in terms of the product $\boldsymbol{F}^{(0)} = c(x_1)\boldsymbol{A}^{(0)}(x_1, y)$, where $c$ is an amplitude function to be determined. Inserting this expression into the $O(\epsilon)$ problem (2.3.13) and imposing the solvability condition yields an ODE for the amplitude function $c$. By solving this equation we can obtain the solution up to the so called 'physical-optics' level WKB approximation. It is common to neglect the $O(\epsilon)$ amplitude correction term $\boldsymbol{F}^{(1)}$ and higher order corrections as the leading order term in the geometric or physical-optics level approximation is usually sufficient for most applications [113, 5].

In this work, we are primarily interested in the inhomogeneous version of problem (2.3.9), where forcing associated with kinetic fluctuations has been introduced. In this case, the problem at $O(\epsilon)$, in addition to describing nonparallel effects, also allows for the determination of the physical amplitude $c$ induced by the forcing. In other words, the problem at $O(\epsilon)$ allows for the solution of the receptivity problem which is completely undetermined by the LST eigenvalue problem. This is a central idea of

this dissertation and will be explored in detail in Chapters 3-5.

### 2.3.4 Numerical solution of the LST eigenvalue problem

In this section, we describe the procedure for the numerical solution of eigenvalue problem (2.3.15) for modes of the discrete spectrum. For fixed $\beta, \omega$, fixed Reynolds number $R$, and known mean flow profiles, the homogeneous boundary value problem (2.3.15) may be solved numerically as an eigenvalue problem for complex $\alpha$ and the amplitude-shape function $\boldsymbol{F}^{(0)}$. An outline of the numerical procedure is as follows:

1. Outside of the boundary layer ($y \to \infty$) $\mathrm{H}_0^\infty = \mathrm{H}_0(y = \infty)$ is a matrix of constant coefficients. We can thus analytically determine 8 fundamental solutions of the resulting linear system in terms of the eigenvalues and eigenvectors of $\mathrm{H}_0^\infty$. These solutions determine the far field asymptotic behavior of the fundamental solutions to (2.3.15).

2. Given an initial guess for the eigenvalue $\alpha$, the equations are integrated from the known asymptotic solutions outside the boundary layer down to the wall ($y = 0$).

3. The vector of eigenfunctions is formed through a linear superposition of the four fundamental solutions exhibiting far-field exponential decay. This is done through satisfying the no slip condition $(A_1, A_3, A_7)\big|_{y=0} = (0, 0, 0)$, and imposing a normalization via the condition $A_2\big|_{y=0} = 1$, which corresponds to $\partial u/\partial y = 1$.

4. Finally, the complex eigenvalue $\alpha$ is found through enforcing the fourth wall boundary condition $\theta\big|_{y=0} = 0$. This is accomplished by iterating on $\alpha$ using a 2D Newton-Raphson scheme and repeating the integration until the condition has been satisfied to within a given tolerance.

In the derivation of the stability equations, the Reynolds number was defined as $R = U^*_\infty \Delta^*/\nu^*_\infty$. If we specify the definition of the boundary layer scale as $\Delta^* = \sqrt{2\nu^*_\infty x^*/U^*_\infty}$ then $R$ may be viewed as a dimensionless streamwise coordinate, as will be usefully done throughout this dissertation. Since the mean flow profiles are also a function of $\Delta^*$ through the dimensionless coordinate $y = y^*/\Delta^*$, this definition of $R$ facilitates the use of the self-similar base flow which may be computed once and for all. The evolution of the LST spectrum in the streamwise direction, described next, can be understood through solving the eigenvalue problem (2.3.15) for increasing values of $R$.

### 2.3.5 Spectrum of the LST operator

The LST eigenvalue problem (2.3.15) admits both a discrete and a continuous spectrum. Figure 2.2 shows the typical spectrum topology for fixed $R, \beta$ and $\omega$ for a hypersonic boundary layer. The vertical branch of the continuous spectrum is associated with vorticity/entropy perturbations based on the features of the corresponding eigenfunctions outside the boundary layer. The horizontal branches are associated with so-called 'fast' and 'slow' acoustic waves. The labels fast and slow indicate waves traveling downstream or upstream, respectively, relative to the free-stream. In terms of dimensionless phase speed $c_r = \Re[\omega/\alpha]$, the sonic lines are given by

$$c = \frac{c^*}{U^*_\infty} = \frac{U^*_\infty \pm a^*_\infty}{U^*_\infty} = 1 \pm \frac{1}{M}. \tag{2.3.19}$$

If for some mode the phase speed $c_r = 1 + 1/M$, the associated wave is traveling upstream sonically relative to the free-stream velocity $U^*_\infty$, and if $c_r = 1 - 1/M$, the wave is traveling sonically downstream.

As is indicated in Figure 2.2, there are a number of discrete modes present depending on the parameters $R, \omega, \beta$ and the boundary layer configuration. Importantly, typically only a single mode of the discrete spectrum is significantly unstable for pa-

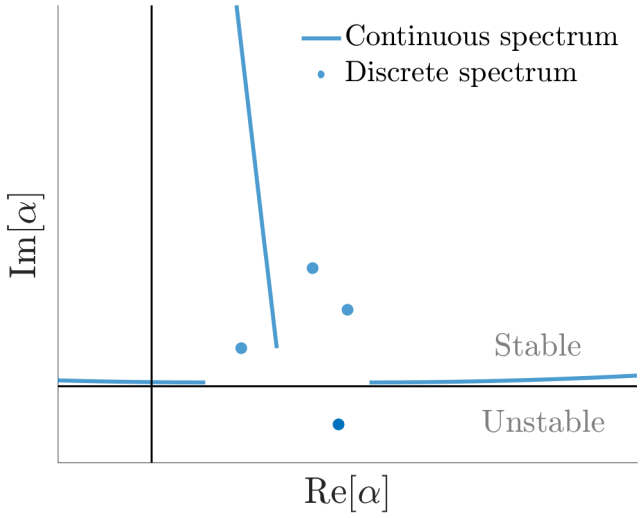


FIGURE 2.2. Spectrum topology of the LST eigenvalue problem.

rameters of physical interest. In this work, we are primarily interested in two modes of the discrete spectrum, which are referred to as 'Mode S' and 'Mode F' [38]. These labels are based on a connection with slow and fast waves of the continuous spectrum as is explained momentarily. Either of them may represent the dominant instability, depending on the boundary layer configuration.

The basic downstream evolution of Modes S and F for the $M = 6$ test case is shown as a function of $R$ in Figure 2.3. The details of the configuration are given in Table 2.1 and discussed in Chapter 5 under the label 'Case B'. There are three components of the discrete mode trajectory to highlight, indicated in Figure 2.3a by the labels '1', '2' and '3'.

1. *Synchronization with acoustic waves of the continuous spectrum.* Near the leading edge of the plate, the phase speeds $c_r = \Re[\omega/\alpha]$ of Mode F and Mode S approach the sonic lines $c_r = 1 \pm M^{-1}$ where they are synchronized with fast and slow acoustic waves of the continuous spectrum. This is the motivation for the terminology Mode S and Mode F [26].

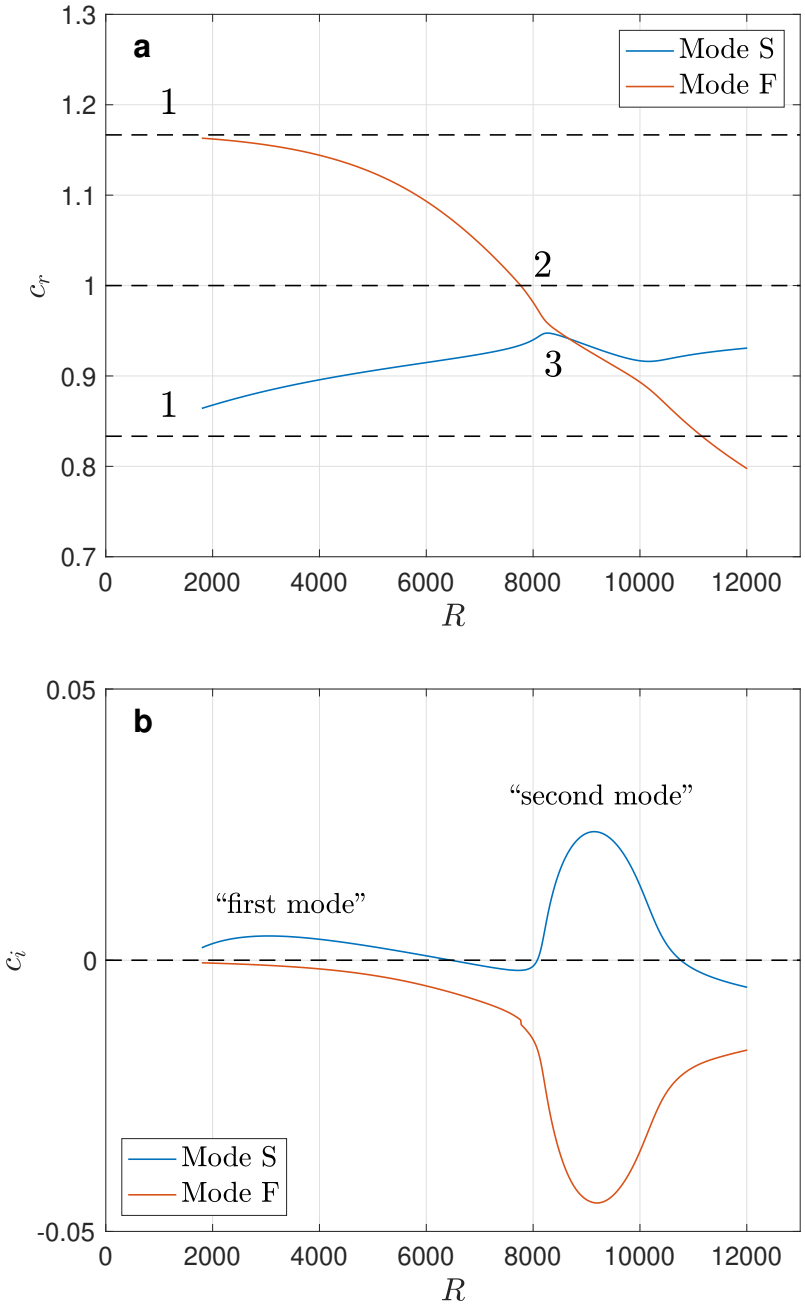


FIGURE 2.3. Evolution of Modes S and F for a representative Mach 6 configuration.

2. *Synchronization of Mode F with vorticity waves.* In region 2, there is a phase speed synchronization between Mode F and the continuous spectrum branch associated with vorticity waves. Connections have been made between this synchronization phenomenon and receptivity of the boundary layer to free-stream vorticity and entropy perturbations from, for example, free-stream turbulence [34]. Mathematically, the eigenvalues upstream and downstream of the synchronization correspond to two different modes and a distinction is sometimes made using the labels Mode $F^-$ and Mode $F^+$, respectively. Because the real part of the eigenvalue $\alpha_r$ is continuous across the branch cut and $\alpha_i$ exhibits only a small finite jump, the two modes are commonly (and erroneously) referred to as a single mode. In this dissertation, this issue will not play an important role and the term Mode F can be understood to refer to Mode $F^+$.

3. *Synchronization of Modes S and F.* In region 3, the phase speeds of Modes S and F are nearly synchronized, leading to a branching of the discrete spectrum [45]. From a mathematical perspective it is useful to view the exact synchronization of discrete modes as corresponding to a branch point Reynolds number $R_{\mathrm{br}}$, which is in general complex. Downstream of the synchronization region, either Mode S or Mode F becomes highly unstable while the other is further stabilized. For the parameters chosen to produce Figure 2.3, Mode S is associated with unstable waves while Mode F is stable. The branching topology depends on whether the complex branch point is bypassed from above or below along the real axis. This topology, and thus which mode is unstable, can change spontaneously with an increase in, for example, Mach number or Reynolds number [34].

The synchronization of discrete modes can pose challenges for the application of traditional LST in solving the receptivity problem. The associated challenges will appear in each of the three major chapters of this dissertation in a variety of contexts. The synchronization of Mode S and F near the onset of instability is especially relevant

to the solution of the receptivity problem and overcoming the associated difficulties is the central focus of Chapter 5.

At this stage, it is useful to point out a discrepancy in the terminology commonly used in discussions of boundary layer linear stability theory. Originally, the term 'mode' in this context was used to identify individual features of the stability curve associated with a single component of the discrete spectrum. For example, in Figure 2.3a, Mode S is seen to have two regions of instability. The first region is often referred to as the 'first mode' and the more dominant feature occurring further downstream is known as the 'second mode'. This terminology, originally put forward by Mack [67] in the late 1960's, is inconsistent with the mathematical definition of a mode as an eigenfunction into which we may expand the solution of a PDE. In this work, the names Mode S and Mode F will be used in the mathematical sense to refer to the two distinct components of the discrete spectrum whose evolution is depicted in Figure 2.3. For convenience and consistency with the literature on this topic, the terminology 'first Mack mode' and 'second Mack mode' will sometimes be used. They will refer to the instability features identified in Figure 2.3b of the unstable wave, which in general may correspond to either Mode F or Mode S.

Finally, Figure 2.4 shows the absolute value of the eigenfunctions of the dominant unstable mode for disturbances $u$, $p$, and $\theta$ for the $M = 6$ test case. Each of the eigenfunctions has been normalized to have maximum equal to one. The figure corresponds to parameters $F = \omega^* \nu_\infty^* / U_\infty^{*2} = 5.0 \times 10^{-5}$, $\beta = 0$, and $R = 4914$. The streamwise velocity and temperature disturbances satisfy the homogeneous wall boundary condition and all three decay exponentially outside the boundary layer. The location of the boundary layer edge is indicated by $\delta_{99}$. The prominent peak in the temperature disturbance eigenfunction occurs in the so called critical layer, $y = y_c$. The wall-normal location $y_c$ marks the point where the phase speed $c_r$ of the mode matches the streamwise velocity of the boundary layer, i.e. $U(y_c) = c_r$. The critical layer tends to be the locus of boundary layer receptivity mechanisms, as will

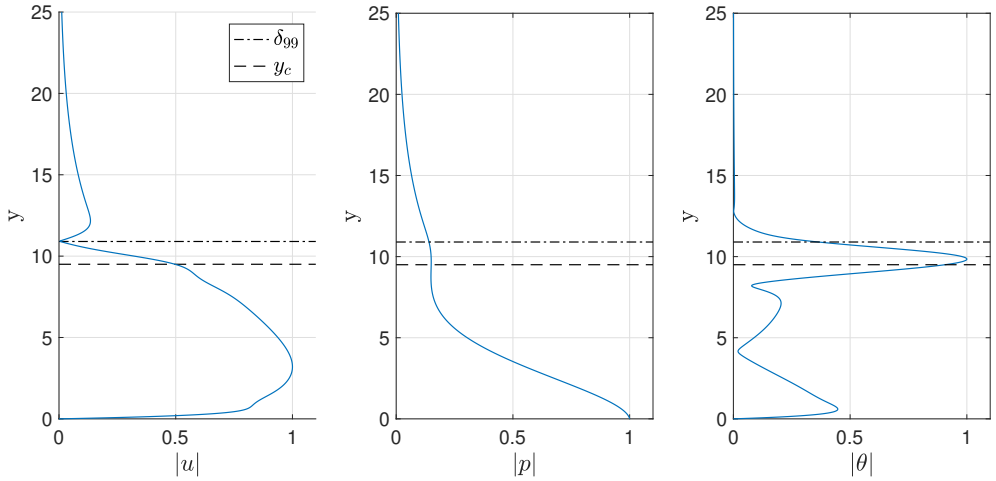


FIGURE 2.4. Eigenfunctions for mean flow disturbance quantities for the $M = 6$ test case, $F = 5.0 \times 10^{-5}$, $\beta = 0$, and $R = 4914$.

be discussed in detail later on. Importantly, for the high Mach number configurations considered in this work, the critical layer is close to the boundary layer edge.

## 2.4 The $N$-factor and the $e^N$ method

Results of LST are typically summarized in terms of the so called $N$-factor, defined simply as the integral of the unstable discrete mode growth rate

$$N(x) = \int_{x_0}^{x} \sigma(x'; \omega, \beta) \mathrm{d}x', \qquad \sigma = -\Im[\alpha]. \tag{2.4.1}$$

The lower bound of the integral, $x_0$, is typically taken to be the lower neutral point, the point where the mode first becomes unstable. The quantity $e^N$ is then understood to account for the cumulative amplification potential of the disturbance associated with the unstable wave of fixed frequency $\omega$ and span-wise wavenumber $\beta$. At each each observation point in the streamwise direction, an infinite number of waves associated with the unstable mode are amplified. On the other hand, at each location (or equivalently, for fixed $R$), there is a single wave which is maximally

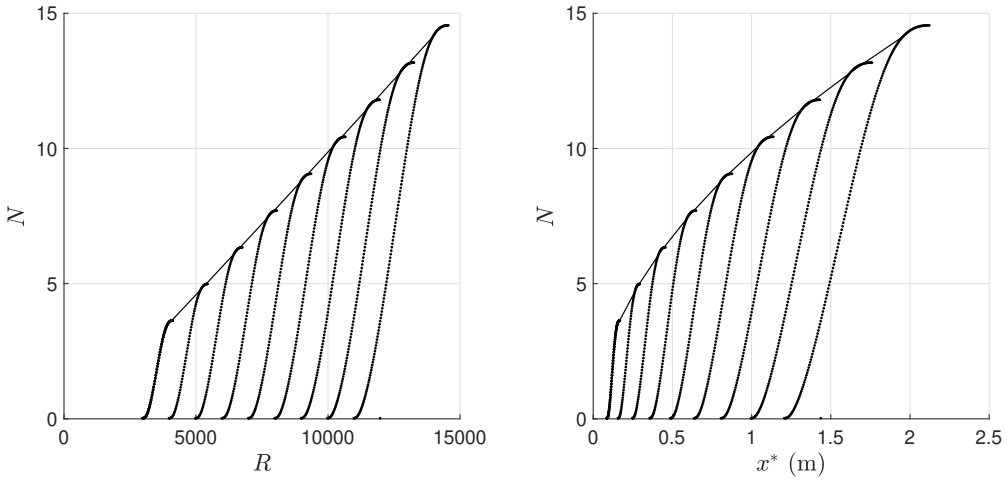


FIGURE 2.5. $N$-factor curves for the Mach 6 test case.

amplified with corresponding $N$-factor $N_{\max}$. The curve $N_{\max}(x)$ (or $N_{\max}(R)$) defines the $N$-factor envelope. The $N$-factor curves for a series of frequency parameters $F$ and $\beta = 0$ as well as the envelope are plotted in Figures 2.5a and 2.5b as functions of $R$ and $x^*$ respectively. For hypersonic boundary layers, the most amplified waves are two-dimensional, i.e. $\beta = 0$, for all frequencies. For supersonic configurations the most amplified waves are oblique.

Since the late 1960's and continuing through to this day, attempts have been made to correlate $N$-factors computed through LST to the location of laminar-turbulent transition onset observed in experiments [67]. In this context, the quantity $e^N$ is thought of as the ratio of the amplitude $A$ at some observation point to the amplitude $A_0$ at some initial station

$$\exp(N) = A/A_0. \tag{2.4.2}$$

This is the so-called $e^N$ method. As an example, $N$-factors in the range $9 - 16$ are typically associated with transition in actual high-speed flight conditions. Lower transition $N$-factors are quoted in connection to wind-tunnel experiments, a fact that is attributed to higher levels of free-stream noise from, for example, turbulent

boundary layers on the walls of the tunnel [27].

Of the many shortcomings of the so called $e^N$ method, the most obvious is that the quantity $N$ accounts only for the potential for amplification; It says nothing about the initial amplitude of the mode, if, in fact, the mode has been excited at all. As discussed earlier, determining the physical amplitudes of components of the linear stability spectrum is the role of receptivity theory. In that way, LST, which is somewhat detached from the physical problem at hand, does not become truly powerful until it is appropriately coupled with receptivity calculations. Nevertheless, knowledge of $N$-factors which are 'typical' for transition for a certain physical setup can be useful for intuition when performing calculations.

Finally, we emphasize that the $N$-factor envelope accounts only for the wave which is most amplified at a given streamwise location. In reality, there is a band of frequencies and spanwise wavenumbers that are amplified at each station. This is visualized in Figure 2.6 which shows the spectral amplification $N = N(\omega, \beta)$ at a fixed observation point. The normalization of $\omega$ and $\beta$ is based on the observation point corresponding to Reynolds number $R = 4000$. Since thermal noise is a broad-band forcing, any satisfactory KF-receptivity model must account for a disturbance wavepacket and not just the single most amplified wave.

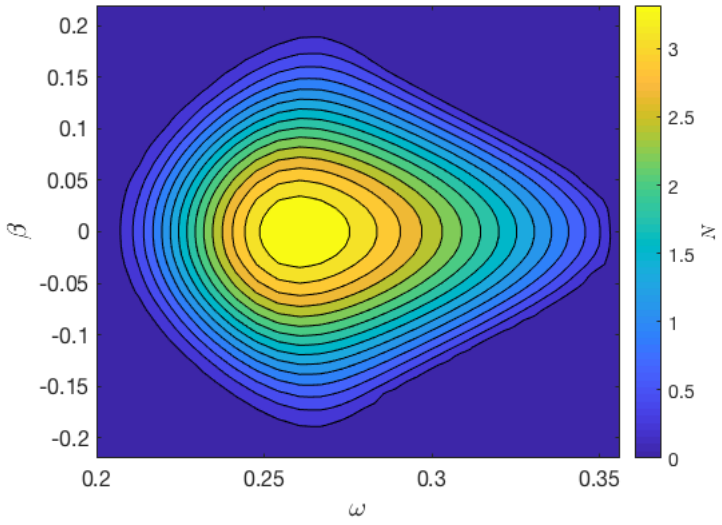


FIGURE 2.6. Spectral amplification $N(\omega, \beta)$ at $R = 4000$ for the Mach 6 test case.

# Chapter 3

# Real Gas Effects on Receptivity to KF

## 3.1 Introduction

Previous studies of receptivity to KF in high-speed boundary layers have been restricted by the assumption of a calorically perfect (CP) gas [60, 61, 39, 31]. This is acceptable for moderate enthalpy configurations where the variation of the specific heats with temperature is not substantial. On the other hand, it is expected that the boundary layer associated with aircraft operating at sustained hypersonic speeds will be characterized by high total enthalpy [48]. In such flows, the variation of the specific heats with temperature may become significant, and in extreme cases, the role of molecular dissociation must be taken into account. An understanding of KF-receptivity for high speed aircraft thus requires characterization of these so called 'real gas effects'.

Because there are significant difficulties in extending models of KF receptivity to boundary layers in real gas [63], this work utilizes a combination of real gas and calorically perfect gas assumptions. In particular, we adopt an approach in which the boundary layer mean flow profiles are computed using a 5-species model for air, while the CP gas assumption is maintained in the stability and receptivity calculations. This requires specification of constant effective parameters $\gamma_{eff}$ and $Pr_{eff}$ for the latter calculations. In what follows we describe the approach in detail and demonstrate its validity for configurations in which no significant dissociation occurs. Throughout this chapter we use the shorthand 'Air/CP', for example, where the first label refers to the mean flow model and the second to the stability model. The present Air/CP approach adopted herein is compared to results based on a CP/CP model as a first step towards identifying the importance of real gas effects in KF-receptivity

and hydrodynamic stability at realistic flight conditions.

The method for solving the receptivity problem in this chapter is the one developed by Fedorov and Tumin in Ref. [39]. The idea is adapted from earlier work on receptivity to deterministic forcing such as vibrations or temperature spots located on the wall [34]. The main assumptions of the approach are that (1) the disturbance induced by KF may be expressed in terms of the dominant unstable mode of the discrete spectrum (single-mode approximation), and (2) that waves associated with this mode are excited in a small neighborhood of the instability onset. Downstream of the excitation region, amplification occurs over a region with length on the order of the plate itself. The evolution of the disturbance is captured by matching an inner solution which completely accounts for initial excitation by KF to an outer solution characterizing the downstream amplification of the mode. For convenience, this approach will be referred to as the matched asymptotic (MA) approach throughout this dissertation. An exposition of the MA approach for solving the problem of receptivity to KF is provided in §3.3.

This Chapter begins with a validation of the combined Air/CP methodology adopted in this work to study real gas effects. We then give a detailed exposition of the MA receptivity solution developed by Fedorov and Tumin [39], making an effort to elaborate on components that are unclear or unaddressed in the literature. We then compare results based on the CP/CP and Air/CP models for two high-enthalpy configurations relevant for sustained hypersonic flight. Significant attention is paid to the appearance of so called 'supersonic unstable modes', which arise in connection with real gas effects. We conclude with a discussion of the limitations of the MA approach which serve as motivation for the work presented in Chapter 4.

## 3.2 Methodology

The real gas mean flow model used in this work is a model for air consisting of five species: $O_2$, $N_2$, $NO$, $N$ and $O$. The thermodynamic and transport properties are computed along the lines of Ref. [43]. The details of the numerical solver are provided in Ref. [20]. The fundamental difference between the real gas 'Air' model and the CP model is the dependence of the specific heats on temperature and species concentration. The CP mean flow model is that described in Chapter 2.

The goal of the present work is to consider flat plate boundary layer configurations which are relevant for actual sustained hypersonic flight conditions. Future heat insulation materials are expected to be effective up to $2000 - 2500$ K. Using this constraint along with general knowledge of the operating speeds of prospective hypersonic aircraft ($3 - 6\,\mathrm{km/s}$), configurations which are practically relevant for the design of future aircraft may be determined. Eight such configurations were proposed in Ref. [48], based on proposed reusable hypersonic cruise vehicles (HCV) capable of reaching any point on the globe within 1-2 hours. The authors suggested considering flows with total enthalpy in the range $4.5 - 18\,\mathrm{MJ/kg}$. To emphasize the role of real gas effects, which depend on the total enthalpy and pressure of the flow, we consider two cases, Case 1 and Case 3 (in the language of Ref. [48]), for which the total enthalpy is $5.60\,\mathrm{MJ/kg}$ and $16.53\,\mathrm{MJ/kg}$, respectively. The corresponding flow parameters are provided in Table 3.1. For each case, we consider two wall temperatures, $T_w = 1000\,\mathrm{K}$ and $T_w = 2000\,\mathrm{K}$. For the cases considered, dissociation is not significant and the mean flow profiles are self-similar.

| | $T_e^*$ (K) | $U_e^*$ (m/s) | $M_e$ | $P_e^*$ (atm) | $I^*$ (MJ/kg) |
|---|---|---|---|---|---|
| Case 1 | 278 | $3.351 \times 10^3$ | 10.00 | 0.0433 | 5.60 |
| Case 3 | 834 | $5.648 \times 10^3$ | 9.91 | 0.0433 | 16.53 |

TABLE 3.1. Details of the flow properties for Cases 1 and 3 from Ref. [49]

In a calorically perfect gas, the Prandtl number and specific heats are constant.

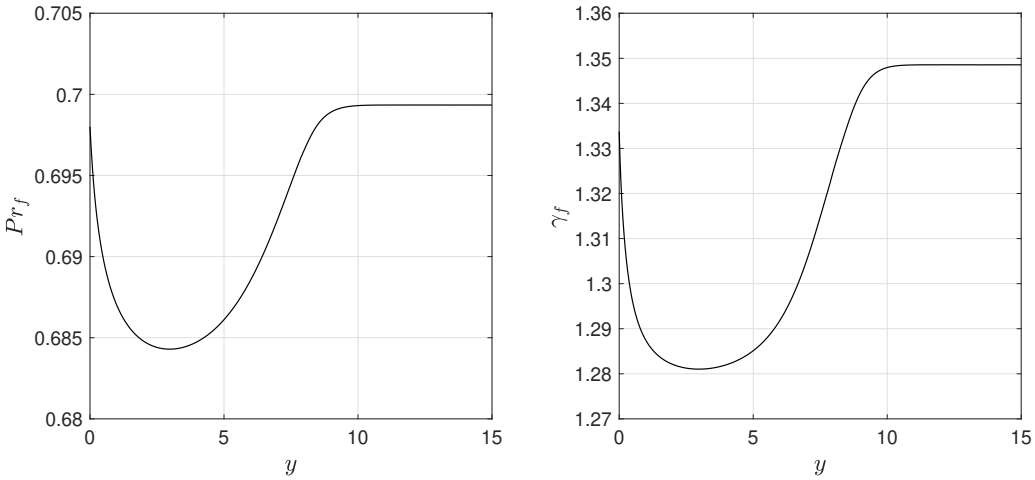


FIGURE 3.1. Variation of $Pr$ and $\gamma$ under the Air model, Case 3, $T_w = 1000$.

For Case 3, the flow conditions result in specific heats ratio $\gamma = 1.35$ and Prandtl number $Pr = 0.70$, determined using the thermodynamic and transport properties of Ref. [43]. In the Air model, these quantities vary as functions of the frozen specific heat $c_{p,f}$ which in turn depends on temperature and species concentration. Here the term 'frozen' indicates the value of the indicated quantity for a fixed chemical composition. The frozen specific heats, for example, is found as a weighted average of the specific heats of each individual species according to the corresponding mass fractions at a given instance. The frozen Prandtl number $Pr_f$ and specific heats ratio $\gamma_f$ for Case 3, $T_w = 1000$ are plotted as functions of the wall normal coordinate in Figure 3.1. The mean temperature and streamwise velocity profiles for this case under both the Air and the CP model are shown in Figure 3.2a. The Air model results in mean temperatures which are lower through the boundary layer than those predicted by the CP model. This phenomenon can be largely attributed to the variation of the frozen specific heat $c_{p,f}$ with temperature. As the heat capacity drops (Figure 3.1b), more energy is required to increase the temperature of the gas, and the temperatures attained are not as high.

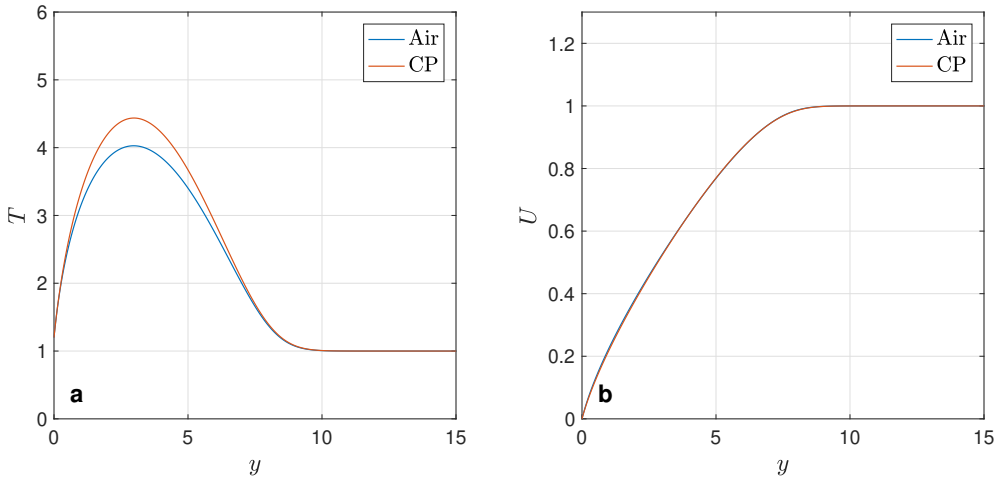


FIGURE 3.2. Mean temperature and streamwise velocity profiles under the Air and CP models for Case 3, $T_w = 1000$.

In the Air/CP approach adopted in this work, we assume an Air model only in computing the mean flow; the CP assumption is maintained in the stability and receptivity calculations. To proceed in this fashion, we must fix effective quantities $\gamma_{eff}$ and $Pr_{eff}$ for the stability and receptivity calculations. Because we expect the receptivity mechanism to be localized near the edge of the boundary layer, it is reasonable to set $\gamma_{eff}$ and $Pr_{eff}$ equal to the free stream values of $\gamma_f$ and $Pr_f$. Because these limiting values are equal to $\gamma$ and $Pr$ under the CP model, this lends a consistency to the stability calculations. In any case, the choice of $Pr_{eff}$ and $\gamma_{eff}$ across the dynamic range predicted by the Air model does not have a strong effect on the stability of the dominant mode. Figure 3.3 shows the unstable portion of the growth rate corresponding to frequency parameter $F = 40.0 \times 10^{-6}$ for two choices of these parameters. In the first case the effective parameters are set to the value of the frozen parameters at the boundary layer edge, in the second they are set to the minimum value of their dynamic range which occurs around $y^*/\Delta^* = 3$. The effect is seen to be negligible, particularly for $R < 5000$, after which point waves

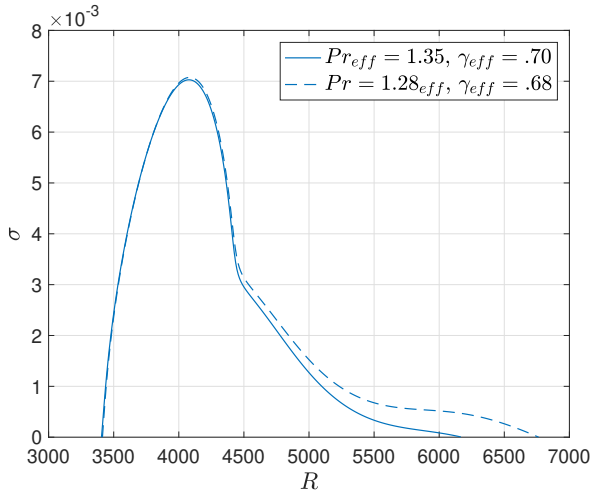


FIGURE 3.3. Growth rate for Case 3, $T_w = 1000$, $F = 4.0 \times 10^{-5}$ under the Air/CP model for two choices of $Pr_{eff}$ and $\gamma_{eff}$.

of lower frequency begin to dominate anyway. In other words, the small additional amplification indicated by the dashed line has minimal effect on the $N$-factor envelope. For all cases considered in this work, we set $\gamma_{eff}$ and $Pr_{eff}$ equal to the value of the corresponding frozen parameter in the free stream.

As a further validation of the Air/CP approach, we compare the behavior of the dominant mode for three different modeling approaches: CP/CP, Air/CP, and Air/Air. The real gas (Air) stability solver used in these comparisons is detailed in Ref. [48]. Figure 3.4 shows a comparison of the real part of the phase speed $c_r$ and the growth rate $\sigma$ for the unstable mode corresponding to $F = 40.0 \times 10^{-6}$. There is close qualitative and quantitative agreement between the cases where the mean flow has been computed based on the Air model. When the mean flow is computed using the CP model, the evolution of the mode is quantitatively and qualitatively different. This suggests that the dominant effect comes from the choice of mean flow model rather than the model adopted for the stability computations. A similar trend is observed across all cases considered herein.

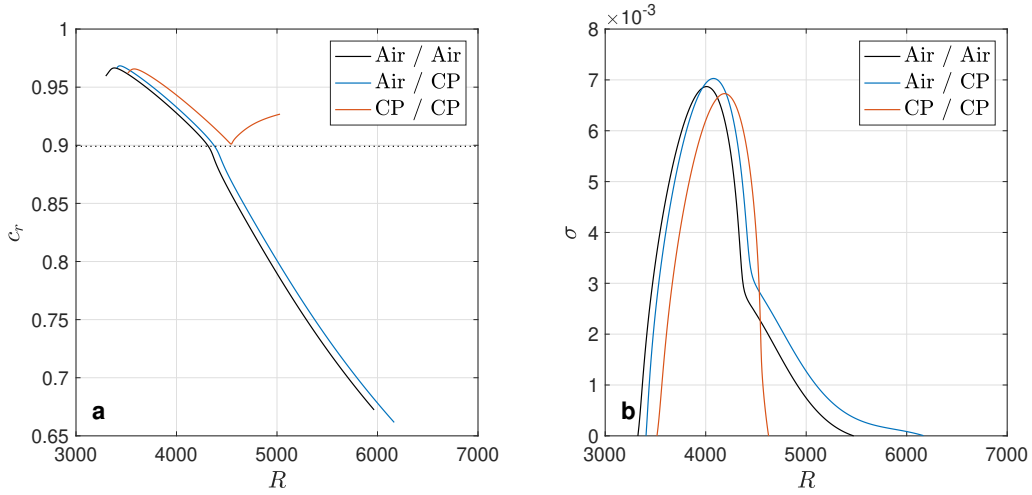


FIGURE 3.4. Case 3, $T_w = 1000$: a) Phase speed $c_r$ and b) growth rate $\sigma$ under three different models.

Finally, the 'tail' that appears in the growth rates associated with the Air mean flow model in Figures 3.3 and 3.4b is associated with a branching of the discrete spectrum. This branching is associated with the onset of so called 'supersonic unstable modes'. This phenomenon, which has physical implications as well as implications for the applicability and the interpretation of conventional LST, is discussed in detail in Section 3.4 in the context of Case 3.

## 3.3 Solution to the receptivity problem

In this section, we provide a detailed exposition of the receptivity solution developed in Ref. [39]. The notation herein is largely consistent with that work, but some small changes have been adopted for the sake of clarity. We begin with the transformed linearized non-parallel boundary layer disturbance equations with forcing due to kinetic

fluctuations

$$\begin{gathered}\mathrm{H}^{(np)}(y,\partial_y,x_1,\epsilon\partial_{x_1},\omega,\beta)\hat{\boldsymbol{F}}=\hat{\boldsymbol{G}}^{(L)},\\ y=0:\hat{F}_i=0,\ \ i=1,3,5,7,\\ y\to\infty:|\hat{F}_i|<\infty,\ \ i=1,3,5,7.\end{gathered}\tag{3.3.1}$$

The solution to the receptivity problem is based on a single-mode approximation where it is assumed that the KF-induced disturbance can be expressed in terms of the dominant unstable discrete mode. The solution strategy is motivated by the idea that the most effective excitation of the unstable mode occurs in a small neighborhood of the instability onset. The evolution of the mode is understood by splitting the streamwise domain into an inner excitation region centered about the neutral point $x_{10}$ and an outer $O(1)$ region over which the mode is amplified. An asymptotic matching of the solutions at the edge of the excitation region then yields a full description of the initial excitation and subsequent amplification of the mode. The outer solution is expressed in the form of the WKB type ansatz

$$\hat{\boldsymbol{F}}(x_1,y)=C(x_1)\boldsymbol{A}^{(0)}(x_1,y)K(x_1),\qquad K=\exp\left(i\epsilon^{-1}\int^{x_1}\alpha(x_1')\mathrm{d}x_1'\right).\tag{3.3.2}$$

Upon Taylor expanding the eigenvalue trajectory of the unstable mode about the neutral point, it can be shown that dominant excitation occurs in the neighborhood

$$x_1-x_{10}=O\left(\sqrt{\frac{\epsilon}{|\sigma_{x_{10}}|}}\right),\tag{3.3.3}$$

where $\sigma_{x_{10}}$ is the derivative of the growth rate at the neutral point. Assuming the eigenvalue $\alpha$ is a slow function of $x_1$, we have $\sigma_{x_{10}}=O(1)$ and condition (3.3.3) reduces to simply $x_1-x_{10}=O\left(\epsilon^{1/2}\right)$, or, equivalently, $x-x_0=O\left(\epsilon^{-1/2}\right)$. In this case, forcing wavenumbers in the range

$$\alpha_f-\alpha_0=O\left(\epsilon^{1/2}\right)\tag{3.3.4}$$

will contribute to the excitation phenomenon. A more detailed explanation of the preceding statements is provided in Appendix A.1. We proceed by considering forcing

wavenumbers $\alpha_f = \alpha_0 + \epsilon^{1/2}\gamma$, where $\gamma = O(1)$ is a parameter reflecting detuning from pure resonance. In light of the excitation region width, we introduce the inner variable $\xi$ defined by $\xi = \epsilon^{-1/2}(x_1 - x_{10})$. The forcing due to KF is then expressed in the form

$$\hat{\boldsymbol{G}}^{(L)} = \hat{\boldsymbol{G}}^{(L)}_{\alpha} \exp\left(i\epsilon^{-1}\alpha_f(x_1 - x_{10})\right) \tag{3.3.5}$$

$$= \hat{\boldsymbol{G}}^{(L)}_{\alpha} \exp\left(i\epsilon^{-1/2}\xi\alpha_0 + i\gamma\xi\right), \tag{3.3.6}$$

where $\hat{\boldsymbol{G}}^{(L)}_{\alpha}$ is defined as the local Fourier transform

$$\hat{\boldsymbol{G}}^{(L)}_{\alpha} = \int_{-\infty}^{\infty} \hat{\boldsymbol{G}}^{(L)} e^{-i\alpha(x-x_0)} \mathrm{d}x. \tag{3.3.7}$$

In the vicinity of the neutral point, the eigenvalue of the unstable mode is expanded as $\alpha = \alpha_0 + b(x_1 - x_{10})$, $b = \mathrm{d}\alpha/\mathrm{d}x_1$. The ansatz in the inner excitation region may be expressed as

$$\hat{\boldsymbol{F}}_{\gamma} = \left[\epsilon^{-1/2} c_{\gamma}(x_1)\boldsymbol{A}^{(0)}(y) + \boldsymbol{A}^{(1)}(x_1, y) + \cdots\right] \exp\left(i\epsilon^{-1/2}\xi\alpha_0\right). \tag{3.3.8}$$

To lead order, the full solution in the inner region is then given by

$$\hat{\boldsymbol{F}} = \frac{\epsilon^{1/2}}{2\pi} \int_{-\infty}^{\infty} \hat{\boldsymbol{F}}_{\gamma} \mathrm{d}\gamma \tag{3.3.9}$$

$$= \frac{1}{2\pi} \int_{-\infty}^{\infty} c_{\gamma}(x_1)\mathrm{d}\gamma\, \boldsymbol{A}^{(0)}(y) \exp\left(i\epsilon^{-1/2}\xi\alpha_0\right), \tag{3.3.10}$$

where the integral in $\gamma$ accounts for all forcing components contributing to excitation of the unstable mode. Expanding the problem about the neutral point and inserting the ansatz (3.3.8) yields, at $O(1)$,

$$\mathcal{L}_0 \boldsymbol{A}^{(1)} = -i\frac{\partial \mathrm{H}_{00}}{\partial \alpha}\frac{\mathrm{d}c_{\gamma}}{\mathrm{d}\xi}\boldsymbol{A}^{(0)} + c_{\gamma}\xi\frac{\partial \mathrm{H}_{00}}{\partial x_1}\boldsymbol{A}^{(0)} + \hat{\boldsymbol{G}}^{(L)}_{\alpha}\exp(i\gamma\xi) \tag{3.3.11}$$

where we have divided through by $\exp\left(i\epsilon^{-1/2}\xi\alpha_0\right)$. For equation (3.3.11) to have a non-trivial solution, the right hand side must be orthogonal to the adjoint eigenfunction $\boldsymbol{B}^{(0)}$. Enforcing this solvability condition yields

$$-i\frac{\mathrm{d}c_{\gamma}}{\mathrm{d}\xi}\left\langle\frac{\partial \mathrm{H}_{00}}{\partial \alpha}\boldsymbol{A}^{(0)}, \boldsymbol{B}^{(0)}\right\rangle + c_{\gamma}\xi\left\langle\frac{\partial \mathrm{H}_{00}}{\partial x_1}\boldsymbol{A}^{(0)}, \boldsymbol{B}^{(0)}\right\rangle + \left\langle\hat{\boldsymbol{G}}^{(L)}_{\alpha}, \boldsymbol{B}^{(0)}\right\rangle\exp(i\gamma\xi) = 0. \tag{3.3.12}$$

By differentiating the LST eigenvalue problem (2.3.15) in $x_1$ (recall that the mean flow, the eigenvalue and the eigenfunctions are slow functions of $x_1$) and applying the solvability condition to the result we obtain the useful identity

$$-b\left\langle \frac{\partial \mathrm{H}_{00}}{\partial \alpha}\boldsymbol{A}^{(0)}, \boldsymbol{B}^{(0)} \right\rangle = \left\langle \frac{\partial \mathrm{H}_{00}}{\partial x_1}\boldsymbol{A}^{(0)}, \boldsymbol{B}^{(0)} \right\rangle. \tag{3.3.13}$$

Using this expression in (3.3.12) allows for the ODE governing $c_\gamma$ to be expressed concisely in the form

$$c_\gamma' - ib\xi c_\gamma = q\exp(i\gamma\xi), \tag{3.3.14}$$

$$q = i\Gamma^{-1}\left\langle \hat{\boldsymbol{G}}_\alpha^{(L)}, \boldsymbol{B}^{(0)} \right\rangle \tag{3.3.15}$$

where the scalar product $\Gamma$ is evaluated at the neutral point

$$\Gamma = \left\langle \frac{\partial \mathrm{H}_{00}}{\partial \alpha}(x_{10}, \alpha_0)\boldsymbol{A}^{(0)}, \boldsymbol{B}^{(0)} \right\rangle. \tag{3.3.16}$$

Equation (3.3.14) may be solved explicitly to obtain

$$c_\gamma = \exp\left(-\frac{ib\xi^2}{2}\right)\int_{-\infty}^{\xi} q\exp\left(i\gamma\xi' - \frac{ib\xi'^2}{2}\right)\mathrm{d}\xi' \tag{3.3.17}$$

where we have assumed the mode has zero amplitude at $\xi \to -\infty$, upstream of the excitation region. The integral in (3.3.17) may be approximated using the method of stationary phase. The dominant contribution to the integral comes from the region of the stationary point $\xi_0 = \gamma/b$ determined by

$$\frac{\partial}{\partial \xi}\left(i\gamma\xi - \frac{ib\xi^2}{2}\right) = 0. \tag{3.3.18}$$

This approximation yields

$$c_\gamma \approx q\exp\left(\frac{ib\xi^2}{2}\right)\exp\left(\frac{i\gamma^2}{2b}\right)\int_{-\infty}^{\infty}\exp\left(-\frac{ib}{2}(\xi-\xi_0)^2\right)\mathrm{d}\xi \tag{3.3.19}$$

$$= q\sqrt{\frac{2\pi i}{b}}\exp\left(\frac{ib\xi^2}{2} + \frac{i\gamma^2}{2b}\right). \tag{3.3.20}$$

Integrating in $\gamma$ we obtain

$$\frac{1}{2\pi}\int_{-\infty}^{\infty} c_\gamma \,\mathrm{d}\gamma = \frac{1}{2\pi}\sqrt{\frac{2\pi i}{b}}\exp\left(\frac{ib\xi^2}{2}\right)\int_{-\infty}^{\infty} q\exp\left(\frac{i\gamma^2}{2b}\right)\mathrm{d}\gamma. \tag{3.3.21}$$

Inserting this into the inner solution (3.3.10) yields

$$\hat{\boldsymbol{F}} = \frac{1}{2\pi}\sqrt{\frac{2\pi i}{b}}\int_{-\infty}^{\infty} q\exp\left(\frac{i\gamma^2}{2b}\right)\mathrm{d}\gamma\boldsymbol{A}^{(0)}(y)\exp\left(i\epsilon^{-1/2}\xi\alpha_0 + \frac{ib\xi^2}{2}\right). \tag{3.3.22}$$

The exponent of $K$, defined in (3.3.2), is asymptotic to that of (3.3.22) as $x_1 \to x_{10}^+$. Thus, comparing (3.3.22) with the outer solution (3.3.2), we determine the excitation coefficient $C$ to be

$$C = \frac{1}{2\pi}\sqrt{\frac{2\pi i}{b}}\int_{-\infty}^{\infty} q\exp\left(\frac{i\gamma^2}{2b}\right)\mathrm{d}\gamma. \tag{3.3.23}$$

Because the quantity $q$ depends on the random forcing due to KF, $C$ is also a random quantity. A physically meaningful expression for the amplitude of the induced disturbance may be determined as the root mean square amplitude of the KF-induced wavepacket. To this end, the mean-square of the amplitude $C$ may be found as

$$\overline{CC^*} = \frac{1}{(2\pi)^2}\frac{2\pi}{|b|}\int_{-\infty}^{\infty}\int_{-\infty}^{\infty}\overline{qq^*}\exp\left(\frac{i\gamma^2}{2b} - \frac{i\gamma'^2}{2b^*}\right)\mathrm{d}\gamma\mathrm{d}\gamma'. \tag{3.3.24}$$

Using expressions (2.1.10)-(2.1.11) for the correlation of the fluctuating dissipative fluxes, the mean square of $q$ may be expressed as

$$\overline{qq^*} = (2\pi)^3(q^2)_{\alpha,\beta,\omega}\delta(\alpha-\alpha')\delta(\beta-\beta')\delta(\omega-\omega') \tag{3.3.25}$$

where details of this calculation and the elements of $(q^2)_{\alpha,\beta,\omega}$ are provided in Appendix A.2. In deriving (3.3.25), integration by parts has been employed to transfer derivatives in $y$ onto the adjoint eigenfunctions $\boldsymbol{B}^{(0)}$. Using $\delta(\alpha-\alpha') = \epsilon^{-1/2}\delta(\gamma-\gamma')$, we have

$$\overline{CC^*} = \frac{\epsilon^{-1/2}}{(2\pi)^2}\frac{2\pi}{|b|}\int_{-\infty}^{\infty}(q^2)_{\alpha,\beta,\omega}(x_{10})\exp\left(-\frac{\gamma^2\sigma_{x_{10}}}{2|b|^2}\right)\mathrm{d}\gamma(2\pi)^3\delta(\beta-\beta')\delta(\omega-\omega') \tag{3.3.26}$$

$$= (2\pi)^2\sqrt{\frac{\pi}{\sigma_{x_0}}}(q^2)_{\alpha,\beta,\omega}(x_{10})\delta(\beta-\beta')\delta(\omega-\omega'). \tag{3.3.27}$$

where in moving from the first to the second line we have used $\epsilon\sigma_{x_{10}} = \sigma_{x_0}$. In the interest of quantifying a physical disturbance, the eigenfunction $\boldsymbol{A}^{(0)}$ in the outer solution (3.3.2) may be replaced with one of its components, for example, the pressure disturbance $A_4^{(0)}(x_1, y, \omega, \beta)$. Of particular interest for hypersonic applications is the disturbance pressure on the wall $\hat{f}_A(x_1, \omega, \beta) = A_4^{(0)}(x_1, y = 0, \omega, \beta)$. If the eigenfunction is normalized so that the pressure disturbance is unity on the wall, $\hat{f}_A = 1$, then the physical disturbance $f = p_w^*/P_e^*$ induced by kinetic fluctuations is given by

$$f(x_1) = \frac{2\epsilon_L}{(2\pi)^2} \int_0^\infty \int_{-\infty}^\infty C(x_1, \omega, \beta) K(x_1, \omega, \beta) e^{i(\omega t - \beta z)} \mathrm{d}\omega \mathrm{d}\beta, \tag{3.3.28}$$

where we have used the symmetry in $\beta$ to change the lower bound of the integral to 0. The mean-square of $f$, accounting for (3.3.27), is given by

$$\overline{|f|^2} = \frac{\epsilon_L^2}{2\pi^2} \int_0^\infty \int_{-\infty}^\infty \sqrt{\frac{\pi}{\sigma_{x_0}}} (q^2)_{\alpha,\beta,\omega}(x_{10}) e^{2N(x_1,\omega,\beta)} \mathrm{d}\omega \mathrm{d}\beta, \tag{3.3.29}$$

where we have used that $|K(x_1)|^2 = \exp(2N(x_1))$ with the standard definition

$$N(x_1) = \epsilon^{-1} \int_{x_{10}}^{x_1} \sigma(x_1') \mathrm{d}x_1', \quad \sigma = -\Im[\alpha]. \tag{3.3.30}$$

The integrals in (3.3.29) may be computed numerically, but a far more efficient approach is to approximate them asymptotically via Laplace's method [106, 5]. This is feasible since $N$ exhibits a unique maximum in the $(\omega, \beta)$-plane and may be assumed large, particularly downstream from the leading edge region. This leads to the compact asymptotic formula

$$\overline{|f|^2} = \frac{\epsilon_L^2}{2\pi} \left( \sqrt{\frac{\pi}{\sigma_{x_0}}} \frac{(q^2)_{\alpha,\beta,\omega}(x_{10}) e^{2N(x_1,\omega,\beta)}}{\sqrt{\left| N_{\omega\omega} N_{\beta\beta} - N_{\omega\beta}^2 \right|}} \right) \Bigg|_{\max}, \tag{3.3.31}$$

where the quantity in parenthesis is evaluated at the maximally amplified frequency $\omega = \omega_{\max}$ and span-wise wavenumber $\beta = \beta_{\max}$ corresponding to the observation point $x_1$. $N_{\omega\omega}$, $N_{\beta\beta}$, and $N_{\omega\beta}$ represent second derivatives of $N$ with respect to the

indicated variables. For the high Mach number cases considered in this chapter, the maximally amplified waves at any location correspond to $\beta_{\max} = 0$, and thus $N_{\omega\beta} = 0$. In Chapter 4, the validity of the Laplace approximation of the Fourier inversion integrals is confirmed for a range of low and high speed range configurations. In this chapter, the magnitude of the KF-induced disturbance will be computed based on the computationally efficient formula (3.3.31).

The spectral density $(q^2)_{\alpha,\beta,\omega}$ evaluated at the neutral point may be expressed as

$$(q^2)_{\alpha,\beta,\omega} = \int_0^\infty \mathcal{R}(y)\,\mathrm{d}y, \tag{3.3.32}$$

$$\mathcal{R} = \left(\sum_{k=2,4,6,8} \mathcal{R}_{kk}\right) + 2\Re\left[\mathcal{R}_{24} + \mathcal{R}_{26} + \mathcal{R}_{28} + \mathcal{R}_{46} + \mathcal{R}_{48} + \mathcal{R}_{68}\right] \tag{3.3.33}$$

where the $\mathcal{R}_{jk}$ are defined via the expression

$$\overline{|\Gamma|^{-2} \int_0^\infty \int_0^\infty B_j^{(0)}(y) G_j(y) B_k^{(0)*}(y') G_k^*(y') \mathrm{d}y \mathrm{d}y'} = (2\pi)^3 \delta(\alpha - \alpha')\delta(\beta - \beta')\delta(\omega - \omega') \int_0^\infty \mathcal{R}_{jk}\,\mathrm{d}y, \tag{3.3.34}$$

and $G_j$ are the elements of the transformed stochastic forcing vector $\hat{\boldsymbol{G}}_\alpha^{(L)}$, provided in Appendix A.2. (Odd indices do not appear in (3.3.33) because $G_j = 0$ for $j = 1, 3, 5, 7$). The function $\mathcal{R}$ and its components $\mathcal{R}_{jk}$ are used to examine the distribution of the receptivity mechanism in the wall-normal direction in Section 3.4.1.

## 3.4 Results

In this section we present results for two high-enthalpy flat plate boundary layer configurations, Case 1 and Case 3, with flow conditions provided in 3.1. In each case we consider wall temperatures $T_w = 1000$ and $T_w = 2000$. The role of real gas effects is explored through comparison of results based on the CP/CP and Air/CP modeling

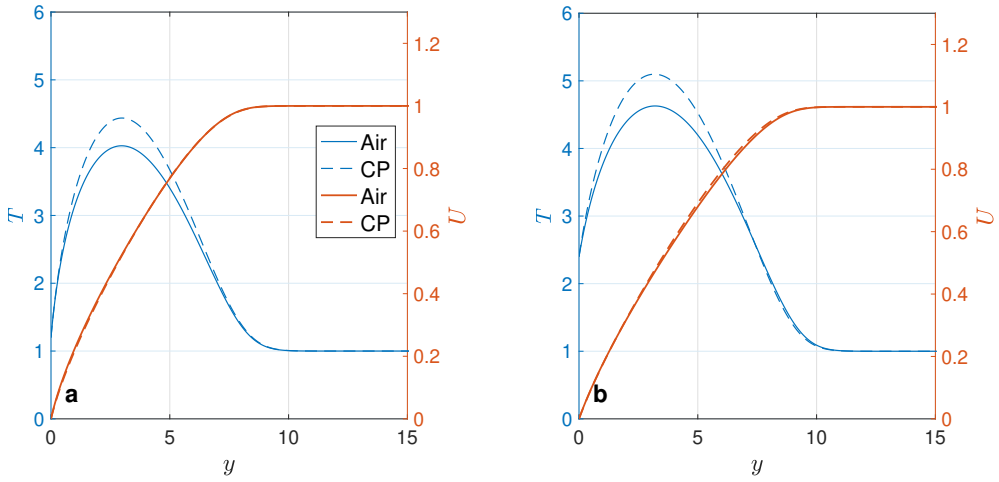


FIGURE 3.5. Case 3: Mean temperature and streamwise velocity profiles for a) $T_w = 1000$ and b) $T_w = 2000$ under the Air and CP models.

approaches. We begin by discussing Case 3 in significant detail, with a particular focus on wall temperature $T_w = 2000$. Case 1 is discussed last and challenges associated with analyzing this case serve to directly motivate the work in the subsequent chapter.

### 3.4.1 Case 3: $T_e = 834\,\text{K}$, $P_e = 0.0433\,\text{atm}$, $U_e = 5.648\,\text{km/s}$, $M_e = 9.91$

Figure 3.5a provides a comparison of the mean temperature and streamwise velocity profiles under the CP and Air models for Case 3, $T_w = 1000$ K. Figure 3.5b provides the same for wall temperature $T_w = 2000$ K. In both cases, real gas effects are primarily manifested through a lower mean temperature profile as discussed earlier. The discrepancy in the profiles between the two gas models is greatest near the center of the boundary layer and becomes negligible towards the edge. This is significant because for hypersonic speeds ($M \approx 6$), the KF-receptivity mechanism is localized in the critical layer $y_c$ which lies near the boundary layer edge [39].

Our results demonstrate that this trend persists for the higher Mach number configurations of interest here. As a consequence, the agreement in the mean flow

profiles predicted by the Air and CP models near the boundary layer edge leads to comparable KF-receptivity. This is demonstrated in Figure 3.6a which shows $\mathcal{R}$, defined in (3.3.33), overlaid on the mean temperature profile for both the Air/CP and CP/CP models. This quantity can be interpreted as the effectiveness of KF in capitalizing on the sensitivity of the boundary layer in the wall-normal dimension at the neutral point. The figure corresponds to the neutral point location $R = 6114$ for $F = 2.0 \times 10^{-5}$ and $\beta = 0$. Receptivity is similar qualitatively and quantitatively between the two models and exhibits a strong peak in the critical layer $y_c \approx 8$. We emphasize that the behavior observed in Figure 3.6a, which corresponds to a single wave at a single streamwise location, is representative of the behavior observed across the range of physically relevant parameters for this case. A more complete picture of the receptivity phenomenon is made possible in Chapter 4 by the methods developed therein.

The shape of $\mathcal{R}$ reflects the shape of the adjoint eigenfunctions and their wall-normal derivatives, which also exhibit peaks in the critical layer. In both cases the dominant contribution to the integrand comes from the term labeled $\mathcal{R}_{22}$ (see (3.3.33)) which is associated with the fluctuating shear stress in the $x$-momentum equation. Figure 3.6b shows that for the Air/CP model, the strong peak in $\mathcal{R}$ is due almost entirely to component $\mathcal{R}_{22}$. Similar behavior is observed for the CP/CP model, and, in fact, for all other cases considered in this chapter.

As alluded to in Section 3.2, a new feature arises in the dispersion curve of the unstable mode for Case 3 which complicates the traditional LST analysis. Figure 3.7 shows the unstable mode growth rate and the complex phase speed trajectory corresponding to two frequencies for wall temperature $T_w = 2000$ under the Air/CP model. As the frequency parameter drops from $F = 2.73 \times 10^{-5}$ to $F = 2.72 \times 10^{-5}$, there is a discontinuous qualitative shift in the dispersion curve that is associated with a branching of the discrete spectrum. The vertical dashed line in Figure 3.7b marks the sonic line $c_r = 1 - 1/M$. While $c_r > 1 - 1/M$, the mode corresponds to

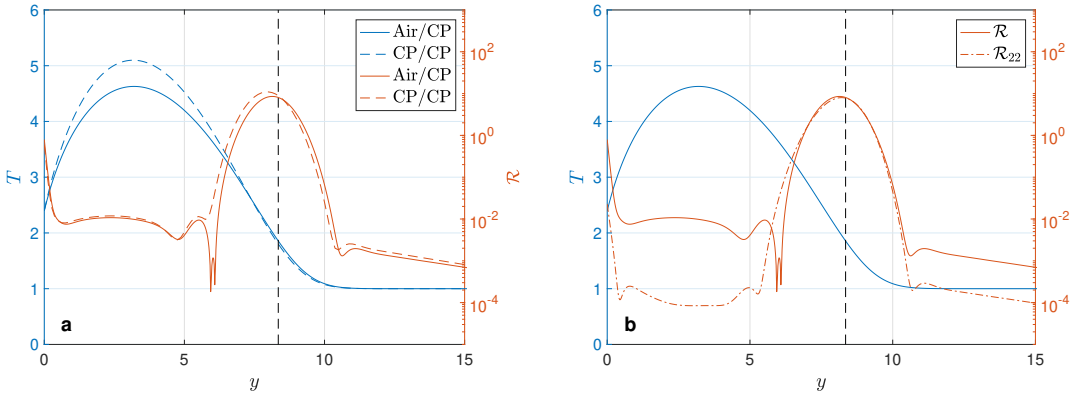


FIGURE 3.6. (a) Mean temperature profiles overlaid on the integrand of $(q^2)_{\alpha,\beta,\omega}$ under models Air/CP and CP/CP. (b) Comparison of the full integrand of $(q^2)_{\alpha,\beta,\omega}$ versus the component $j_{22}$ associated with shear stress in the $x$-momentum equation under the Air/CP model.

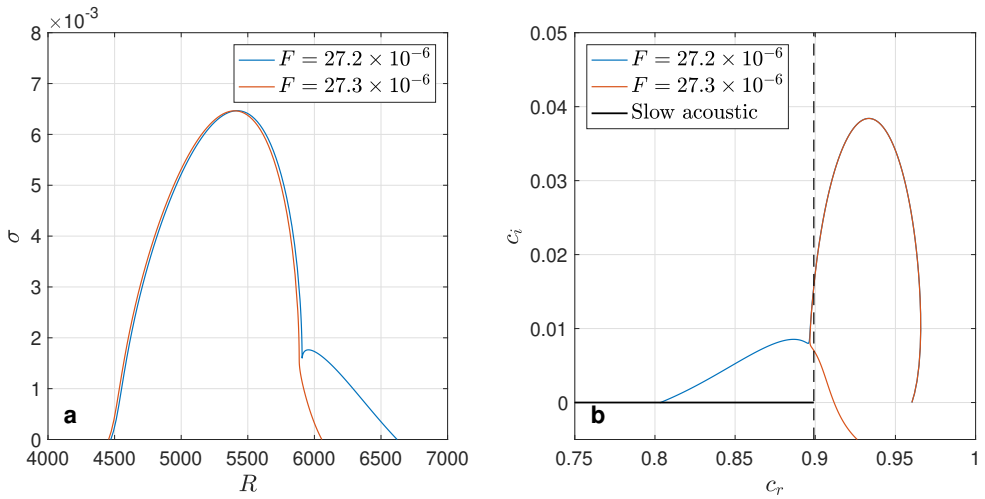


FIGURE 3.7. (a) Growth rate and (b) phase speed trajectory for Case 3, $T_w = 2000$, Air/CP.

waves traveling upstream subsonically relative to the free-stream velocity $U^*_\infty$. When $c_r < 1 - 1/M$, the waves are traveling supersonically relative to the free-stream. When the phase speed of a mode drops below the sonic line $c_r < 1 - 1/M$ it is thus referred to as supersonic. Downstream, unstable supersonic modes coalesce with the upper side of the branch cut associated with slow acoustic waves, after which point the mode ceases to exist.

It has been emphasized recently that the appearance of supersonic modes is associated with a phase speed synchronization between the unstable discrete mode waves and slow acoustic waves of the continuous spectrum [8, 13]. This explanation may be correct in certain cases, however, in the present case, the phenomenon is connected to a coalescence of the unstable mode with another mode of the discrete spectrum. As such, there is a complex branch point Reynolds number $R_{\text{br}}$ which may be associated with the phenomenon. This idea was introduced in Chapter 2 in the context of the coalescence of modes S and F near the instability onset. Before exploring the implications of supersonic unstable modes, we leverage the notion of the branch point Reynolds number to highlight the discrepancy in the predictions of the Air/CP model versus the CP/CP model.

As is the case for the synchronization of modes S and F, the topology of the eigenvalue dispersion associated with supersonic modes depends on whether the associated complex branch point is bypassed from above or below along the real axis. Figure 3.8a shows $R_{\text{br}}$ as a function of $F$ For Case 3, $T_w = 2000$, under the Air/CP and CP/CP models. The onset of supersonic unstable modes in each case corresponds to the point where $R_{\text{br}}$ crosses the real axis from below as $F$ is decreased.

Figure 3.8b shows the $N$-factor $N = \int_{x_0}^{x} \sigma \, \mathrm{d}x$ as a function of frequency parameter $F$ at the point where the corresponding wave is maximally amplified. The solid dots indicate the location where $\Im[R_{\text{br}}] = 0$. For the CP/CP model, the $N$-factor is $N \approx 16.5$ just before the onset of unstable supersonic modes, likely outside the range of physically relevant values. For the Air/CP model on the other hand, waves of the

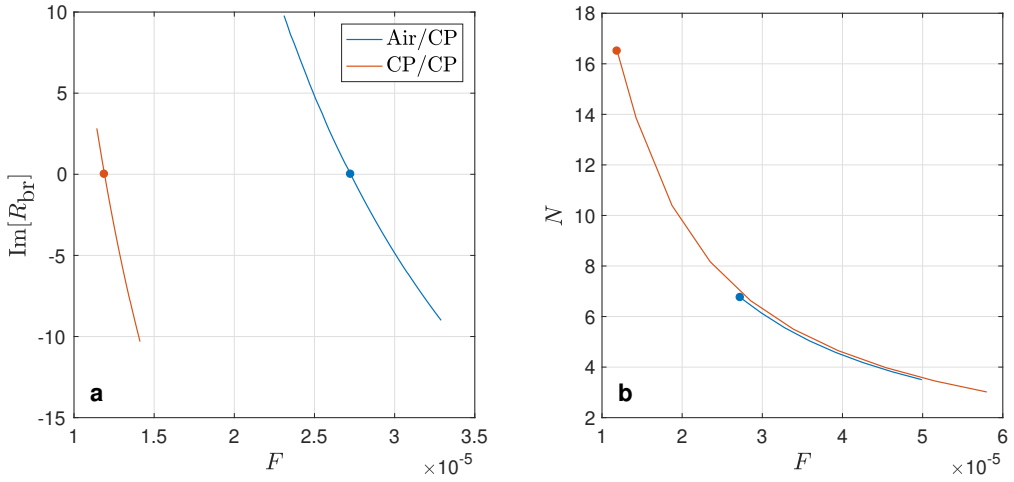


FIGURE 3.8. (a) Imaginary part of the complex branch point associated with the supersonic mode for Case 3, $T_w = 2000$ under both models. (b) $N$-factors.

dominant mode become supersonic further upstream where the $N$-factor is only about $N \approx 6.5$. Therefore, the Air/CP model suggests that, whatever their significance, supersonic modes must be understood and accounted for if LST is to be used to study laminar-turbulent transition at realistic flight conditions. In what follows, we use Case 3, $T_w = 2000$ under the Air/CP model as an example through which to understand the spectrum topology associated with the supersonic modes phenomenon.

Figure 3.9a shows the growth rates for mode S, mode F and a third previously unidentified mode of the discrete spectrum for frequency parameter $F = 2.71 \times 10^{-5}$. Near the transition of mode S from subsonic to supersonic, a new mode appears, becomes briefly unstable, and nearly coalesces with mode S. Because this new mode emanates from the slow acoustic branch of the continuous spectrum (as mode S does), we refer to it as mode S2. Downstream, mode S2 becomes stable and persists indefinitely while mode S coalesces with the continuous spectrum and ceases to exist. Figure 3.9b shows the real part of the discrete mode eigenvalues. Both mode S and mode F become supersonic downstream.

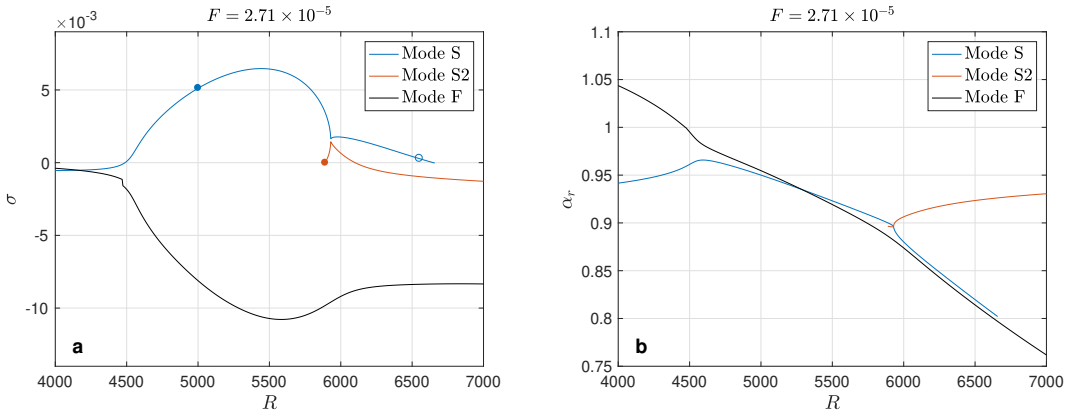


FIGURE 3.9. Case 3, $T_w = 2000$, Air/CP: a) Growth rates $\sigma = -\Im[\alpha]$ and b) $\Re[\alpha]$ for Modes S, S2, and F.

The topology observed in this case appears to be different from what has been observed elsewhere in the literature on supersonic modes. The difference may be due in part to the focus of other works on lower Mach number configurations and cases where the wall temperature ratio $T_w/T_e$ is much less than 1. In the present case the wall temperature ratio is $T_w/T_e \approx 2.4$. A consistent feature across all cases for which supersonic unstable modes have been observed is a small wall-to-adiabatic temperature ratio $T_w/T_{ad}$. In the present case, $T_w/T_{ad} = 0.16$.

The potential significance of the spectrum behavior in this case may be understood through considering the eigenfunctions associated with the unstable modes at the locations identified by dots in Figure 3.9. Figure 3.10 shows the absolute value of the pressure disturbance eigenfunctions which have been normalized to unity on the wall. At $R = 5000$, well before coalescence with the acoustic branch, the pressure disturbance associated with mode S decays rapidly outside of the boundary layer. Downstream, when mode S is close to the slow acoustic branch, the eigenfunction exhibits extremely slow decay, suggesting the potential for radiation of acoustic-like waves into the outer flow. Similar behavior is observed in the eigenfunction of mode S2 at the location indicated in Figure 3.9a. The local pressure disturbance field

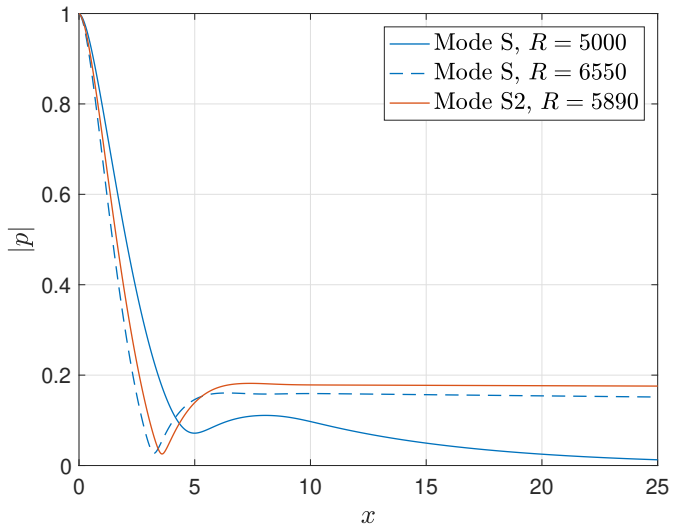


FIGURE 3.10. Case 3, $T_w = 2000$, Air/CP: Pressure disturbance eigenfunctions for modes S and S2 at the three locations indicated in Figure 3.9a.

associated with a mode for a particular choice of $\omega, \beta$ and $R$ may be visualized through plotting the quantity

$$\psi_p = \Re\left[p(y)\exp(i\alpha x)\right], \tag{3.4.1}$$

where $p = A_4$ is the component of the complex eigenfunction $\boldsymbol{A}$ associated with the pressure disturbance. Figures 3.11a-c show the local pressure disturbance field associated with mode S at (a) $R = 5000$ and (b) $R = 6550$ and (c) mode S2 at $R = 5890$. In all three cases, $F = 2.71 \times 10^{-5}$ and $\beta = 0$. The edge of the boundary layer $y \approx 9.1$ is indicated by the dashed red line. These plots suggest that if mode S and/or mode S2 are excited, there is potential for acoustic-like waves to be radiated well into the far field.

Indeed, Chuvakhov and Fedorov [13] recently demonstrated through DNS that wave packets of supersonic 2nd Mack modes in a cold wall boundary layer ($T_w/T_e = 0.5$) can spontaneously emit sound waves, potentially changing the dynamics of the disturbance. The authors connected this phenomenon with the coalescence of mode F

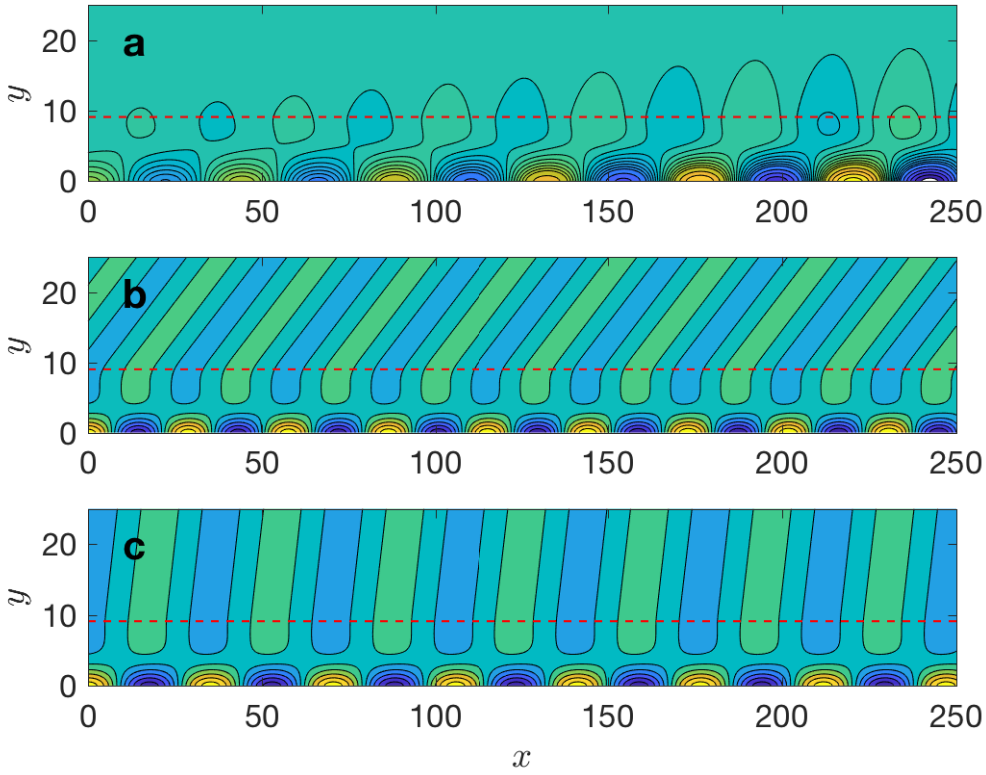


FIGURE 3.11. Case 3, $T_w = 2000$, Air/CP: Local pressure disturbance for mode S at (a) $R = 5000$ and (b) $R = 6550$ and (c) mode S2 at $R = 5890$.

with the acoustic spectrum. It is not clear to what extent the results of Ref. [13] can be extrapolated to understand the present configuration since the spectrum topology is somewhat more complicated than for the lower Mach number cases considered therein.

Further complicating the traditional LST analysis is the fact that mode S2 is unstable and supersonic well before the dominant unstable mode becomes supersonic. Figures 3.12a and 3.12b show the phase speed for mode S and S2 at two frequency parameters, before and after the transition of mode S from subsonic to supersonic. The arrows indicate the direction of increasing Reynolds number. The point along the trajectories where mode S2 appears is indicated by black dots. For $F = 2.73 \times 10^{-5}$,

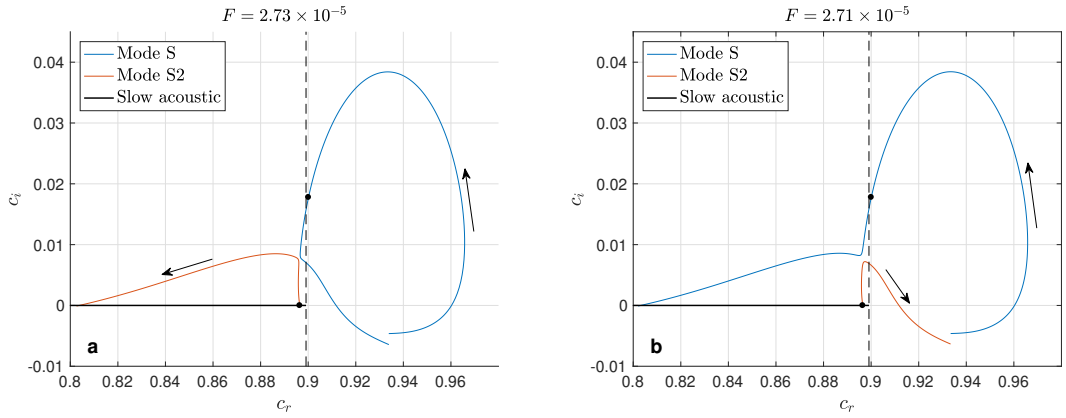


FIGURE 3.12. Case 3, $T_w = 2000$, Air/CP: Trajectory of Modes S and S2 in the complex phase speed plane for two frequencies. Arrows indicate the direction of increasing $R$.

the new mode branches off of the continuous spectrum and becomes substantially unstable before again coalescing with the acoustic branch. Mode S2 is supersonic over the entirety of its life span. Because mode S is at the peak of its potential amplification when the two become synchronized, it is feasible that coupling could result in substantial excitation of mode S2, leading to significant sound radiation earlier than expected. These results suggest that, for high Mach number configurations, caution must be taken in expressing boundary layer disturbances in terms of a single mode, even when the dominant mode is not supersonic.

Finally, a less subtle implication of the supersonic mode onset is that the dominant mode is unstable over a greater distance and thus its potential for overall amplification is increased. Figure 3.13 shows $N$-factors for a range of frequencies for this case with $\beta = 0$. Waves that transition from subsonic (blue) to supersonic (red) undergo greater amplification. The net result of this phenomenon on the full disturbance wavepacket can be understood from Figure 3.14 which shows the $N$-factor as a function of $\omega$ for a range of Reynolds numbers. Upstream (lower $R$), the wavepacket consists of entirely subsonic waves. Moving downstream (higher $R$), the unstable

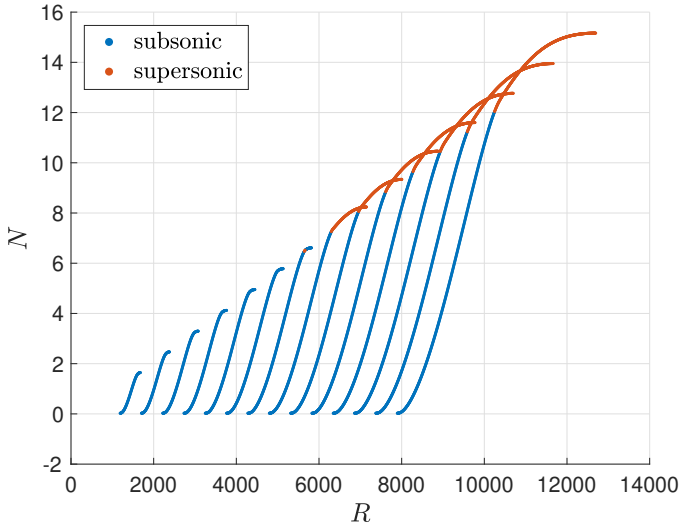


FIGURE 3.13. Case 3, $T_w = 2000$, Air/CP: $N$-factors for a range of frequencies and $\beta = 0$.

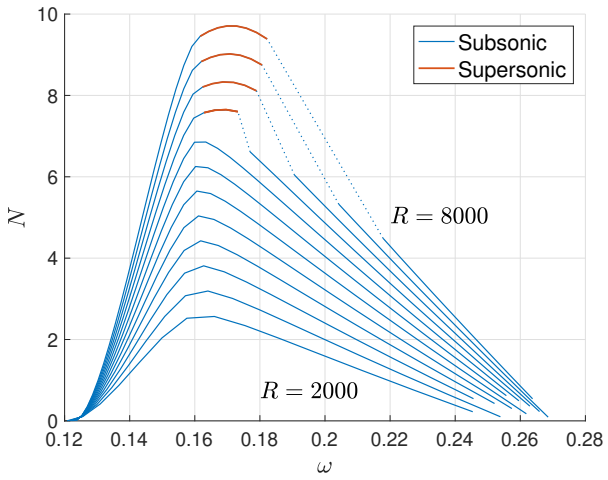


FIGURE 3.14. Case 3, $T_w = 2000$, Air/CP: $N$-factor as a function of frequency $\omega$ for a series of Reynolds numbers increasing from the bottom by 500.

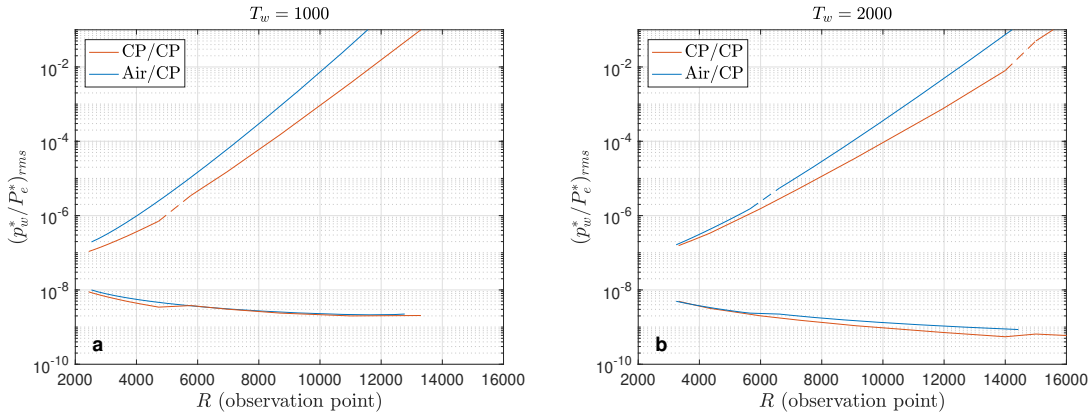


FIGURE 3.15. Case 3: Magnitude of the KF-induced wall pressure perturbation for (a) $T_w = 1000$ and (b) $T_w = 2000$ under both models.

waves become supersonic near the peak in their amplification, resulting in broader spectral amplification.

The dashed lines in Figure 3.14 are a visual aid; The dominant unstable mode (mode S) is not present in this region as a result of its coalescence with the slow acoustic branch of the continuous spectrum. The discontinuity in the second derivative $N_{\omega\omega}$ will result in a discontinuity in the KF-induced wavepacket amplitude, as is evident from formula (3.3.31). Of course, this does not reflect a discontinuity in the physical problem, and is in fact an indication of the shortcomings of a single mode approximation for this case. Nevertheless, for the sake of obtaining order of magnitude estimates of the KF-induced disturbance amplitude, our approximation remains valid.

Figure 3.15a shows the root mean square amplitude $(p_w^*/P_e^*)_{\text{rms}}$ of the KF-induced wall pressure disturbance under both the CP/CP and Air/CP models, computed using formula (3.3.31). The amplitude is shown as a function of the Reynolds number based on the streamwise point of observation. The lower curves correspond to the downstream wave-packet amplitude re-scaled by the factor $e^{N_{max}}$, where $N_{max}$ is the $N$-factor of the dominating frequency at the observation point. This quantity reflects

both receptivity and selective downstream amplification and thus should not be interpreted as the initial amplitude of the wavepacket. Rather, it is meant to give a sense of the extent of the amplification required to raise the disturbance induced by KF to the level of physical significance. This emphasizes that the discrepancy in the downstream disturbance magnitude predicted by the two models is due largely to differences in overall amplification rather than receptivity. A similar comparison of the induced wall pressure disturbance for wall temperature $T_w = 2000$ is provided in Figure 3.15b.

The portions of the curves indicated by dashed lines are not resolved due to the spontaneous increase in $N_{\omega\omega}$ with the onset of supersonic modes. The curve corresponding to Air/CP in Figure 3.15a is solid because the disturbance consists of supersonic waves over the entire range of Reynolds numbers considered.

For both wall temperatures, the downstream magnitude of the KF-induced wavepacket is greater under the Air/CP model. This is not attributed to the receptivity phenomenon as we have already demonstrated that the receptivity is comparable between the two models. The discrepancy is due rather to differences in downstream amplification. The difference is primarily due to the lower mean temperature profiles predicted by the Air model which leads to both further destabilization of subsonic unstable modes as well as earlier onset of supersonic unstable modes.

### 3.4.2 Case 1: $T_e = 278\,\mathrm{K}$, $P_e = 0.0433\,\mathrm{atm}$, $U_e = 3.351\,\mathrm{km/s}$, $M_e = 10$

Case 1 represents a moderate-enthalpy configuration. The flow conditions lead to frozen parameters $\gamma_f = 1.40$ and $Pr_f = 0.715$. The mean temperature and streamwise velocity profiles under each model for wall temperatures $T_w = 1000$ and $T_w = 2000$ are shown in Figure 3.16.

Figure 3.17a provides a comparison of the KF-induced wall pressure disturbance magnitude for Case 1, $T_w = 1000$, under both models. The format is the same as

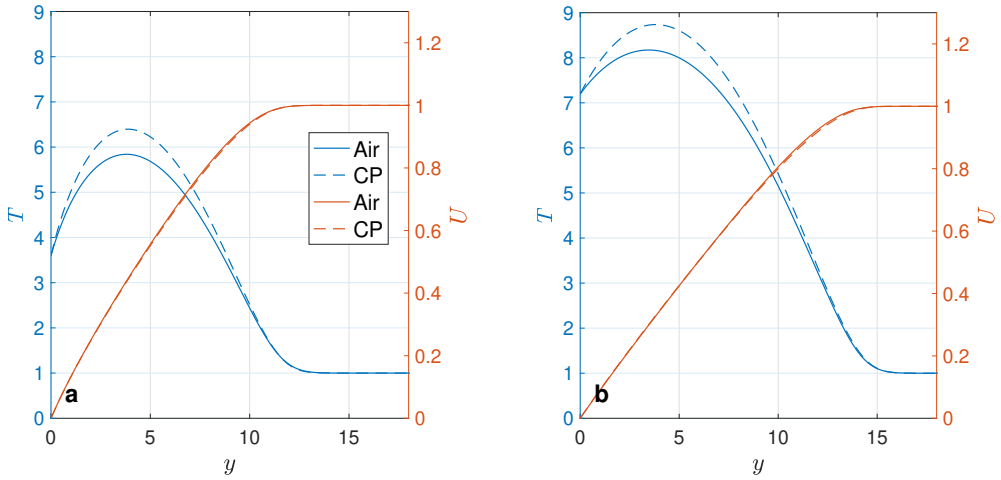


FIGURE 3.16. Case 1: Mean temperature and streamwise velocity profiles for a) $T_w = 1000$ and b) $T_w = 2000$ under the Air and CP models.

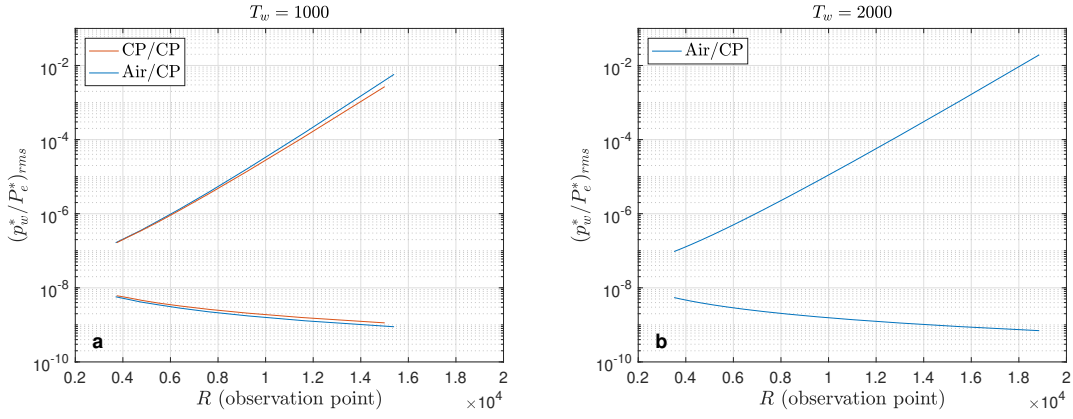


FIGURE 3.17. Case 3: Magnitude of the KF-induced wall pressure perturbation for (a) $T_w = 1000$ and (b) $T_w = 2000$ under both models.

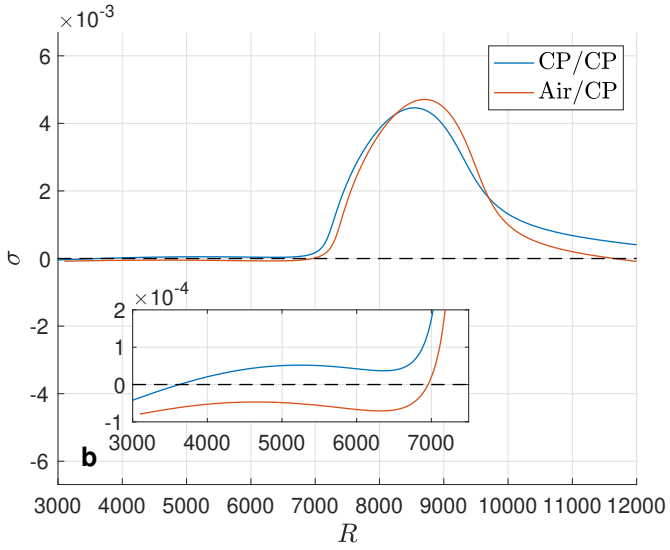


FIGURE 3.18. Comparison of growth rates under the CP/CP and Air/CP models for Case 1, $T_w = 2000$, $F = 1.15 \times 10^{-5}$.

for the corresponding Case 3 comparisons. For this case, no supersonic modes are present under either model for the range of frequencies considered. The slightly higher disturbance magnitudes predicted by the Air/CP model are a result of the associated lower mean temperature profile.

Figure 3.17b shows the KF-induced disturbance magnitude for wall temperature $T_w = 2000$, but only for the Air/CP model. Note that the downstream wavepacket amplitudes are slightly lower as compared to those for $T_w = 1000$ under the same model. This can again be largely attributed to the de-stabilizing effect of lower temperatures on the second Mack mode.

The curve corresponding to the CP/CP model in Figure 3.17b is not shown due to a difficulty in approximating receptivity along the lines of Section 3.3 in this case. In particular, for most of the physically relevant frequencies, a weakly unstable first Mack mode precedes the dominant second Mack mode instability feature. Thus, the neutral point, where the receptivity approximation takes place, is pushed far upstream. This can be seen in Figure 3.18 which shows the growth rate under both the CP/CP model

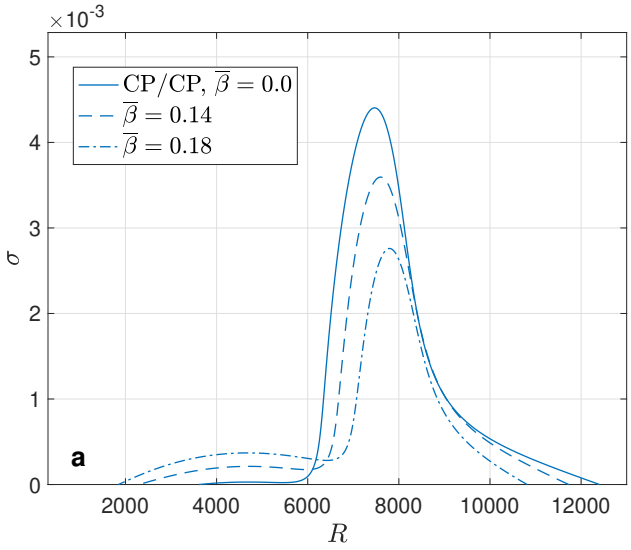


FIGURE 3.19. Growth rate under the CP/CP model for Case 1, $T_w = 2000$, $F = 1.15 \times 10^{-5}$ and $\beta = 0.0, 0.14$ and $0.18$.

and the Air/CP model for $F = 11.5 \times 10^{-6}$ and $\beta = 0$. The receptivity solution was derived assuming an excitation region of width $\epsilon^{1/2}/\sigma_{x_1} = O\left(\epsilon^{1/2}\right)$ about the neutral point, assuming the growth rate gradient $\sigma_{x_1} = O(1)$. However in this case, $\sigma_{x_1} \ll 1$ indicating that the excitation region may be substantially longer. This highlights a major shortcoming of the present approach to solving the receptivity problem. The growth rates predicted by the Air/CP and CP/CP models are quite consistent for this case, yet the model, if applied naively, predicts dramatically different receptivity outcomes, in conflict with physical intuition.

Additionally, note that an increase in the spanwise wavenumber $\beta$ simultaneously stabilizes the second Mack mode instability feature while destabilizing the first Mack mode. This is demonstrated in Figure 3.19 which shows the growth rate under the CP/CP model for $F = 1.60 \times 10^{-5}$ for $\beta = 0.0, 0.14$ and $0.18$. The normalization of $\beta$ is based on $\Delta^*$ at the neutral point. The net amplification still decreases away from $\beta = 0$ and thus the approximation of the Fourier inversion integrals via Laplace's

method (Eqn. (3.3.31)) is still valid. However, since for some frequencies the first mode only becomes unstable for some finite value of $\beta$, the additional amplification associated with this feature is not captured in an approximation that occurs at $\beta = 0$. In Chapter 4, the validity of approximating the integrals in $\omega$ and $\beta$ is explored for this case and a variety of others.

## 3.5 Conclusions

In this chapter we have computed the magnitude of the wavepacket induced by KF in high-enthalpy boundary layers. As a first step towards understanding the role of real gas effects in this phenomenon, we have compared results based on two mean flow models: a five-species model for air and a calorically perfect gas model. In both cases, the CP assumption has been maintained in the stability and receptivity calculations. Real gas effects for the cases considered are primarily manifested through a lower mean temperature profile through the boundary layer.

Our results lead to two primary findings. (1) The receptivity phenomenon is not strongly influenced by real gas effects for the cases considered in this work. This is because the receptivity mechanism is located in the critical layer of the boundary layer. For high Mach number configurations, the critical layer is close to the boundary layer edge where the difference in the mean flow profiles predicted by the CP and Air models are not very different. The shear stress fluctuation in the $x$-momentum equation was shown to be the principal contribution to the excitation of the dominant mode, in agreement with earlier results at lower hypersonic Mach numbers. (2) Real gas effects can have a substantial impact on the spectrum topology. Use of the Air model results in greater destabilization of the second Mack mode and also leads to earlier onset of unstable supersonic Mack modes. Both of these effects result in higher predicted KF-induced disturbance magnitudes.

We have also found that the spectrum topology associated with the onset of su-

personic unstable modes is different in the high Mach number cases considered herein than for the more moderate hypersonic configurations considered elsewhere in the literature. In particular, for all cases considered, the dominant unstable mode is mode S. The transition of this mode from subsonic to supersonic is associated with a discrete spectrum branching, rather than a direct coalescence with the continuous spectrum. In such cases there is an additional discrete mode, not previously identified in the literature, which is unstable and supersonic prior to the dominant mode becoming supersonic. DNS studies are needed to fully appreciate the implications of these results. We note that there may be additional (stable) discrete mode(s) present in a figure like Figure 3.12 that were not explored for the purposes of the present work.

We have also highlighted a limitation of the receptivity solution laid out in Section 3.3. In particular, because the method relies on an approximation at the neutral point, it is highly sensitive to nuanced growth rate behavior in the vicinity of the instability onset. The method fails when a weakly unstable first Mack mode is present due to failure in the assumption that excitation occurs in a narrow neighborhood of the neutral point. In Chapter 4, we develop an alternative approach to solving the receptivity problem which is more broadly applicable.

Finally, the destabilization of the first Mack mode with increasing span-wise wavenumber can have a substantial impact on the total magnitude of the KF-induced disturbance wavepacket. In certain cases, this effect can be missed by an asymptotic approximation of the wavepacket integrals at $\beta = 0$. In such cases, numerical integration may be necessary. This issue is explored for a variety of configurations in Chapter 4.

# Chapter 4

# A Model of Distributed Receptivity to Kinetic Fluctuations

## 4.1 Introduction

The shortcomings of the matched asymptotic (MA) solution to the KF-receptivity problem were highlighted at the end of the previous chapter using the example of Case 1, $T_w = 2000$. Under the CP/CP model, the MA approach failed due to the appearance of a weakly unstable first Mack mode and a breakdown of the assumption that dominant excitation occurs in an $O(\epsilon^{1/2})$ neighborhood of the neutral point.

In this chapter, we pursue a solution to the receptivity problem which is applicable across a broader range of configurations. We are particularly interested in high-hypersonic boundary layers where the dominant unstable mode exhibits long-scale near neutral behavior upstream of the neutral point. It was evident that the results of the MA approach for Case 1, $T_w = 2000$, under the CP/CP model were incorrect because the receptivity solution differed dramatically from that obtained under the Air/CP model, despite only minor differences in the underlying boundary layer. Thus a more successful model should also yield consistent results between configurations for which physics dictates that the receptivity phenomenon should be similar.

The receptivity solution developed in this chapter is similar to that recently employed by Luchini to study low-speed incompressible boundary layers over a swept wing [61]. As in the MA approach, a solution is sought in the form of WKB ansatz under the single-mode approximation. However, in the present work, we derive a differential equation governing the amplitude of the dominant mode which is integrated directly. No assumption is made about the length of the region where effective KF-excitation occurs and no approximation is made to the growth rate near the in-

stability onset. This allows for the excitation region to be examined in detail and provides intuition into the receptivity phenomenon. In certain cases, the solution is seen to be asymptotically equivalent to the the MA solution.

For the solution derived herein, there is an opportunity to approximate Fourier inversion integrals in $\omega$ and $\beta$ using Laplace's method, as was done in Chapter 3. This approximation is generally preferable to numerical integration which represents an appreciable increase in computation and some challenges in implementation. By comparison with direct numerical evaluation, the validity of the approximation is confirmed for a range of configurations. One possible exception exists for cases where a weakly unstable first Mack mode precedes the dominant second Mack mode instability.

The bulk of the work presented in this chapter has been published in [19], however, the presentation has been substantially altered for the coherence of the present manuscript. Briefly, the structure of this chapter is as follows. Section 4.2 contains the formulation and solution of the receptivity problem. Discussion of the solution is provided in §4.3, followed by a validation of the code developed based on the present formulation for a Mach 0.04 and a Mach 6 configuration. In §4.3.3 we revisit Case 1, $T_w = 2000$, considered in Chapter 3, for which the dominant mode growth rates exhibit long-scale near neutral behavior upstream of the lower neutral branch. In §4.3.4 we provide results for a supersonic (Mach 2) boundary layer where the dominant instability waves are oblique. We conclude with a recapitulation of the key results of this chapter and their implications.

## 4.2 Solution to the receptivity problem

As in Chapter 3, we consider the boundary layer over a flat plate in quiet flow conditions. The base flow is steady, two-dimensional and only weakly varying in the stream-wise direction. The governing equations are the linearized, nonparallel bound-

ary layer disturbance equations forced by kinetic fluctuations

$$\begin{gathered} \mathrm{H}^{(np)}(y, \partial_y, x_1, \epsilon\partial_{x_1}, \omega, \beta)\hat{\boldsymbol{F}} = \hat{\boldsymbol{G}}^{(L)}, \\ y = 0 : \hat{F}_i = 0, \ i = 1, 3, 5, 7, \\ y \to \infty : |\hat{F}_i| < \infty, \ i = 1, 3, 5, 7. \end{gathered} \tag{4.2.1}$$

We again adopt a single-mode approximation under the assumption that coupling of the dominant mode with other components of the spectrum is not significant. (A more precise statement about when this assumption is valid is developed in Chapter 5). The eigenvalue of the unstable mode is denoted by $\alpha$. For hypersonic cases this may be either mode F or mode S. The topology is substantially different at lower speeds and the dominant instability is known as the Tollmein-Schlicting mode. For the purposes of the present formulation, the distinction is not of great importance. A multiple scales expansion is introduced through the WKB type ansatz

$$\hat{\boldsymbol{F}} = \left[c(x_1)\boldsymbol{A}^{(0)}(x_1, y) + \epsilon\boldsymbol{A}^{(1)}(x_1, y) + O(\epsilon^2)\right] K(x_1), \tag{4.2.2}$$

$$K(x_1; \omega, \beta) = \exp\left[i\epsilon^{-1}\int_{x_{10}}^{x_1} \alpha(\eta; \omega, \beta)\mathrm{d}\eta\right], \tag{4.2.3}$$

where the zeroth order amplitude vector-function $\boldsymbol{A}^{(0)}(x_1, y)$ in Eqn. (4.2.3) is an eigenfunction of the conventional LST problem

$$\begin{gathered} \mathcal{L}\boldsymbol{A}^{(0)} = 0, \quad \mathcal{L} = \left[\frac{\mathrm{d}}{\mathrm{d}y} - \mathrm{H}_0(\alpha, x_1)\right], \\ y = 0 : A_i^{(0)} = 0, \ i = 1, 3, 5, 7, \\ y \to \infty : |A_i^{(0)}| \to 0, \ i = 1, 3, 5, 7. \end{gathered} \tag{4.2.4}$$

For convenience, the lower integration bound in the definition of the exponential (4.2.3) is taken in this chapter to be the neutral point $x_{10}$ of the unstable mode. We note, however, that the product $c(x_1)K(x_1)$ is independent of this choice, and, thus, so is the final solution.

The coefficients of Eq. (4.2.4) depend on the mean flow profiles and are slow functions of the variable $x_1$, as are the eigenfunction $\boldsymbol{A}^{(0)} = \boldsymbol{A}^{(0)}(x_1, y)$ and the

eigenvalue $\alpha = \alpha(x_1)$. The normalization of $\boldsymbol{A}^{(0)}$ is chosen based on the desired interpretation of the final result. For example, if the eigenfunction is normalized so that the quantity of interest (wall pressure, streamwise velocity perturbation, etc.) is equal to one, the product $\epsilon_L c(x_1)K(x_1)$ corresponds to the physical amplitude of that quantity as a function of the downstream coordinate $x_1$.

Inserting (4.2.3) into the forced disturbance equations and using the homogeneous problem (4.2.4) yields the following linear equation for the amplitude correction term $\boldsymbol{A}^{(1)}$:

$$\mathcal{L}\boldsymbol{A}^{(1)} = -i\frac{\partial \mathrm{H}_0}{\partial \alpha}\left(\frac{\mathrm{d}c}{\mathrm{d}x_1}\boldsymbol{A}^{(0)} + c\frac{\mathrm{d}\boldsymbol{A}^{(0)}}{\mathrm{d}x_1}\right) + c\,\mathrm{H}_3\,\boldsymbol{A}^{(0)} + \epsilon^{-1}\hat{\boldsymbol{G}}^{(L)}K^{-1} + O\left(\epsilon\right). \quad (4.2.5)$$

The components of $\mathrm{H}_3$, which contain terms related to the non-parallel nature of the mean flow, such as $\mathrm{d}U/\mathrm{d}x_1$, are provided in Appendix A.2. The solvability condition requires that the right-hand side of Eq. (4.2.5) be orthogonal to the vector-function $\boldsymbol{B}^{(0)}$, defined as a solution to the adjoint problem

$$\begin{gathered}\mathcal{L}^\dagger \boldsymbol{B}^{(0)} = 0, \quad \mathcal{L}^\dagger = \left[\frac{\mathrm{d}}{\mathrm{d}y} + \mathrm{H}_0^H\right], \\ y = 0 : B_i^{(0)} = 0,\ i = 2,4,6,8, \\ y \to \infty : |B_i^{(0)}| \to 0,\ i = 2,4,6,8.\end{gathered} \quad (4.2.6)$$

The direct and adjoint eigenfunctions satisfy the bi-orthogonality condition

$$\left\langle -i\frac{\partial \mathrm{H}_0}{\partial \alpha}\boldsymbol{A}_\alpha^{(0)}, \boldsymbol{B}_\beta^{(0)}\right\rangle = \Gamma\Delta_{\alpha\beta} \quad (4.2.7)$$

where $\Delta_{\alpha\beta}$ is the Dirac delta if both $\alpha$ and $\beta$ belong to the continuous spectrum, and the Kronecker delta otherwise. The inner product is defined by:

$$\langle \boldsymbol{f}, \boldsymbol{h}\rangle = \int_0^\infty \sum_{i=1}^{8} f_i h_i^* \mathrm{d}y. \quad (4.2.8)$$

where $\cdot^*$ denotes complex conjugation. Applying the solvability condition yields a first order ODE for the amplitude coefficient $c(x_1)$:

$$\frac{\mathrm{d}c}{\mathrm{d}x_1} + M\Gamma^{-1}c = \epsilon^{-1}qK^{-1}, \tag{4.2.9}$$

$$q(x_1;\beta,\omega) = -\Gamma^{-1}\left\langle \hat{\boldsymbol{G}}^{(L)}, \boldsymbol{B}^{(0)} \right\rangle, \quad \Gamma = -i\left\langle \frac{\partial \mathrm{H}_0}{\partial\alpha}\boldsymbol{A}^{(0)}, \boldsymbol{B}^{(0)} \right\rangle, \tag{4.2.10}$$

$$M(x_1;\alpha,\beta,\omega) = \left\langle -i\frac{\partial \mathrm{H}_0}{\partial\alpha}\frac{\mathrm{d}\boldsymbol{A}^{(0)}}{\mathrm{d}x_1} + \mathrm{H}_3\boldsymbol{A}^{(0)}, \boldsymbol{B}^{(0)} \right\rangle. \tag{4.2.11}$$

Note that (4.2.9) is not the same as the amplitude equation (3.3.14) derived in Chapter 3. In that context, the equation modeled the response to a single component of the forcing under the assumption of a width $O\left(\epsilon^{1/2}\right)$ excitation region. In this inner region, the eigenvalue was assumed to evolve linearly and the effect of boundary layer growth did not enter into the lead order approximation. In the present formulation, we make no approximation to the behavior of the eigenvalue. The nonparallel evolution of the boundary layer is accounted for through the coefficient $M$, which depends on $\mathrm{H}_3$ and the streamwise derivative of the slow varying eigenfunction $\boldsymbol{A}^{(0)}$. Assuming the mode has zero amplitude at some location $x_{1u}$ sufficiently far upstream of the neutral point, the solution to (4.2.9) is given by

$$c(x_1) = \epsilon^{-1}\exp\left(-\int^{x_1} M\Gamma^{-1}\mathrm{d}x_1'\right) \times \int_{x_{1u}}^{x_1} q\left(\eta\right) K(\eta)^{-1}\exp\left(\int^{\eta} M\Gamma^{-1}\mathrm{d}x_1'\right)\mathrm{d}\eta. \tag{4.2.12}$$

The product $cK$ can then be expressed concisely as

$$cK = \epsilon^{-1}\int_{x_{1u}}^{x_1} q\left(\eta\right)\frac{K^{(np)}(x_1)}{K^{(np)}(\eta)}\mathrm{d}\eta, \tag{4.2.13}$$

where

$$K^{(np)}(x_1) = \exp\left(\int_{x_{10}}^{x_1}\frac{i\alpha(x_1')}{\epsilon} - M(x_1')\Gamma(x_1)^{-1}\,\mathrm{d}x_1'\right). \tag{4.2.14}$$

From (4.2.14) it is apparent that inclusion of nonparallel effects on the evolution of the wavenumber is akin to adopting the physical-optics level WKB approximation. In the present formulation, we make no assumption about the length of the

excitation region. As will be demonstrated in §4.3, the mode generation region for high-hypersonic cases may be elongated, and, in principle, nonparallel effects could play a role. Computations, however, suggest that for the cases of interest in this work, nonparallel effects on stability are not significant.

Figure 4.1 shows $N$-factor curves for Case 1, $T_w = 2000$ for representative frequency $F = 1.40 \times 10^{-5}$. Results are shown based on the CP/CP and Air/CP models where non-parallel effects are included or not. The values of $N_{\max}$ under each model, indicated by an open circle, do not differ substantially. It is worth pointing out however that the inclusion of non-parallel effects in the Air/CP model results in a long region over which the mode is weakly unstable. This has the effect of pushing the neutral point far upstream, making the MA approach of Chapter 3 inapplicable, and reinforcing the need for a receptivity model which treats the excitation region more flexibly. Results of KF-receptivity calculations and further discussion for this case are provided in Appendix B.

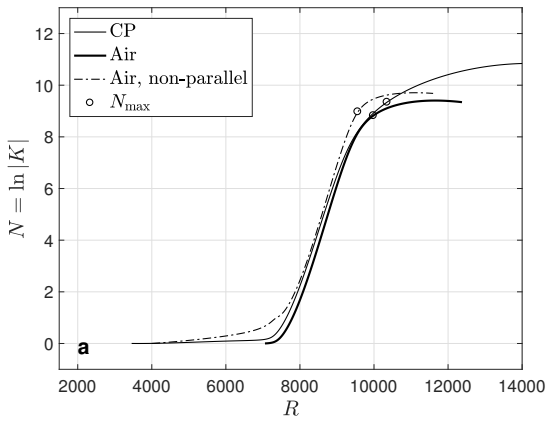


FIGURE 4.1. $N$-factors with $N_{\max}$ indicated by open circles.

For the purposes of this work, we proceed by neglecting nonparallel effects which is achieved formally by setting $M \equiv 0$ in (4.2.12). In this case, the equation governing the amplitude $c$ is simply

$$\frac{\mathrm{d}c}{\mathrm{d}x_1} = \epsilon^{-1} q K^{-1}, \tag{4.2.15}$$

and the product $cK$ is given by

$$c(x_1)K(x_1) = \epsilon^{-1} \int_{x_{1u}}^{x_1} q\,(\eta)\, \frac{K(x_1)}{K(\eta)} \mathrm{d}\eta. \tag{4.2.16}$$

Note that $c$ is a random quantity due to the dependence of $q$ on the stochastic forcing terms $\hat{\boldsymbol{G}}^{(L)}$. To arrive at a physically meaningful result we consider the root-mean-square of the disturbance $\hat{\boldsymbol{F}}$. In this way, we render the details of a single realization of the forcing term irrelevant in favor of its known statistical properties.

The presence of the highly oscillatory term $qK^{-1}$ in (4.2.9) seems to conflict with our assumption that $c = c(x_1)$ is a slowly varying function of the streamwise coordinate. This issue has been addressed to varying degrees in previous works. Zavol'skii and Reutov [110] offer no discussion of the issue but formally arrive at an expression for the mean square disturbance amplitude which is indeed a slow function of the coordinate we call $x_1$. (No slow scale is explicitly introduced in their formalism). Luchini [61] offers an intuitive explanation which resembles the argument for why a stationary phase approximation is valid despite its failure in regions of rapid oscillation. This reasoning is substantiated by an analysis like that used in Chapter 3 to demonstrate the insignificance of wavenumbers outside the resonance interval $O(\epsilon^{1/2}/\Delta^*)$. For the cases of interest here, the range of resonant forcing wavenumbers may be somewhat broader, but the dominant contribution will still be associated with a slow variation of the quantity $qK^{-1}$.

The model adopted here is similar to that of Ref. [61], which is formulated for incompressible flow, and the two formulations are equivalent in the low-speed limit. No scaling is explicitly introduced in Ref. [61], but comparison of the final numerical results leads to the conclusion that, in the low speed limit, our $\epsilon^{-1}\hat{\boldsymbol{G}}^{(L)}$ corresponds to $\mathbf{g}$ in Eq. (22) of that work. Note also that the spectral intensity $q$ in our Eq.

(4.2.9) is equivalent to $F^{(1)}$ in Eq. (1.4) of Ref. [110] (in the low speed limit) with opposite sign.

Using (4.2.16), and the space-time correlations (2.2.10) - (2.2.11), we arrive at an expression for the mean square disturbance associated with the physical parameter of interest

$$\overline{g^2}(x_1) = \frac{\epsilon_L^2}{2\pi^2} \int_0^\infty \int_{-\infty}^\infty \left[ \int_{x_u}^x \left(q^2\right)_{\alpha,\beta,\omega}(\eta) \left| \frac{K(x_1)}{K(\eta)} \right|^2 \mathrm{d}\eta \right] \mathrm{d}\omega \mathrm{d}\beta. \tag{4.2.17}$$

In obtaining (4.2.17) we have used integration by parts to transfer derivatives in $x$ and $y$ from the stochastic forcing terms onto the adjoint eigenfunctions $\boldsymbol{B}^{(0)}$. Details of this calculation are provided in Appendix A.3 and the components of $(q^2)_{\alpha,\beta,\omega}$ are provided in Appendix A.2. The factor $|K(x_1)|$, with the neutral point $x_{10}$ chosen as the lower integration bound, is equivalent to the exponential of the standard $N$-factor defined by

$$N(x_1;\omega,\beta) = \epsilon^{-1} \int_{x_{10}}^{x_1} \sigma(\xi;\omega,\beta)\mathrm{d}\xi, \quad \sigma = -\mathrm{Im}[\alpha]. \tag{4.2.18}$$

Note that expression (4.2.17) accounts for all waves of the dominant mode that are excited by KF, not just the one that is most amplified at each station. Using (4.2.18), we can express (4.2.17) in the equivalent form

$$\overline{g^2}(x_1) = \frac{\epsilon_L^2}{2\pi^2} \int_0^\infty \int_{-\infty}^\infty I(x_1,\omega,\beta) e^{2N(\omega,\beta,x_1)} \mathrm{d}\omega \mathrm{d}\beta, \tag{4.2.19}$$

where

$$I(x_1,\omega,\beta) = \int_{x_{1u}}^{x_1} \left(q^2\right)_{\alpha,\beta,\omega}(\eta) \left|K(\eta,\omega,\beta)\right|^{-2} \mathrm{d}\eta. \tag{4.2.20}$$

For a given observation point $x_1$, the function $N = N(\omega,\beta)$ exhibits a peak in the $(\omega,\beta)$-plane at $(\omega_{\max},\beta_{\max})$, away from which it decays in all directions. This fact suggests approximation of the integrals in (4.2.19) over $\omega$ and $\beta$ by Laplace's method. The result is

$$\overline{g^2}(x_1) = \frac{\epsilon_L^2}{2\pi^2}\left(\frac{2\pi}{\sqrt{2\left|-H(N)(\omega_{\max},\beta_{\max})\right|}} I(x_1,\omega_{\max},\beta_{\max}) e^{2N(\omega_{\max},\beta_{\max})}\right), \quad (4.2.21)$$

where $|-H(N)|$ denotes the determinant of the Hessian matrix for $N = N(\omega,\beta)$. Upon simplification, we obtain the computationally efficient expression

$$\overline{g^2}(x_1) = \frac{\epsilon_L^2}{2\pi\sqrt{N_{\omega\omega}N_{\beta\beta} - N_{\omega\beta}^2}}\left[\int_{x_u}^{x} \left(q^2\right)_{\alpha,\beta,\omega}(\eta)\left|\frac{K(x_1)}{K(\eta)}\right|^2 \mathrm{d}\eta\right]_{\max}, \quad (4.2.22)$$

where $\cdot_{\max}$ indicates evaluation at $(\omega,\beta) = (\omega_{\max},\beta_{\max})$, corresponding to the maximally amplified frequency and span-wise wavenumber at the observation point $x_1$. $N_{\omega\omega}$, $N_{\beta\beta}$, and $N_{\omega\beta}$ represent derivatives of $N$ with respect to the indicated variable at the maximally amplified frequency $\omega_{\max}$ and wave-number $\beta_{\max}$ at the observation point. For high Mach number cases, $\beta_{\max} = 0$ for waves of any frequency, and thus $N_{\omega\beta} = 0$. In cases for which $\beta_{\max} \neq 0$, e.g. the Mach 2 case discussed in §4.3.4, the integrand of (4.2.17) consists of two peaks, one at $(\omega_{\max},\beta_{\max})$ and one at $(\omega_{\max},-\beta_{\max})$. If these two peaks are essentially separate, as is the case for the aforementioned Mach 2 configuration, formula (4.2.22) is a valid approximation if multiplied by 2. If the support of the peaks are substantially overlapping, (4.2.22) will no longer be valid. Of course, (4.2.17) is valid regardless of the structure of its integrand.

From here on out, we will refer to results based on formula (4.2.17) with label 'MMS' and those based on (4.2.22) with label 'MMSA', where the 'A' indicates the additional approximation involved in computing the Fourier integrals via Laplace's method. In Section 4.3, we compare the results obtained based on the MMS and MMSA formulas to explore the validity of asymptotic approximation of the wavepacket integrals. For the cases considered in this work, the discrepancies between the results are not significant, except in certain cases where weakly unstable waves associated with the first mode are present. This point is discussed in detail in §4.3.3.

## 4.3 Results & discussion

In what follows, particular attention will be given to the integral

$$I(x_1;\beta,\omega) = \int_{x_{1u}}^{x_1} S\left(\eta;\beta,\omega\right)\left|K(\eta;\beta,\omega)\right|^{-2}\mathrm{d}\eta, \tag{4.3.1}$$

$$S\left(\eta;\beta,\omega\right) = \left(q^2\right)_{\alpha,\beta,\omega}(\eta), \tag{4.3.2}$$

which appears in the final result (4.2.17) of the previous section. The functions $S$, $|K|^{-2}$, and their product $J = S\,|K|^{-2}$ may be used to examine the features of the excitation region. Note that we consider the integral $I$ without the factor $|K(x_1)|^2$, which is constant for a given observation point $x_1$ chosen downstream of the excitation region. The quotient $|K(x_1)/K(\eta)|$, which may be expressed as

$$\left|\frac{K(x_1)}{K(\eta)}\right| = \exp\left(\epsilon^{-1}\int_{\eta}^{x_1}\sigma(\xi;\omega,\beta)\mathrm{d}\xi\right), \tag{4.3.3}$$

represents the downstream amplification (or decay) at the observation point $x_1$ of disturbances excited at the stream-wise location $\eta$. Expression (4.3.3) makes it clear that the choice of lower bound $x_{10}$ in the definition of $K$ is indeed arbitrary with respect to the final solution. Considered by itself, the function $|K|^{-2}$ *is* a function of the lower integration bound, however, in what follows, our interest is in the qualitative features of $|K|^{-2}$ which are immune to the rescaling that occurs with a change in this lower bound. The factor peaks at the neutral point, where it is unity, and decays away from this peak in both directions.

The discrepancies that arise between the present solution and that of the MA approach amount to differences in the evaluation of the quantity represented by $I$. The solution derived from the MA approach is equivalent to the one developed here if the integrand $J$ is approximated by a Gaussian along the lines of Laplace's method. Thus, although such an approximation is not formally how the MA solution is obtained, it is useful to compare the full integrand of $I$ with the Gaussian

$$\tilde{J} = S\left(x_{10};\alpha,\beta,\omega\right)\exp\left(-\epsilon^{-1}\left(\frac{\mathrm{d}\sigma}{\mathrm{d}x_1}\right)_{x_{10}}(x_1-x_{10})^2\right), \tag{4.3.4}$$

where the receptivity function $S$ is evaluated at the neutral point. Note that this and other quantities of interest will be presented as functions of the local Reynolds number, $R = (2U_e^* x^*/\nu_e^*)^{1/2}$, based on the variable of integration $\eta$ in (4.3.1).

In either approach, the wavepacket integrals in $\omega$ and $\beta$ may be treated either numerically or asymptotically. For each configuration, we explore the validity of formula (4.2.22) (MMSA) in which the integrals over $\omega$ and $\beta$ in (4.2.17) have been approximated asymptotically. It is worth pointing out that discrepancies arising between (4.2.17) and (4.2.22) are muted in their significance upon taking the square root to obtain the root-mean-square disturbance amplitude.

In all cases, integral (4.3.1) was evaluated numerically using a Simpson's rule from the specified observation point $x_1$ to the upstream limit $x_{1u}$ This allowed for the specification of $x_{1u}$ (or $R_u$) as the location where the relative contribution to the integral was less than $10^{-4}$. This was unambiguous because the integrand decays monotonically away from the neutral point in all cases. In evaluating (4.2.17), the integrals over $\omega$ and $\beta$ were computed numerically using a $20 \times 20$ grid in the $(\omega, \beta)$-plane. The integration domain varied widely between cases and even for different observation points within a single configuration. However, because the integrand decays exponentially away from its peak in all directions, it is easy to verify on a case by case basis that the support of the peak has been adequately captured. Due to symmetry across the $\beta$-axis, the integrand only needs to be evaluated over half of the $(\omega, \beta)$ domain.

In what follows, we consider boundary layer configurations at Mach numbers $M = 0.04, 6.0, 10.0$ and 2.0, in that order. The flow parameters for each of these configurations are provided in Table 4.1. The Mach 10 configuration is the same as that referred to as Case 1, $T_w = 2000$ in Chapter 3. For the hypersonic cases, we consider results based on both the calorically perfect (CP) and five-species air (Air) mean flow models. In all cases, the stability computations are performed using a calorically perfect gas stability solver, as explained in Chapter 3.

| | $T_e^*$ (K) | $U_e^*$ (m/s) | $\rho_e^*$ (kg/m$^3$) | $\nu_e^*$ (m/s$^2$) | Pr | $\gamma$ |
|---|---|---|---|---|---|---|
| Mach 0.04 | 300 | 15 | 1.176 | $1.458 \times 10^{-5}$ | 0.70 | 1.40 |
| Mach 6.0 | 300 | $2.084 \times 10^3$ | $4.13 \times 10^{-1}$ | $4.473 \times 10^{-5}$ | 0.72 | 1.40 |
| Mach 10.0 | 278 | $3.351 \times 10^3$ | $5.47 \times 10^{-2}$ | $3.505 \times 10^{-4}$ | 0.715 | 1.40 |
| Mach 2.0 | 62 | $3.16 \times 10^2$ | $8.46 \times 10^{-2}$ | $4.788 \times 10^{-5}$ | 0.72 | 1.40 |

TABLE 4.1. Details of the flow parameters for each case considered in this work.

### 4.3.1 Code Validation: Low-speed Case, $M = 0.04$

As discussed earlier, the receptivity solution derived in this chapter is equivalent to that of Luchini [61] in the low-speed incompressible limit. Thus, as a partial verification of the code developed for this work, we compare our results with those from Ref. [61] for a $M = 0.04$ test case, the details of which are provided in Table 4.1. The dimensionless growth rate $\sigma(R) = -\mathrm{Im}[\alpha(R)]$ for the representative dimensionless frequency parameter $F = 1.5 \times 10^{-5}$ is shown in Figure 4.2a. The *rms* maximal stream-wise velocity fluctuation $u_{\mathrm{rms}}$ of the wave packet is shown as a function of the observation Reynolds number in Figure 4.2b. As anticipated, our result agrees well with that of Luchini. The negligible discrepancy between MMS and MMSA suggests that asymptotic evaluation of the Fourier inversion integrals in $\omega$ and $\beta$ is justified in this case.

Also shown are results reported by Fedorov and Tumin [39] for the same configuration, obtained using the MA approach detailed in Chapter 3. The discrepancy is not significant, which is a result of the consistency of the assumptions underlying the MA approach for this case.

The full dimensionless integrand $J(R; \alpha, \beta_{\max}, \omega_{\max})$ and its individual components, as computed based on the present approach, are shown in Figure 4.3. In this case, effective excitation peaks in the vicinity of the neutral point and decays rapidly outside a neighborhood of that peak, in line with the assumptions underlying the MA formulation. The approximate integrand $\tilde{J}$, also shown in Figure 4.3, is quite consistent with the actual behavior $J$. The close agreement is attributed to the $O(1)$

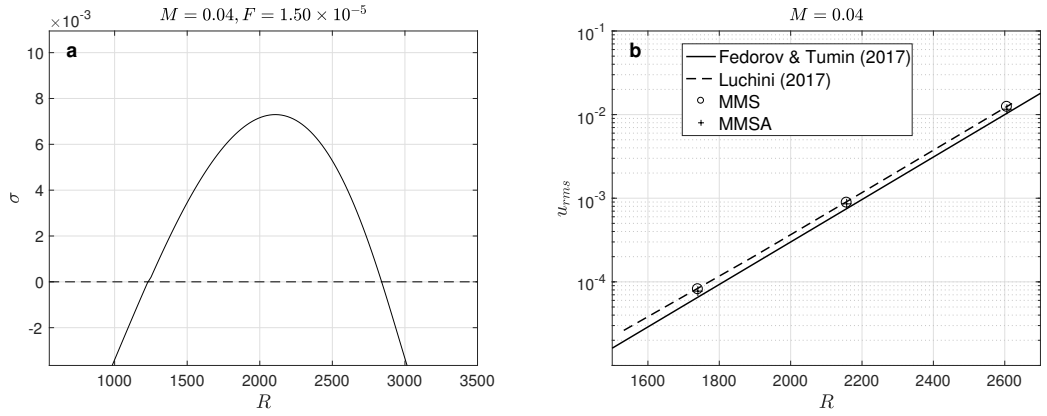


FIGURE 4.2. (a) The growth rate for the Mach 0.04 test case. (b) A comparison of $u_{\mathrm{rms}}$ between the present work and results from Refs. [61, 39] ($M = 0.04$).

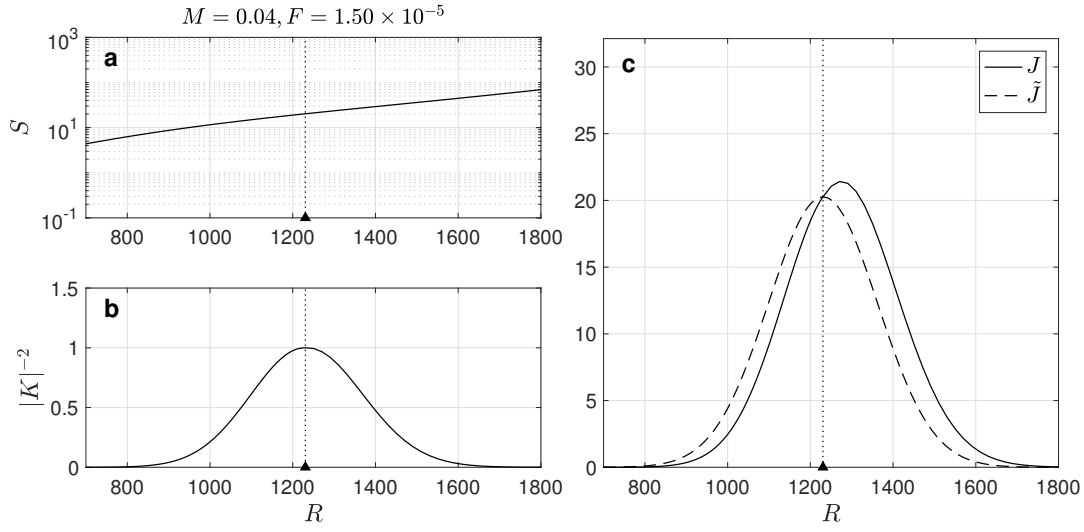


FIGURE 4.3. Components (a) $S$ and (b) $|K|^{-2}$ and (c) comparison of the full integrand $J$ with the Gaussian assumed by the MA approach for the M = 0.04 configuration.

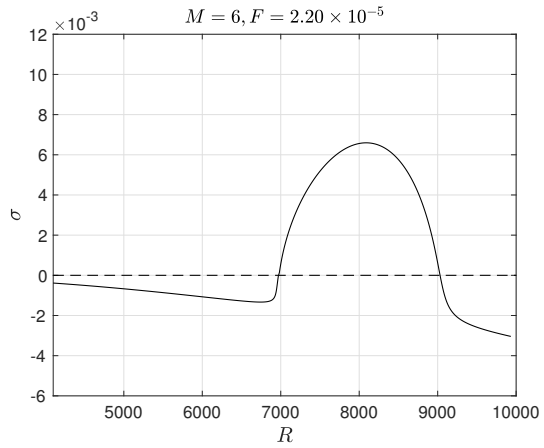


FIGURE 4.4. The growth rate $\sigma = -\mathrm{Im}[\alpha]$ corresponding to frequency parameter $F = 2.20 \times 10^{-5}$, $\beta = 0$, for the Mach 6 test case.

deviation of the growth rate from neutral on either side of the instability onset and the slow variation in the spectral density $S$. This trend persists across all parameters of physical interest for this case.

### 4.3.2 Code Validation: Hypersonic Case, $M = 6.0$

As a hypersonic test case, we consider a Mach 6 flat plate boundary layer previously studied in Ref. [39] using the MA formulation. The flow parameters for this case are provided in Table 4.1. In that work, the mean flow solver was based on a calorically perfect gas model. Here, we consider the same configuration where the mean flow profiles have been computed using the Air model with effective parameters $\gamma_{\text{eff}} = 1.40$ and $Pr_{\text{eff}} = 0.72$.

Figure 4.4 shows the growth rate as a function of $R$ for the representative frequency parameter $F = 2.2 \times 10^{-5}$ and $\beta = 0$. Upstream of the instability onset, the mode is nearly neutral, in contrast to the $M = 0.04$ case, where the mode was heavily damped upstream. This near-neutral evolution is typical for hypersonic configurations and becomes more pronounced with increasing Mach number.

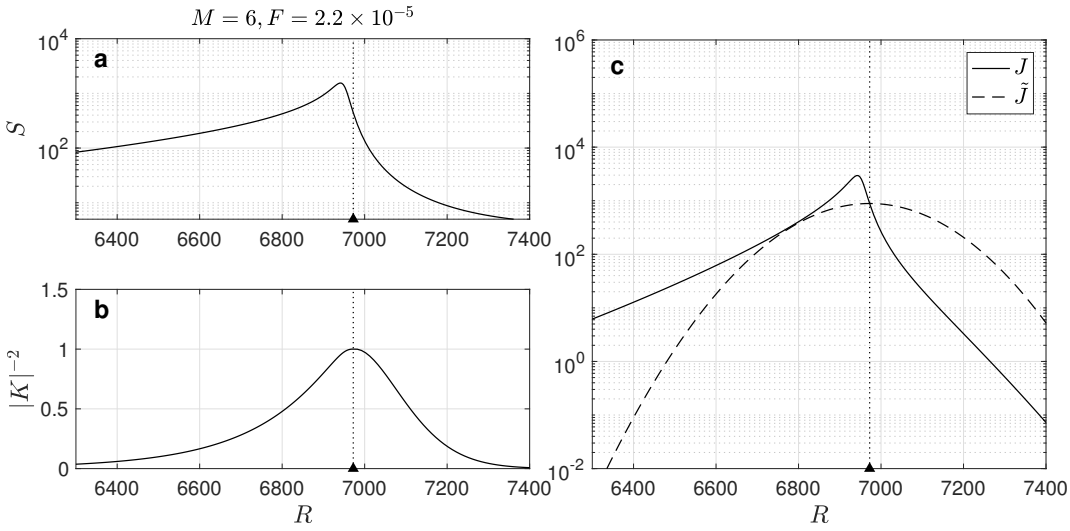


FIGURE 4.5. Components (a) $S$ and (b) $|K|^{-2}$ and (c) comparison of the full integrand $J$ with the Gaussian assumed by the MA approach for the M = 6, Air configuration.

The integrand $J$ and its components are plotted in Figure 4.5 for $F = 2.2 \times 10^{-5}$ and $\beta = 0$. The spectral density $S$, shown in Figure 4.5a, exhibits a strong peak just upstream of the neutral point. This behavior is associated with the proximity of the mode in question to another mode of the discrete spectrum, which suggests an opportunity for coupling. This phenomenon is explored in detail in Chapter 5. The exponential factor $|K|^{-2}$ (Figure 4.5b) exhibits elongated support upstream that is attributed to the near-neutral behavior of the growth rate in that region. Physically, this suggests a lengthening of the region upstream of the neutral point where the excitation of disturbances may be relevant. The effect of this elongation on $J$ is muted due to the decay of $S$ away from the neutral point region.

Figure 4.6 shows the normalized *rms* wall pressure disturbance $(p_w/P_e)_{\text{rms}}$ induced by KF. The good agreement between all three calculations for Air may be attributed to two factors. First, the integrals over $\omega$ and $\beta$ which account for the induced wavepacket are well approximated by the asymptotic formula (4.2.22). Second, despite

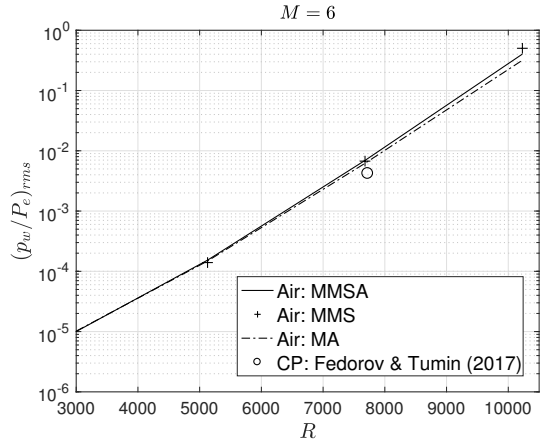


FIGURE 4.6. Downstream magnitude of wall pressure perturbations $(p_w/Pe)_{\text{rms}}$ for the Mach 6 test case.

substantial qualitative and quantitative discrepancies between $J$ and its approximation by a Gaussian, $\tilde{J}$, there is ultimately good agreement in the evaluation of the integral $I$. In this way, the agreement between the direct MMS and the MA solution is somewhat misleading. The MA solution fails to account for the details of the excitation region that are revealed through direct integration of the amplitude equation (4.2.9) in the MMS approach.

Also shown in Figure 4.6 is a value reported in Ref. [20] of $(p_w/P_e)_{\text{rms}}$ for CP mean flow computed using the MA approach. This point is not far from the values corresponding to the Air mean flow model. The small discrepancy is due to lower amplification rates that result primarily from the higher temperature profile predicted by the CP mean flow model. The qualitative features of the excitation region for the CP case are similar to those shown in Figure 4.5.

### 4.3.3 Hypersonic cases, $M = 10$

In this section, we revisit the Mach 10 configuration that was referred to in Chapter 3 as Case 1, $T_w = 2000$. As was done in that chapter, we consider this case under

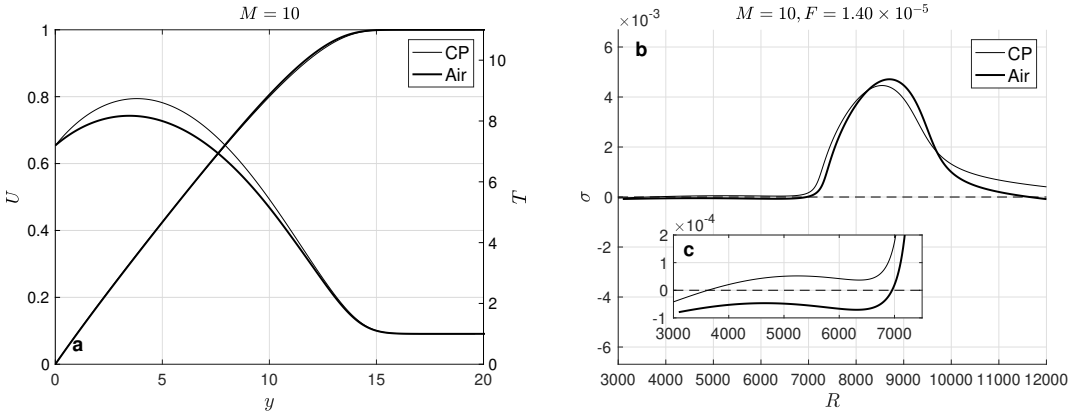


FIGURE 4.7. (a) Mean streamwise velocity and temperature profiles. (b) Dimensionless growth rates. (c) Enhanced view of the near-neutral region.

both the CP/CP and the Air/CP frameworks. The mean streamwise velocity and temperature profiles resulting from each model are reproduced in Figure 4.7a. Growth rates for each model corresponding to the representative frequency parameter $F = 1.40 \times 10^{-5}$ and $\beta = 0$ are shown in Figure 4.7b and 4.7c. (Note that this figure is the same as Figure 3.18 and has been reproduced here for convenience). As demonstrated before, use of the CP mean flow for this configuration results in a weakly unstable growth rate preceding the dominant second mode instability for all physically relevant span-wise wave-number. For this reason, the MA approach is not valid. Use of the Air mean flow does not result in unstable first modes at the maximally amplified wavenumber $\beta = 0$, however, the growth rates do exhibit an extended region of near-neutral behavior.

Figure 4.8 shows $J$ and it's components corresponding to both mean flow models. The neutral points corresponding to CP and Air, $R_0 \approx 3620$ and $R_0 \approx 6955$, respectively, are indicated by vertical dashed lines. The behavior of $S$, Figure 4.8a, is qualitatively and quantitatively consistent between the two models, in line with physical intuition. As for the $M = 6$ case, $S$ peaks near the instability onset and decays exponentially away from this peak under both mean flow models. For Air, the

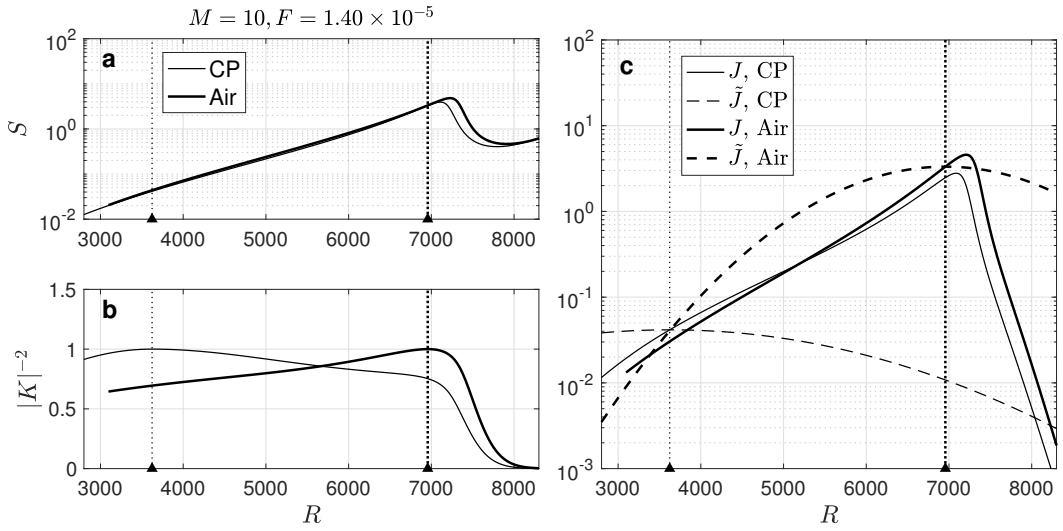


FIGURE 4.8. Components (a) $S$ and (b) $|K|^{-2}$ and (c) comparison of the full integrand $J$ with the Gaussian $\tilde{J}$ assumed by the MA approach for the Mach 10 configuration.

neutral point of the second mode instability is close to this peak. For the CP model, the lower neutral branch, which corresponds to the onset of the first mode instability, is far upstream of the peak in receptivity. In both cases, $K^{-2}$ is $O(1)$ over a long region as a result of the near neutral evolution of the growth rates. This suggests a substantially longer effective excitation region than that observed for the low-speed $M = 0.04$ case considered earlier.

For both mean flow models, the approximation $\tilde{J}$, shown in Figure 4.8c, is largely inconsistent with the behavior of $J$. In the CP case, the approximation fails entirely because the neutral point is far from the locus of dominant excitation. Since the opportunity for subsequent amplification is essentially equal over the entire region where the mode is nearly neutral, the peak in excitation for the unstable mode is dictated by the behavior of $S$. The comparable behavior of $J$ between the Air and CP case for this configuration suggests that the excitation phenomenon is insensitive to the particular location of the neutral point.

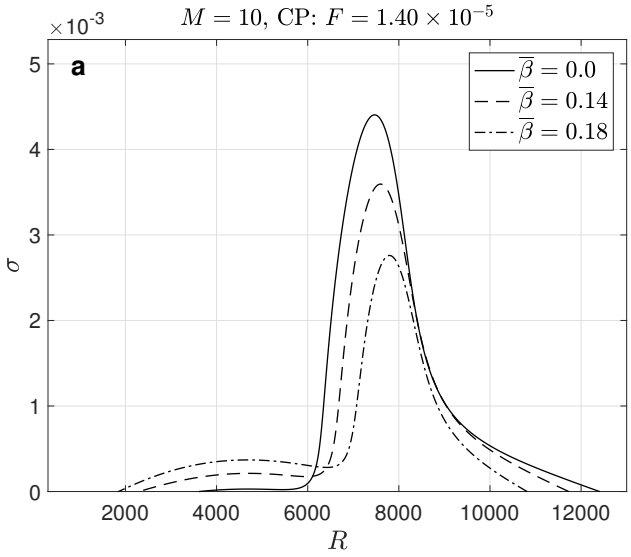


FIGURE 4.9. Growth rates for Case 1, $T_w = 2000$, CP.

Before presenting results for the KF-induced disturbance magnitudes for this case, we illustrate an important feature of the growth rate for nonzero $\beta$. Figure 4.9 shows the growth rate for $F = 1.40 \times 10^{-5}$ and a range of spanwise wavenumbers under the CP model. As $\beta$ increases, the first Mack mode instability feature grows, partially counteracting the decay of the second Mack mode and broadening the spectrum of significantly amplified waves. This helps explain the results of Figures 4.10a and 4.10b which show the *rms* amplitude of the downstream wall pressure disturbance $(p_w/P_e)_{\text{rms}}$ under the Air and CP models, respectively.

For Air, the discrepancy that exists between MMS and MMSA is due to the phenomenon just described. For this case, weakly unstable first Mack modes are present for all frequencies, but only beyond some finite $\beta$. The Laplace approximation adopted in MMSA, which takes place at $\beta = \beta_{\max} = 0$, fails to capture the associated broadening in spectral amplification. Numerical quadrature of course captures this effect, leading to higher overall disturbance magnitudes, particularly downstream. The same reasoning explains the discrepancy in MMS and MMSA under the CP/CP model prior

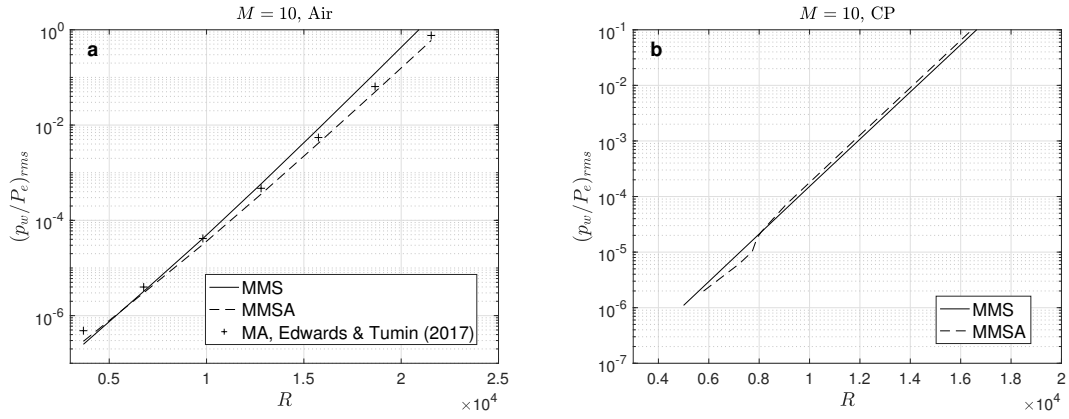


FIGURE 4.10. Downstream magnitude of wall pressure perturbations $(p_w/Pe)_{\text{rms}}$ for the Mach 10 Air configuration.

to $R \approx 8000$ in Figure 4.10b. Under the CP model, only results corresponding to MMS and MMSA are shown since the MA solution is not applicable in this case.

### 4.3.4 Supersonic case, $M = 2$: First mode dominated transition

As a test of the MMS approach for configurations where the maximally amplified modes are three-dimensional, we consider a Mach 2 configuration under the CP mean flow model. For this supersonic case, the dominant instability is the first Mack mode, and the most unstable waves have non-zero span-wise wavenumber $\beta$. Figure 4.11 shows the amplification $|K|^2(R, F, \bar{\beta})$ of the unstable mode in the $(F, \bar{\beta})$-plane for the observation Reynolds number $R = 3000$. Here $\bar{\beta}$ is the span-wise wavenumber non-dimensionalized by the boundary layer length scale at the neutral point $x_0$. The maximally amplified mode at the observation Reynolds number $R = 3000$ corresponds to $F = 1.10 \times 10^{-5}$ and $\bar{\beta} = 0.055$. The components of the spectral excitation integral $I$ are shown for these parameters in Figure 4.12. The qualitative behavior is largely similar to what was observed in the $M = 0.04$ case considered earlier.

Notably, at $R \approx 440$ there is a sharp peak in the receptivity function $S$. This peak is due to the proximity of the unstable mode to an additional mode of the discrete

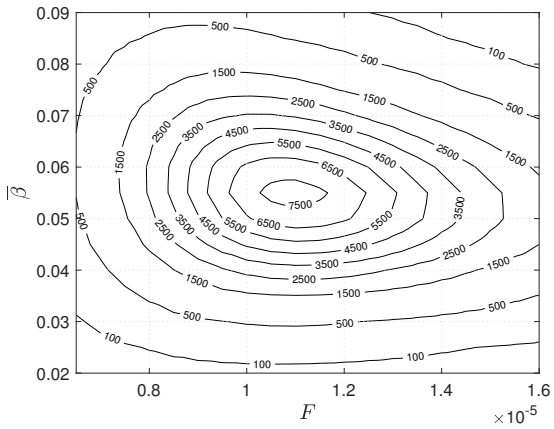


FIGURE 4.11. Amplification spectrum $|K|^2(R_{\text{obs}}, F, \bar{\beta})$ for the unstable mode at observation Reynolds number $R = 3000$.

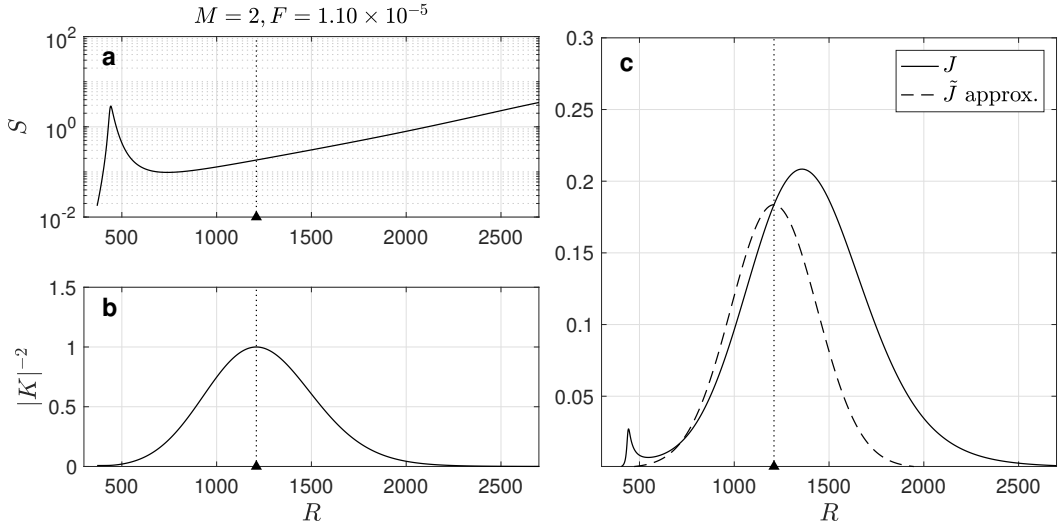


FIGURE 4.12. Components (a) $S$ and (b) $|K|^{-2}$ and (c) comparison of the full integrand $J$ with the Gaussian assumed by the MA approach for the Mach 2 case.

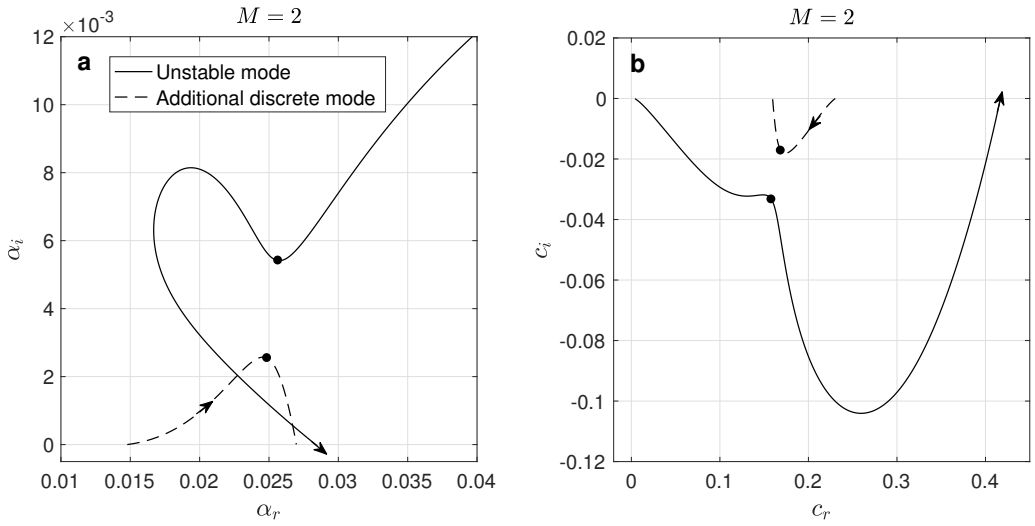


FIGURE 4.13. The trajectory of two discrete modes in (a) the $\alpha$-plane and (b) the complex phase speed plane for $F = 0.85 \times 10^{-5}$ and $\bar{\beta} = 0.055$.

spectrum in this vicinity. The trajectory of both of these modes in the $\alpha$-plane as the Reynolds number is increased is shown in Figure 4.13a for $F = 0.85 \times 10^{-5}$, $\bar{\beta} = 0.055$. The arrows indicate the direction of increasing Reynolds number. Note that the entire life-span of the mode indicated by the dashed line is shown. This mode initially appears when it branches off of the continuous spectrum and then disappears shortly after when it again coalesces with the acoustic branch. The point where the two modes are closest corresponds to $R \approx 499$ and is indicated by a dot along each trajectory. At this location, a sharp, nearly singular peak is observed in the function $S$ for $F = 0.850 \times 10^{-5}$, similar to the one seen in Figure 4.12 at $R \approx 440$ for $F = 1.10 \times 10^{-5}$. This is due to the fact that $|\Gamma|^2$, which appears in the numerator of $S$, tends towards zero as the eigenvalues approach synchronization. This phenomenon and the validity of the current approximation near the coalescence of two discrete modes is explored in detail in Chapter 5.

The phase speed trajectory corresponding to $F = 0.850 \times 10^{-5}$ for the dominant unstable mode and the new mode are shown in Figure 4.13b. Interestingly, the

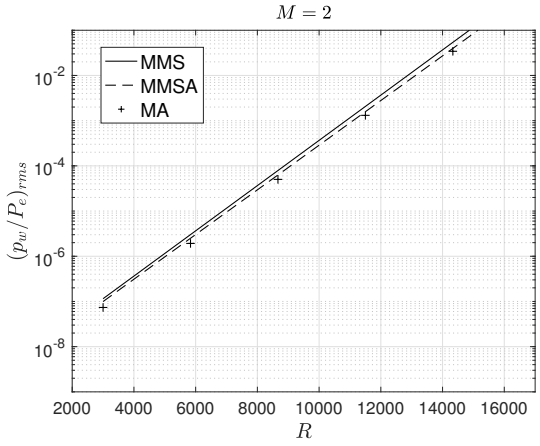


FIGURE 4.14. The downstream magnitude of wall pressure perturbations $(p_w/Pe)_{\text{rms}}$ for the Mach 2 configuration.

spectrum topology observed in this case bears a strong resemblance to that of Case 3, the $M = 10$ configuration considered in Chapter 3, near the transition of the dominant mode from subsonic to supersonic. An important difference, however, is that the latter phenomenon occurs while the mode is unstable, whereas the present behavior occurs while the mode is highly stable. As a result, the peak in $S$ represents a negligible contribution to the overall integral $I$, as is evident in Figure 4.12c. For the purposes of the present work, we make no effort to address this singular behavior or the potential for mode coupling effects. Such an approach may not be acceptable across all similar configurations.

As was the case for the Mach 0.04 case, the present MMS approach and the MA approach yield results that are relatively consistent both qualitatively and quantitatively. The magnitude of wall pressure disturbances $(p_w/P_e)_{\text{rms}}$ induced by kinetic fluctuations is shown in Figure 4.14. Computations based on all three approximations agree reasonably well. Again the asymptotic evaluation of the wave packet integrals in accordance with the MMSA formula (4.2.22) yields results consistent with direct numerical integration (4.2.17). However, as mentioned previously, for cases of this

kind where $\beta_{\max} \neq 0$, an exploration of the $(\omega, \beta)$-plane is necessary anyway, making the computational advantage of asymptotic evaluation less significant.

## 4.4 Conclusions

Receptivity of flat plate boundary layers to distributed forcing by kinetic fluctuations has been studied using a method of multiple scales (MMS) approach. Within the context of this approach, we have explored the validity of approximating the Fourier inversion integrals in $\omega$ and $\beta$ via Laplace's method (MMSA). Results have been presented for a range of configurations, from low speed to hypersonic.

The present MMS/MMSA approach may be compared to a matched asymptotic (MA) approach (all of which are based on a multiple scales formulation). The essential difference between the two amounts to the treatment of the excitation region. In the direct MMS approach adopted here, the ODE governing mode excitation is integrated numerically, whereas the MA approach relies on an asymptotic approximation in a neighborhood of the neutral point, assuming the excitation region is narrow.

For hypersonic configurations, our results suggest the following about the initial excitation phenomenon. (1) Excitation over the entire region where the mode is nearly neutral is essentially equally effective in terms of the potential for subsequent downstream amplification. The particular location of the neutral point is not significant. This leads to a failure of the MA approach outlined in Chapter 3 in certain cases. (2) The spectral density $S$ representing receptivity to KF exhibits a strong peak near the instability onset. This peak is associated with a degree of synchronization between the unstable mode and another mode of the discrete spectrum, indicating the potential for coupling. Properly accounting for this phenomenon is the subject of Chapter 5.

We have also observed a new feature of the stability spectrum topology for a supersonic ($M = 2$) boundary layer. For the Mach 2 case considered herein, the

dominant mode is nearly synchronized with another previously unidentified mode of the discrete spectrum, resulting in a nearly-singular peak in the spectral density $S$. The discrete spectrum branching in this case closely resembles the topology associated with the onset of supersonic unstable modes for hypersonic configurations. Since the branching in the $M = 2$ case occurs while the dominant mode is highly stable, the phenomenon is unlikely to play an important role in the excitation phenomenon.

Finally, the results presented herein suggest that asymptotic evaluation of the Fourier inversion integrals in $\omega$ and $\beta$ via formula (4.2.22) is justified across a broad range of configurations. One possible exception has been identified. For hypersonic cases where unstable first modes are present only outside a neighborhood of $\beta = 0$ where the approximation occurs, formula (4.2.22) may result in an underestimation of KF-induced disturbances due to an underestimation of the range of $\beta$ contributing to the disturbance wave packet.

# Chapter 5

# Receptivity Near the Discrete Mode Branch Point

## 5.1 Introduction

In Chapters 3 and 4 we adopted a single mode approximation in which the KF-induced disturbance was expressed solely in terms of the dominant unstable mode of the discrete spectrum. This approach is justified for a broad range of cases ranging from subsonic to moderate hypersonic. For many hypersonic configurations, however, the picture is complicated by a richer spectrum topology. In Chapter 3, for example, the onset of supersonic unstable modes was linked to a discrete spectrum branching. This phenomenon is not directly connected to initial KF-receptivity because it occurs downstream of the excitation region. Nevertheless, in such cases a single mode approximation in the traditional LST framework may not fully capture the downstream disturbance evolution. The proximity of two discrete modes also posed a difficulty in the analysis of the Mach 2 configuration considered in Chapter 4. This phenomenon was not a significant obstacle in computing KF-receptivity because the synchronization occurred long before the dominant instability onset. In contrast, the synchronization of modes S and F that occurs in the vicinity of the lower neutral point for many hypersonic configurations is highly relevant to questions of receptivity. This is because the synchronization region in this case directly coincides with the region of efficient mode excitation. The synchronization of modes S and F has been studied previously to explain how a stable mode excited near the leading edge can excite an unstable mode downstream prior to its amplification [34]. The phenomenon has also been explored in the context of receptivity to disturbances located on the wall [35].

As explained previously, any discrete spectrum branching may be associated with

a complex Reynolds number $R_{\rm br}$ corresponding to exact coalescence of the modes in question. In principle, the value of $R_{\rm br}$ associated with the initial coalescence of modes S and F may have large imaginary part, even for high Mach number configurations. In this case, synchronization is not strong for the real values of $R$ which are of interest physically and a single-mode approximation is valid. On the other hand, when $R_{\rm br}$ is close to the real axis, the opportunity for mode coupling is strong and an approximation which accounts for more than one component of the spectrum may be necessary. It should be emphasized that, although the efforts of this chapter are oriented towards the KF-receptivity problem, the difficulty to be overcome is essentially fundamental to the stability operator and would arise in the presence of a more general distributed forcing.

In this chapter, we seek to develop a solution to the KF-receptivity problem in the vicinity of the discrete mode branch point. The strategy is as follows. In the vicinity of the discrete mode coalescence, we show that the equations governing the mode amplitudes can be reduced to an inhomogeneous Airy equation which can formally be solved analytically. This solution, which completely accounts for the initial excitation of the disturbance by KF, may then be asymptotically matched to an outer solution capturing the downstream amplification of the unstable mode. In this way, the full evolution of the disturbance induced by KF is accounted for.

We begin by demonstrating the difficulty presented by the coalescence of modes S and F through a test case relevant for hypersonic flight: a 5.5° half-angle wedge at Mach 7. We then develop a solution to the receptivity problem in the case where the discrete mode branch point lies on or near the real axis. Finally, we present results and provide some discussion of directions for future work.

## 5.2 Test case: $5.5^\circ$ Wedge, Mach 7

To illustrate the difficulty, we consider the boundary layer over a wedge with $5.5^\circ$ half-angle at Mach 7. The free-stream parameters are based on flight at altitude 20 km. We consider two cases which differ only in the assumed wall temperature $T_w$. In Case A, we take $T_w = 800$, and in Case B, $T_w = 2000$ K. This corresponds to $T_w/T_{ad} = 0.40$ and $T_w/T_{ad} = 0.99$, respectively, where $T_{ad}$ is the adiabatic wall temperature. In both cases we assume a perfect gas with $\gamma = 1.40$ and $\mathrm{Pr} = 0.72$.

In practice, we study this wedge configuration by considering an equivalent flat plate boundary layer. This is done by taking the 'free stream' flow parameters for the flat plate to be those of the flow at the edge of the boundary layer developing on the wedge, behind the shock wave attached to the leading edge. This leads to consideration of a $M = 6$ flat plate boundary layer with edge parameters $T_e^* = 283$ K, $U_e^* = 2.02$ km/s, and $\nu_e^* = \mu_e^*/\rho_e^* = 1.09 \times 10^{-4}$ m$^2$/s.

The downstream evolution of the eigenvalues for Modes S and F are shown in Figure 5.1a-d for $T_w = 800$ and $T_w = 2000$, respectively. The trajectories were computed by solving the LST eigenvalue problem 2.3.15 under the CP/CP model described in Chapter 3. All plots in Figure 5.1 correspond to frequency parameter $F = 2.5 \times 10^{-5}$ and spanwise wavenumber $\beta = 0$. The eigenvalue trajectories are qualitatively similar between the two cases. In both cases, the unstable mode corresponds to Mode S while Mode F is highly stable downstream of the instability onset.

The growth rates for each case are plotted in Figure 5.1e and the corresponding upstream and downstream branch points $R_{\mathrm{br}}$ are shown in Figure 5.1f. For Case A, the imaginary parts of $R_{\mathrm{br}}$ are, respectively, $\mathrm{Im}[R_{\mathrm{br}}] \approx -2$ and $\mathrm{Im}[R_{\mathrm{br}}] \approx 37$. For Case B, they are $\mathrm{Im}[R_{\mathrm{br}}] \approx -100$ and $\mathrm{Im}[R_{\mathrm{br}}] \approx -351$. The eigenvalue branching topology is determined by whether the branch points are bypassed from above or below. In both Case A and Case B, the upstream branch point is bypassed from above, since, in both cases, $\mathrm{Im}[R_{\mathrm{br}}] < 0$. Accordingly, Mode S is unstable in both

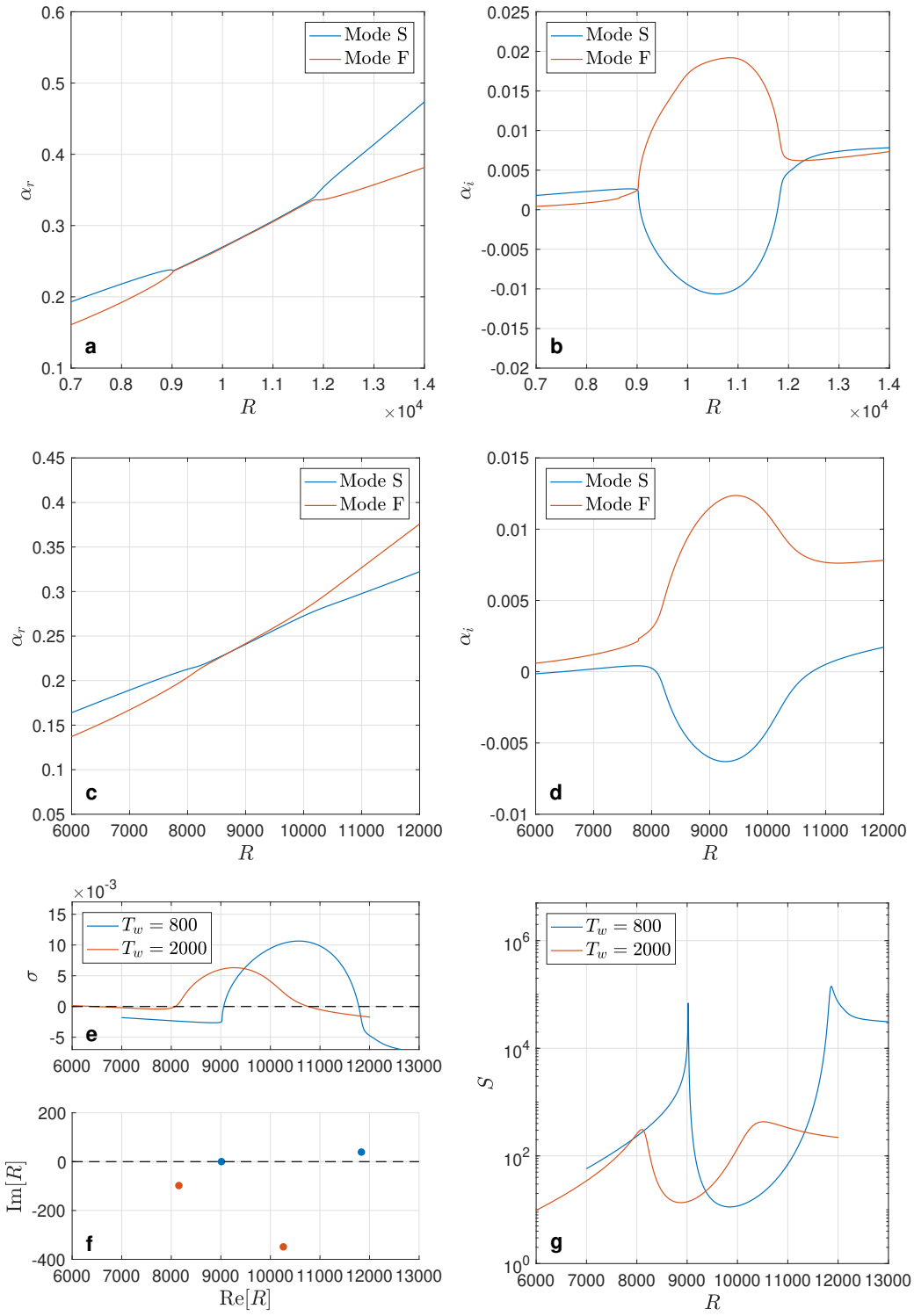


FIGURE 5.1. A comparison of Case A and Case B: (a,b) Discrete mode evolution for Case A. (c,d) Discrete mode evolution for Case B. (e) Growth rates. (f) Upper and lower branch point Reynolds numbers. (g) Receptivity functions $S$.

cases. As the branch point crosses the imaginary axis, which mode is unstable changes spontaneously. Downstream, the branch points are bypassed from above and below, respectively. This leads to branching topology that is different between the two cases, as is evident in comparing the downstream behavior of $\Re[\alpha] = \alpha_r$.

The proximity of the branch point to the real axis has a strong influence on the receptivity function $S$ (in the language of Chapter 4). Plots for each case are shown in Figure 5.1g. The degree to which $S$ is peaked correlates with the proximity of $\mathrm{Im}[R_{\mathrm{br}}]$ to zero. For Case A, the upstream branch point lies essentially on the real axis resulting in nearly singular behavior in the receptivity function. The non-parallel correction to the eigenvalue exhibits similar behavior. Figure 5.2 shows the growth rate for Case A, $F = 2.5 \times 10^{-5}$ along with the non-parallel correction in the vicinity of the discrete mode synchronization.

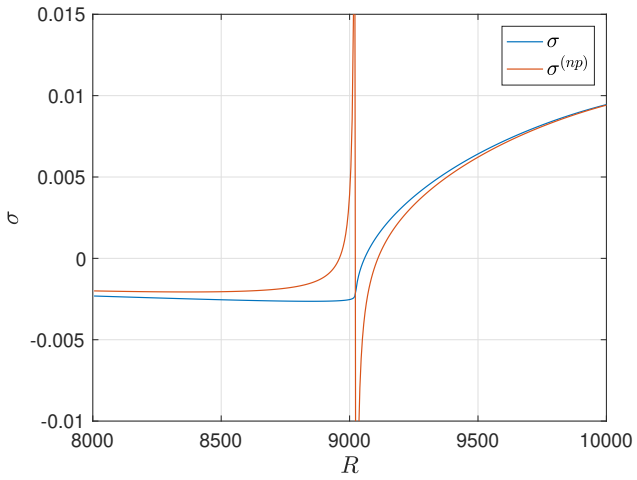


FIGURE 5.2. Growth rate for Case A and the non-parallel correction.

Since the downstream branch point occurs after the opportunity for exponential growth has passed, it is not relevant to questions about physical disturbance growth. From here on out, $R_{\mathrm{br}}$ will refer to the upstream branch point. Figure 5.3 shows $R_{\mathrm{br}}$ for Case A and B as a function of the frequency parameter $F$. The range of physically

relevant frequencies roughly corresponds to the range presented in the figure. The spanwise wavenumber is $\beta = \beta_{\max} = 0$. For Case A, the branch point is very close to the real axis. This is particularly true for lower frequencies which have higher amplification rates and are more likely to contribute to transition onset. In Case B, the branch point is farther from the real axis for all $F$.

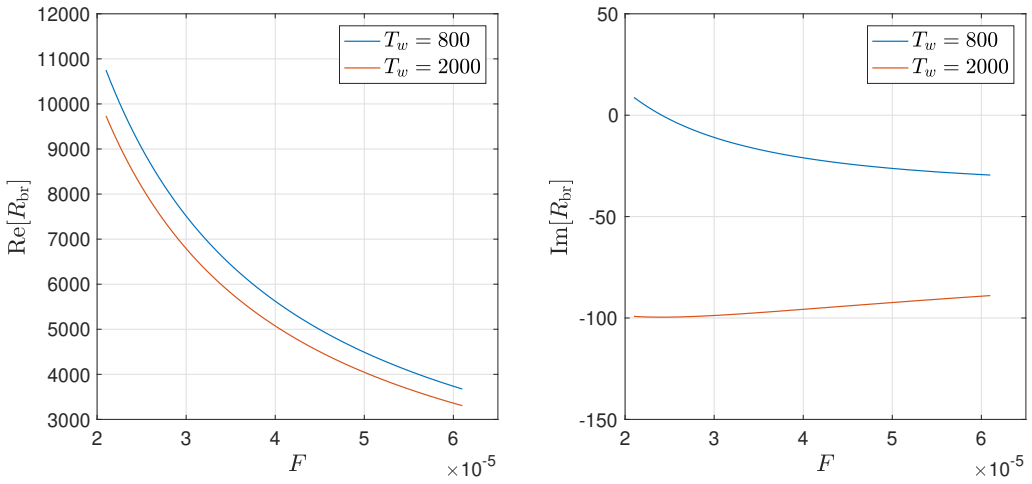


FIGURE 5.3. Position of the upstream discrete mode branch point as a function of frequency parameter $F$ for Case A and B.

## 5.3 The two-mode approximation

In light of the coalescence of modes S and F near the instability onset, we are motivated to consider a two-mode approximation. From here on out we will refer to the two discrete modes in question as Mode 1 and Mode 2 (not to be confused with the first and second Mack modes) with eigenvalues denoted by $\alpha_{1,2}$. As before, the governing equations are the linearized, nonparallel boundary layer disturbance equations with forcing due to kinetic fluctuations

$$\begin{gathered}\mathrm{H}^{(np)}(y,\partial_y,x_1,\epsilon\partial_{x_1},\omega,\beta)\hat{\boldsymbol{F}}=\hat{\boldsymbol{G}}^{(L)},\\ y=0:\hat{F}_k=0,\ k=1,3,5,7,\\ y\to\infty:|\hat{F}_k|<\infty,\ k=1,3,5,7.\end{gathered}\tag{5.3.1}$$

The solution ansatz is the two-mode analog to the single-mode approximation

$$\hat{\boldsymbol{F}}=\boldsymbol{F}_1(x_1,y)K_1(x_1)+\boldsymbol{F}_2(x_1,y)K_2(x_1),\tag{5.3.2}$$

$$K_j=\exp\left(i\epsilon^{-1}\int^{x_1}\alpha_j(x_1')\mathrm{d}x_1'\right).\tag{5.3.3}$$

Inserting (5.3.2) into the forced disturbance equations yields

$$\begin{aligned}&\mathcal{L}_{01}\boldsymbol{F}_1K_1+\mathcal{L}_{02}\boldsymbol{F}_2K_2=\\ &\qquad\epsilon\left(-i\frac{\partial\mathrm{H}_{01}}{\partial\alpha_1}\frac{\partial\boldsymbol{F}_1}{\partial x_1}+\mathrm{H}_3\boldsymbol{F}_1\right)K_1+\epsilon\left(-i\frac{\partial\mathrm{H}_{02}}{\partial\alpha_2}\frac{\partial\boldsymbol{F}_2}{\partial x_1}+\mathrm{H}_3\boldsymbol{F}_2\right)K_2+\hat{\boldsymbol{G}}^{(L)},\end{aligned}\tag{5.3.4}$$

where

$$\mathcal{L}_{0j}=\frac{\partial}{\partial y}-\mathrm{H}_0(x_1,\alpha_j).\tag{5.3.5}$$

The amplitude vector functions $\boldsymbol{F}_j$ are decomposed as

$$\boldsymbol{F}_j=c_j(x_1)\boldsymbol{A}_j(x_1,y),\tag{5.3.6}$$

where $c_j$ is an amplitude function to be determined and $\boldsymbol{A}_j=\boldsymbol{A}_j(y;x_1,\omega,\beta)$ is a solution to the homogeneous eigenvalue problem

$$\begin{gathered}\mathcal{L}_{0j}\boldsymbol{A}_j=0,\\ y=0:A_{ji}=0,\ i=1,3,5,7,\\ y\to\infty:|A_{ji}|\to0,\ i=1,3,5,7.\end{gathered}\tag{5.3.7}$$

The normalization of eigenfunction $\boldsymbol{A}_j$, which is not determined by (5.3.7), will ultimately be chosen based on the desired physical interpretation of the receptivity

solution. For now, it is left unspecified. Since the shape functions $\boldsymbol{A}_j$ are eigenfunctions of the LST eigenvalue problem, the left-hand side of (5.3.4) is identically zero. Using (5.3.6), the equation becomes

$$\left(-i\frac{\partial \mathrm{H}_{01}}{\partial \alpha_1}\left(\frac{\partial c_1}{\partial x_1}\boldsymbol{A}_1 + c_1\frac{\partial \boldsymbol{A}_1}{\partial x_1}\right) + c_1\mathrm{H}_3\boldsymbol{A}_1\right)K_1 + \left(-i\frac{\partial \mathrm{H}_{02}}{\partial \alpha_2}\left(\frac{\partial c_2}{\partial x_1}\boldsymbol{A}_2 + c_2\frac{\partial \boldsymbol{A}_2}{\partial x_1}\right) + c_2\mathrm{H}_3\boldsymbol{A}_2\right)K_2 + \epsilon^{-1}\hat{\boldsymbol{G}}^{(L)} = 0. \quad (5.3.8)$$

Taking the inner product with the adjoint eigenfunction $\boldsymbol{B}_j$, a solution to the adjoint problem

$$\begin{gathered}\mathcal{L}_{0j}^{\dagger}\boldsymbol{B}_j = 0, \quad \mathcal{L}_{0j}^{\dagger} = \frac{\partial}{\partial y} + \mathrm{H}_0^H(x_1, \alpha_j). \\ y = 0 : B_{ji} = 0,\ i = 2, 4, 6, 8, \\ y \to \infty : |B_{ji}| \to 0,\ i = 2, 4, 6, 8,\end{gathered} \quad (5.3.9)$$

and accounting for the biorthogonality condition

$$\left\langle -i\frac{\partial \mathrm{H}_{0i}}{\partial \alpha_i}\boldsymbol{A}_i, \boldsymbol{B}_j \right\rangle = \delta_{ij}\Gamma_{ij}, \quad (5.3.10)$$

yields a system of ODEs governing the mode amplitudes $c_1$ and $c_2$

$$\frac{\mathrm{d}c_k}{\mathrm{d}x_1} + \sum_{j=1,2}\left[\frac{M_{jk}}{\Gamma_{kk}}c_jK_j + \epsilon^{-1}\delta_{kj}\frac{\left\langle \hat{\boldsymbol{G}}^{(L)}, \boldsymbol{B}_k \right\rangle}{\Gamma_{kk}}\right]K_k^{-1} = 0, \quad k = 1, 2, \quad (5.3.11)$$

where $\delta_{kj}$ is the Kronecker delta and

$$\Gamma_{kk} = \left\langle -i\frac{\partial \mathrm{H}_{0b}}{\partial \alpha}\boldsymbol{A}_k, \boldsymbol{B}_k \right\rangle, \quad M_{jk} = \left\langle -i\frac{\partial \mathrm{H}_{0b}}{\partial \alpha}\frac{\mathrm{d}\boldsymbol{A}_j}{\mathrm{d}x_1} + \mathrm{H}_3\boldsymbol{A}_j, \boldsymbol{B}_k \right\rangle. \quad (5.3.12)$$

Equation (5.3.11) is the two-mode analog to the single-mode amplitude equation (4.2.9) obtained in Chapter 4. The effect of the downstream boundary layer growth on the evolution of individual modes is associated with coefficients $M_{jk}$, $j = k$. The off-diagonal elements $M_{jk}$, $j \neq k$ lead to the coupling between waves of Mode 1 and

Mode 2. This coupling is due to the inclusion of non-parallel flow effects which may be viewed as a perturbation of the parallel flow operator.

In Chapter 4, under the single mode approximation, the ODE governing the discrete mode amplitude admitted an explicit solution. Equation (5.3.11) has no apparent analytical solution. For some types of forcing, the receptivity problem could in principle be solved by numerical integration of an equation like (5.3.11). Of course, in the present work, numerical integration is not straightforward since the forcing is known only in terms of its statistical properties. Luckily, by approximating the equations in a small neighborhood of the discrete mode branch point, we can reduce (5.3.11) to an inhomogeneous Airy equation for which an explicit analytical solution exists. By matching the solution in the (inner) branch point region to an outer solution, we obtain a full approximation of the KF-induced disturbance.

## 5.4 Eigenvalue branching model

To describe the evolution of the discrete modes near the branch point we adopt an eigenvalue branching model of the form proposed by Fedorov and Khokhlov [34]

$$\alpha_{1,2} = \alpha_b \mp i\eta X^{1/2}, \quad X = x_1 - x_{1b}. \tag{5.4.1}$$

Here $\alpha_b$ is the value of the eigenvalues where they coincide and $\eta$ is in general a complex valued parameter that must be determined for each $\omega$ and $\beta$. The discrete mode branch point, which is in general complex, is denoted by $x_{1b}$. A demonstration of the behavior of model (5.4.1) is provided in Figure 5.4 for parameters $\alpha_b = 5.0 + 0.5i$, $\eta = 1.0$ and branch point $x_{1b} = 1.0 \pm 0.01i$, respectively. The branching topology changes depending on whether the branch point is bypassed from above or below along the real axis. The mode with label 'Mode 1' is unstable in both cases, but its identity (e.g. Mode S or Mode F), determined by the behavior upstream, differs between the two plots.

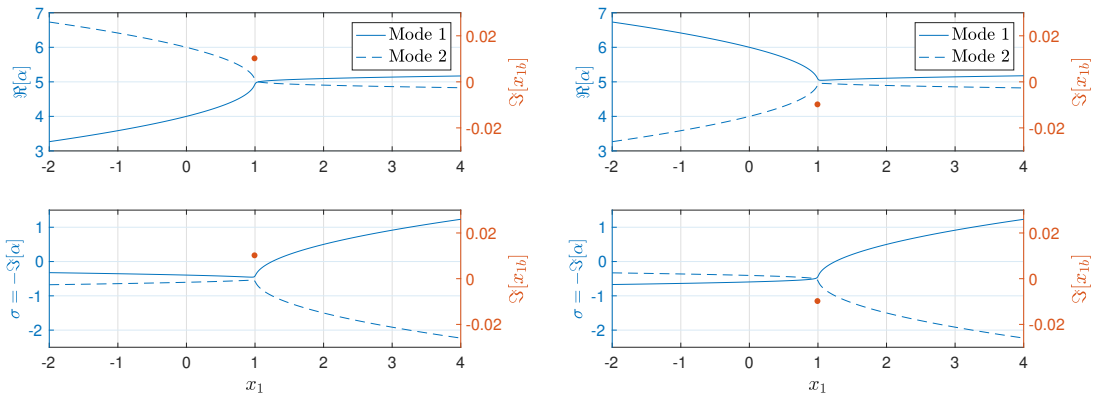


FIGURE 5.4. Eigenvalue topology captured by the branching model (5.4.1).

For simplicity, we assume in this work that the branch point lies on the real axis, i.e. $\Im[R_{\text{br}}] = 0$, as is approximately true for Case A. For definiteness and without loss of generality, we assume $\Re[\eta] > 0$, which ensures that the mode labeled as Mode 1 is the unstable mode. Finally, we assume $\Im[\eta] = 0$ which implies that the real and imaginary parts of $\alpha_{1,2}$ are constant, respectively, after and before the branch point. Since the growth rate is small and negative where the eigenvalues coincide, the model results in modes which are stable and nearly neutral upstream of the branch point. Thus, based on the results of Chapter 4, we expect the receptivity solution derived in this section to capture the elongated region of effective excitation typical for hypersonic configurations.

### 5.4.1 Expansion of the LST eigenvalue problem

For $|X| \ll 1$, the eigenvalues of modes 1 and 2 are assumed to evolve according to (5.4.1). The eigenvectors $\boldsymbol{A}_j$ are expanded as

$$\boldsymbol{A}_{1,2} = \boldsymbol{A}^{(0)} + (\alpha_{1,2} - \alpha_b)\boldsymbol{A}^{(1)} + \cdots \tag{5.4.2}$$

$$= \boldsymbol{A}^{(0)} \mp i\eta X^{\frac{1}{2}}\boldsymbol{A}^{(1)} + O\left(X\right). \tag{5.4.3}$$

The operator $\mathrm{H}_0$, which depends on $x_1$ through mean flow quantities as well as through the eigenvalue $\alpha = \alpha(x_1)$, is expanded as

$$\mathrm{H}_0 = \mathrm{H}_{0b} \mp i\eta X^{\frac{1}{2}} \frac{\partial \mathrm{H}_{0b}}{\partial \alpha} + X \left[ \frac{\partial \mathrm{H}_{0b}}{\partial x_1} - \frac{1}{2}\eta^2 \frac{\partial^2 \mathrm{H}_{0b}}{\partial \alpha^2} \right] + O\left(X^{\frac{3}{2}}\right). \tag{5.4.4}$$

The operator $-i\partial \mathrm{H}_0/\partial\alpha$ is expanded similarly. The non-parallel operator $\mathrm{H}_3$, which does not depend on $\alpha$, is expanded as

$$\mathrm{H}_3 = \mathrm{H}_{3b} + X \frac{\partial \mathrm{H}_{3b}}{\partial x_1} + \cdots . \tag{5.4.5}$$

Expanding the LST eigenvalue problem (5.3.7) accordingly and collecting terms in ascending powers of $X$ yields the following series of linear problems:

$$O(1): \qquad \mathcal{L}_{0b} \boldsymbol{A}^{(0)} = 0, \tag{5.4.6}$$

$$O(X^{\frac{1}{2}}): \qquad \mathcal{L}_{0b} \boldsymbol{A}^{(1)} = \frac{\partial \mathrm{H}_{0b}}{\partial \alpha} \boldsymbol{A}^{(0)}, \tag{5.4.7}$$

$$O(X): \qquad \mathcal{L}_{0b} \boldsymbol{A}^{(2)} = \left[ \frac{\partial \mathrm{H}_{0b}}{\partial x_1} - \frac{1}{2}\eta^2 \frac{\partial^2 \mathrm{H}_{0b}}{\partial \alpha^2} \right] \boldsymbol{A}^{(0)} - \eta^2 \frac{\partial \mathrm{H}_{0b}}{\partial \alpha} \boldsymbol{A}^{(1)}. \tag{5.4.8}$$

Equation (5.4.6) is simply the LST eigenvalue problem at the discrete mode branch point. Applying the solvability condition to (5.4.7) and (5.4.8) yields the useful identities

$$\left\langle \frac{\partial \mathrm{H}_{0b}}{\partial \alpha} \boldsymbol{A}^{(0)}, \boldsymbol{B}^{(0)} \right\rangle = 0, \tag{5.4.9}$$

and

$$\eta^2 = \frac{\left\langle \frac{\partial \mathrm{H}_{0b}}{\partial x_1} \boldsymbol{A}^{(0)}, \boldsymbol{B}^{(0)} \right\rangle}{\left\langle \frac{1}{2} \frac{\partial^2 \mathrm{H}_{0b}}{\partial \alpha^2} \boldsymbol{A}^{(0)} + \frac{\partial \mathrm{H}_{0b}}{\partial \alpha} \boldsymbol{A}^{(1)}, \boldsymbol{B}^{(0)} \right\rangle}. \tag{5.4.10}$$

Identity (5.4.9) simply reflects the biorthogonality condition which says that the scalar product $\Gamma$ vanishes when two modes exactly coincide. It is this condition that facilitates a numerical search for discrete mode branch points. In practice, this is accomplished by iterating on the complex Reynold's number via a 2D Newton-Raphson scheme until (5.4.9) is satisfied to within a given tolerance. Identity (5.4.10) allows

the receptivity solution to ultimately be expressed without explicit dependence on the eigenfunction correction term $\boldsymbol{A}^{(1)}$. Since parameter $\eta$, which in principle could be computed via (5.4.10), may for our purposes be estimated via a simple least squares procedure, this eliminates the need to solve the inhomogeneous equation (5.4.7) for $\boldsymbol{A}^{(1)}$.

### 5.4.2 Expansion of the two-mode ODEs

The equations governing the amplitudes of modes 1 and 2 under the two-mode approximation may be written as

$$\frac{\mathrm{d}c_1}{\mathrm{d}x_1} + \frac{M_{11}}{\Gamma_{11}}c_1 = -\left[\frac{M_{21}}{\Gamma_{11}}c_2 K_2 + \epsilon^{-1}\frac{\left\langle \hat{\boldsymbol{G}}^{(L)}, \boldsymbol{B}_1 \right\rangle}{\Gamma_{11}}\right] K_1^{-1} \tag{5.4.11}$$

$$\frac{\mathrm{d}c_2}{\mathrm{d}x_1} + \frac{M_{22}}{\Gamma_{22}}c_2 = -\left[\frac{M_{12}}{\Gamma_{22}}c_1 K_1 + \epsilon^{-1}\frac{\left\langle \hat{\boldsymbol{G}}^{(L)}, \boldsymbol{B}_2 \right\rangle}{\Gamma_{22}}\right] K_2^{-1}. \tag{5.4.12}$$

From this form it is evident that each mode is excited by both its discrete spectrum counterpart and the external forcing to the extent that these components are in resonance with the mode in question. In what follows, it is convenient to specify the lower integration bound in the definition of $K_j$ as the branch point $x_{1b}$ (as opposed to the neutral point $x_{10}$), i.e.

$$K_j = \exp\left(i\epsilon^{-1}\int_{x_{1b}}^{x_1}\alpha_j(x_1)\mathrm{d}x_1\right). \tag{5.4.13}$$

This simplifies the manipulations and has no bearing on the final solution. With this definition the local approximation to $K_j$, denoted by $\tilde{K}_j$, may be expressed as

$$\tilde{K}_j = \exp\left(i\epsilon^{-1}\alpha_b X \pm \epsilon^{-1}\frac{2}{3}\eta X^{3/2}\right). \tag{5.4.14}$$

The eigenvectors and matrix operators are expanded according to (5.4.3), (5.4.4) and (5.4.5). Coefficient $\Gamma_{jj}$, defined in (5.3.12), is estimated to leading order as

$$\Gamma_{jj} = (-1)^j\, 2\eta X^{1/2}\left[\left\langle \frac{\partial \mathrm{H}_{0b}}{\partial\alpha}\boldsymbol{A}^{(1)}, \boldsymbol{B}^{(0)}\right\rangle + \frac{1}{2}\left\langle \frac{\partial^2 \mathrm{H}_{0b}}{\partial\alpha^2}\boldsymbol{A}^{(0)}, \boldsymbol{B}^{(0)}\right\rangle\right], \tag{5.4.15}$$

where the $O(1)$ term has vanished due to the branch point identity (5.4.9). Using identity (5.4.10) for $\eta$, we may rewrite the above expression without explicit dependence on $\boldsymbol{A}^{(1)}$ as

$$\Gamma_{jj} = (-1)^j \frac{2X^{1/2}}{\eta} \left\langle \frac{\partial \mathrm{H}_{0b}}{\partial x_1} \boldsymbol{A}^{(0)}, \boldsymbol{B}^{(0)} \right\rangle. \tag{5.4.16}$$

Coefficient $M_{ji}$, defined in (5.3.12), may be expanded in a similar fashion. Since $\partial \boldsymbol{A}_j / \partial x_1 \sim X^{-1/2}$, the leading order behavior of $M_{ji}$ is $\sim X^{-1/2}$ and thus $O(1)$ terms, including those involving $\mathrm{H}_3$, do not appear to leading order. This leads to the simple lead order asymptotic expression

$$M_{kj}\Gamma_{jj}^{-1} = \frac{(-1)^{j+k}}{4X}. \tag{5.4.17}$$

Finally, the forcing term is expressed locally to leading order as

$$\epsilon^{-1}\Gamma_{jj}^{-1} \left\langle \hat{\boldsymbol{G}}^{(L)}, \boldsymbol{B}_j \right\rangle K_j^{-1} = (-1)^j \epsilon^{-1} \frac{\eta Q}{2X^{1/2}} \tilde{K}_j^{-1} \tag{5.4.18}$$

where

$$Q(x_1) = \frac{\left\langle \hat{\boldsymbol{G}}^{(L)}, \boldsymbol{B}^{(0)} \right\rangle}{\left\langle \dfrac{\partial \mathrm{H}_{0b}}{\partial x_1} \boldsymbol{A}^{(0)}, \boldsymbol{B}^{(0)} \right\rangle}. \tag{5.4.19}$$

Inserting these expressions into Equations (5.3.11) governing the amplitude of the discrete modes yields the local evolution equations

$$\frac{\mathrm{d}c_1}{\mathrm{d}x_1} + \frac{1}{4X} c_1 = \left[ \frac{1}{4X} c_2 \tilde{K}_2 + \epsilon^{-1} \frac{\eta Q}{2X^{1/2}} \right] \tilde{K}_1^{-1} \tag{5.4.20}$$

$$\frac{\mathrm{d}c_2}{\mathrm{d}x_1} + \frac{1}{4X} c_2 = \left[ \frac{1}{4X} c_1 \tilde{K}_1 - \epsilon^{-1} \frac{\eta Q}{2X^{1/2}} \right] \tilde{K}_2^{-1}, \tag{5.4.21}$$

valid in the region $X \ll 1$.

## 5.5 Solution to the receptivity problem

To understand how to proceed, we make the following observation. Assume that $X \ll 1$ and that mode coupling effects are negligible, as was the case in the context

of Chapter 4. Using the eigenvalue expansion (5.4.1), we express the KF-induced disturbance in terms of the dominant mode as

$$\hat{\boldsymbol{F}}_1 = c_1(x_1)\boldsymbol{A}^{(0)}(y)K_1(x_1) \tag{5.5.1}$$

$$= c_1(x_1)\boldsymbol{A}^{(0)}(y)\exp\left(i\epsilon^{-1}\alpha_b X + \epsilon^{-1}\frac{2\eta}{3}X^{3/2}\right). \tag{5.5.2}$$

Significantly far downstream of the excitation region, the amplitude of mode 1 is governed by the equation

$$\frac{\mathrm{d}c_1}{\mathrm{d}x_1} + \frac{1}{4X}c_1 = 0. \tag{5.5.3}$$

which has analytical solution

$$c_1 = C_1\exp\left(-\frac{1}{4}\ln X\right) = C_1 X^{-1/4}. \tag{5.5.4}$$

This allows $\hat{\boldsymbol{F}}_1$ to be expressed in the form

$$\hat{\boldsymbol{F}}_1 = \phi_1(x_1)\boldsymbol{A}^{(0)}(y)\exp\left(i\epsilon^{-1}\alpha_b X\right), \quad \phi_1 = C_1 X^{-1/4}\exp\left(\epsilon^{-1}\frac{2\eta}{3}X^{3/2}\right). \tag{5.5.5}$$

Observe that the amplitude function $\phi_1$ exactly matches the asymptotic behavior for large positive input of a solution to the Airy equation

$$\epsilon^2\frac{\mathrm{d}^2\phi}{\mathrm{d}X^2} - \eta^2 X\phi = 0. \tag{5.5.6}$$

From another perspective, $\phi_1$ may be viewed as the physical-optics level WKB approximation to a solution of equation (5.5.6), which has a turning point at $X = 0$. A standard analysis shows that such an approximation is valid provided that

$$X \gg \left(\frac{\epsilon}{\eta}\right)^{2/3}. \tag{5.5.7}$$

In light of this fact, we introduce the inner variable $\zeta = (\epsilon/\eta)^{-2/3}X$, which reduces equation (5.5.6) to the simple form

$$\phi''(\zeta) - \zeta\phi(\zeta) = 0. \tag{5.5.8}$$

This analysis suggests that if the solution in the vicinity of the branch point is to match the solution in the intermediate region $(\epsilon/\eta)^{2/3} \ll X \ll 1$, the disturbance should be locally governed by an Airy equation of the form (5.5.8). Since we are interested in solving the receptivity problem, the equation should be inhomogeneous with forcing related to kinetic fluctuations.

### 5.5.1 Solution to the receptivity problem

Motivated by the preceding discussion, the solution in the inner region $X = O\left(\epsilon^{2/3}\eta^{-2/3}\right)$ is expressed in terms of the inner variable $\zeta$ as

$$\hat{\boldsymbol{F}}_{in} = \phi(\zeta)\boldsymbol{A}^{(0)}(y)E(\zeta), \quad E = \exp\left(i\alpha_b\epsilon^{-1/3}\eta^{-2/3}\zeta\right), \tag{5.5.9}$$

where $\phi$ is determined by an inhomogeneous Airy equation to be derived now. We begin with equations (5.4.20)-(5.4.21) which may be expressed in terms of $\zeta$ as

$$\frac{\mathrm{d}c_1}{\mathrm{d}\zeta} + \frac{1}{4\zeta}c_1 = \left[\frac{1}{4\zeta}c_2\tilde{K}_2 + \left(\frac{\eta}{\epsilon}\right)^{2/3}\frac{Q}{2\zeta^{1/2}}\right]\tilde{K}_1^{-1} \tag{5.5.10}$$

$$\frac{\mathrm{d}c_2}{\mathrm{d}\zeta} + \frac{1}{4\zeta}c_2 = \left[\frac{1}{4\zeta}c_1\tilde{K}_1 - \left(\frac{\eta}{\epsilon}\right)^{2/3}\frac{Q}{2\zeta^{1/2}}\right]\tilde{K}_2^{-1}. \tag{5.5.11}$$

By multiplying (5.5.10) and (5.5.11) by $\exp\left(\frac{2}{3}\zeta^{3/2}\right)$ and $\exp\left(-\frac{2}{3}\zeta^{3/2}\right)$, respectively, then adding or subtracting the second from the first, we obtain two useful identities:

$$c_1'\exp\left(\tfrac{2}{3}\zeta^{3/2}\right) + c_2'\exp\left(-\tfrac{2}{3}\zeta^{3/2}\right) = 0, \tag{5.5.12}$$

and

$$c_1'\exp\left(\tfrac{2}{3}\zeta^{3/2}\right) - c_2'\exp\left(-\tfrac{2}{3}\zeta^{3/2}\right) + \frac{1}{2\zeta}\left[c_1\exp\left(\tfrac{2}{3}\zeta^{3/2}\right) - c_2\exp\left(-\tfrac{2}{3}\zeta^{3/2}\right)\right] = \left(\frac{\eta}{\epsilon}\right)^{2/3}\frac{Q}{\zeta^{1/2}}E. \tag{5.5.13}$$

Here $\cdot'$ denotes differentiation in $\zeta$. Motivated by the discussion in the preceding section, we introduce the change of variables

$$\phi(\zeta) = c_1\exp\left(\tfrac{2}{3}\zeta^{3/2}\right) + c_2\exp\left(-\tfrac{2}{3}\zeta^{3/2}\right), \tag{5.5.14}$$

effectively replacing the approximation by a sum of exponentials with the general function $\phi$. Taking the derivative of $\phi$ with respect to $\zeta$ and using identity (5.5.12) yields

$$\phi' = \zeta^{1/2}\left[c_1 \exp\left(\tfrac{2}{3}\zeta^{3/2}\right) - c_2 \exp\left(-\tfrac{2}{3}\zeta^{3/2}\right)\right]. \tag{5.5.15}$$

A second differentiation yields

$$\phi'' - \zeta\phi = \zeta^{1/2}\left(c_1' \exp\left(\tfrac{2}{3}\zeta^{3/2}\right) - c_2' \exp\left(-\tfrac{2}{3}\zeta^{3/2}\right)\right) + \frac{1}{2\zeta^{1/2}}\left(c_1 \exp\left(\tfrac{2}{3}\zeta^{3/2}\right) - c_2 \exp\left(-\tfrac{2}{3}\zeta^{3/2}\right)\right). \tag{5.5.16}$$

Finally, using identity (5.5.13), the right hand side of (5.5.16) may be expressed in terms of the random forcing, reducing it to the inhomogeneous Airy type equation

$$\phi'' - \zeta\phi = \left(\frac{\eta}{\epsilon}\right)^{2/3} QE. \tag{5.5.17}$$

Since $Q$, defined in (5.4.19), is regular at $\zeta = 0$, so too is the solution of (5.5.17), indicating that there is no singularity at the branch point. Equation (5.5.17) may be solved formally through a variation of parameters approach assuming a solution of the form

$$\phi(\zeta) = u(\zeta)\mathrm{Ai}(\zeta) + v(\zeta)\mathrm{Bi}(\zeta), \tag{5.5.18}$$

where Ai and Bi are the standard Airy functions, solutions to the homogeneous form of equation (5.5.17). If the disturbance has negligible amplitude upstream of the inner region, we find

$$u(\zeta) = \pi\left(\frac{\eta}{\epsilon}\right)^{2/3} \int_{-\infty}^{\zeta} \mathrm{Bi}(\zeta')Q(\zeta')E(\zeta')\mathrm{d}\zeta', \tag{5.5.19}$$

$$v(\zeta) = -\pi\left(\frac{\eta}{\epsilon}\right)^{2/3} \int_{-\infty}^{\zeta} \mathrm{Ai}(\zeta')Q(\zeta')E(\zeta')\mathrm{d}\zeta', \tag{5.5.20}$$

so that the full solution may be expressed as

$$\phi = \pi\left(\frac{\eta}{\epsilon}\right)^{2/3} \int_{-\infty}^{\zeta} \left[\mathrm{Ai}(\zeta)\mathrm{Bi}(\zeta') - \mathrm{Bi}(\zeta)\mathrm{Ai}(\zeta')\right] Q(\zeta')E(\zeta')\mathrm{d}\zeta'. \tag{5.5.21}$$

The asymptotic behavior of the Airy functions for $\zeta \to +\infty$ is given by

$$\mathrm{Ai}(\zeta) \sim \frac{1}{2\sqrt{\pi}}\zeta^{-\frac{1}{4}} \exp\left(-\tfrac{2}{3}\zeta^{3/2}\right), \quad \mathrm{Bi}(\zeta) \sim \frac{1}{\sqrt{\pi}}\zeta^{-\frac{1}{4}} \exp\left(\tfrac{2}{3}\zeta^{3/2}\right), \quad \zeta \to +\infty. \tag{5.5.22}$$

The behavior of $\phi$ for $\zeta \to \infty$ may thus be expressed as

$$\phi(\zeta) = \frac{v(\zeta)}{\sqrt{\pi}}\zeta^{-\frac{1}{4}} \exp\left(\tfrac{2}{3}\zeta^{3/2}\right), \quad \zeta \to \infty, \tag{5.5.23}$$

and the inner solution outside of the branch point region is given by

$$\hat{\boldsymbol{F}}_{in} = \frac{v(\zeta)}{\sqrt{\pi}}\zeta^{-1/4}\boldsymbol{A}^{(0)}(y) \exp\left(i\alpha_b\epsilon^{-1/3}\eta^{-2/3}\zeta + \frac{2}{3}\zeta^{3/2}\right), \quad \zeta \to \infty. \tag{5.5.24}$$

Rewriting (5.5.24) in terms of the outer variable $X$ and using expression (5.5.19) for $v$ we have

$$\hat{\boldsymbol{F}}_{in} = \sqrt{\pi}\eta\left(\frac{\eta}{\epsilon}\right)^{1/6} \int_0^\infty \mathrm{Ai}\left(\epsilon^{-2/3}\eta^{2/3}X'\right) Q \exp\left(-i\epsilon^{-1}\alpha_b X'\right) \mathrm{d}x_1' \times \\ X^{-1/4}\boldsymbol{A}^{(0)}(y) \exp\left(\epsilon^{-1}\left[i\alpha_b X + \eta\frac{2}{3}X^{3/2}\right]\right), \quad X \gg \epsilon^{2/3}. \tag{5.5.25}$$

The outer solution is expressed as

$$\hat{\boldsymbol{F}}_{out} = \sum_{k=1,2} C_k \boldsymbol{A}(x_1, y) K_k^{(np)}(x_1), \tag{5.5.26}$$

$$K_k^{(np)} = \exp\left(\int^{x_1} i\epsilon^{-1}\alpha_k - \Gamma_{kk}^{-1}M_{kk}\mathrm{d}x_1'\right), \tag{5.5.27}$$

or in the intermediate region $\epsilon^{2/3} \ll X \ll 1$ as

$$\hat{\boldsymbol{F}}_{out} = \left[C_1 \exp\left(\epsilon^{-1}\eta\frac{2}{3}X^{3/2}\right) + C_2 \exp\left(-\epsilon^{-1}\eta\frac{2}{3}X^{3/2}\right)\right] \times \\ X^{-1/4}\boldsymbol{A}^{(0)}(y) \exp\left(i\epsilon^{-1}\alpha_b X\right). \tag{5.5.28}$$

Comparing this expression with the inner solution (5.5.25), we find that the disturbance outside the excitation region is given by

$$\hat{\boldsymbol{F}}_{out}(x_1, y) = C_1 \boldsymbol{A}(x_1, y) K_1^{(np)}(x_1), \tag{5.5.29}$$

with

$$C_1 = \sqrt{\pi}\eta \left(\frac{\eta}{\epsilon}\right)^{1/6} \int_0^\infty \mathrm{Ai}\left(\epsilon^{-2/3}\eta^{2/3}X'\right) Q \exp\left(-i\epsilon^{-1}\alpha_b X'\right) \mathrm{d}x_1', \tag{5.5.30}$$

$$Q(x_1) = \frac{\left\langle \hat{\boldsymbol{G}}^{(L)}, \boldsymbol{B}^{(0)} \right\rangle}{\left\langle \dfrac{\partial \mathrm{H}_{0b}}{\partial x_1} \boldsymbol{A}^{(0)}, \boldsymbol{B}^{(0)} \right\rangle}. \tag{5.5.31}$$

### 5.5.2 Mean-square disturbance

Downstream of the branch point influence domain $x_1 - x_{1b} = O(\epsilon^{2/3})$, the disturbance induced by kinetic fluctuations, upon inverting the Fourier transform, is given by

$$\boldsymbol{f}(x_1, y) = \frac{\epsilon_L}{(2\pi)^2} \iint_{-\infty}^{\infty} C_1(\omega, \beta) \boldsymbol{A}(x_1, y, \omega, \beta) K^{(np)}(x_1, \omega, \beta) e^{i(\omega t - \beta z)} \mathrm{d}\omega \mathrm{d}\beta. \tag{5.5.32}$$

As was done in previous chapters, the eigenfunction $\boldsymbol{A}$ may be replaced by one of its components, say, the wall pressure $A_4(x_1, y = 0, \beta, \omega)$, in order to facilitate a particular physical interpretation. If the eigenfunction is then normalized so that this quantity is unity, then the expression for the disturbance is simply

$$f(x_1) = \frac{\epsilon_L}{(2\pi)^2} \iint_{-\infty}^{\infty} C_1(\omega, \beta) K^{(np)}(x_1, \omega, \beta) e^{i(\omega t - \beta z)} \mathrm{d}\omega \mathrm{d}\beta. \tag{5.5.33}$$

Since $C_1$ is a random quantity, we quantify the magnitude of the induced disturbance $f$ through its root-mean-square. To this end, we first compute the mean square of $C_1$. Multiplying $C_1$ by its complex conjugate and taking an ensemble average yields

$$\overline{|C_1|^2} = (2\pi)^2 \delta(\beta - \beta') \delta(\omega - \omega') \left(\sqrt{\pi}\eta \left(\frac{\eta}{\epsilon}\right)^{1/6}\right)^2 \times \int_0^\infty \left(Q^2\right)_{\omega,\beta} \left|\mathrm{Ai}(\zeta) \exp\left(\epsilon^{-1}\alpha_{b,i} X\right)\right|^2 \mathrm{d}x_1, \tag{5.5.34}$$

where we have used the expressions for the correlations between the fluctuating dissipative fluxes. In terms of the quantity $(q^2)_{\alpha,\beta,\omega}$ defined in the previous two chapters,

the spectral density $(Q^2)_{\omega,\beta}$ may be expressed as

$$\left(Q^2\right)_{\omega,\beta} = \frac{(q^2)_{\alpha,\beta,\omega}\left|\Gamma\right|^2}{\left|\left\langle \frac{\partial \mathrm{H}_{0b}}{\partial x_1}\boldsymbol{A}^{(0)}, \boldsymbol{B}^{(0)}\right\rangle\right|^2}. \tag{5.5.35}$$

Since the quantity $(q^2)_{\alpha,\beta,\omega}\left|\Gamma\right|^2$ is regular at the branch point, so is $(Q^2)_{\omega,\beta}$. Taking the mean square of $f$ and using

$$\left|K^{(np)}\right| = \exp\left(N^{(np)}\right), \quad N^{(np)} = \epsilon^{-1}\int^{x_1} \sigma - \epsilon\Re\left[\Gamma_{11}^{-1}M_{11}\right]\mathrm{d}x_1, \tag{5.5.36}$$

we obtain

$$\overline{|f|^2} = \frac{\epsilon_L^2}{(2\pi)^4}\iiiint_{-\infty}^{\infty}\overline{|C_1|^2}e^{2N^{(np)}(x_1,\omega,\beta)}\times e^{i((\omega-\omega')t-(\beta-\beta')z)}\mathrm{d}\omega\mathrm{d}\omega'\mathrm{d}\beta\mathrm{d}\beta'. \tag{5.5.37}$$

Finally, using expression (5.5.34) for $\overline{|C_1|^2}$, we have

$$\overline{|f|^2} = \frac{\epsilon_L^2}{(2\pi)^2}\iint_{-\infty}^{\infty} I(x_1,\omega,\beta)\left(e^{N^{(np)}(x_1,\omega,\beta)}\right)^2\mathrm{d}\omega\mathrm{d}\beta \tag{5.5.38}$$

where

$$I = \left(\sqrt{\pi}\eta\left(\frac{\eta}{\epsilon}\right)^{1/6}\right)^2\int_0^{\infty}\left(Q^2\right)_{\omega,\beta}\left|\mathrm{Ai}(\zeta)\exp\left(\epsilon^{-1}\alpha_{b,i}X\right)\right|^2\mathrm{d}x_1 \tag{5.5.39}$$

If the eigenfunction is normalized by the condition $A_4(x_1, y=0)=1$, then the result is $f_{rms} = \left(p_w^{*\prime}/P_e^*\right)_{rms}$, the magnitude of the KF-induced wall pressure disturbance relative to the pressure at the edge of the boundary layer.

## 5.6 Results & Discussion

To examine the receptivity solution derived in this chapter, we return our attention to Case A, for which the discrete mode branch point lies on or near the real axis for all frequencies of physical interest. For the sake of comparison, note that if the

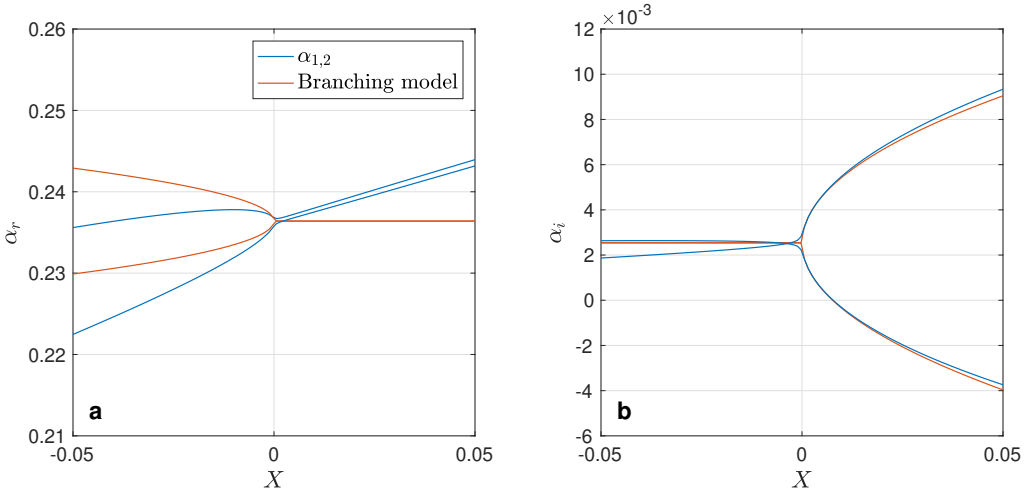


FIGURE 5.5. Behavior of the branching model with the actual eigenvalue evolution, Case A, $F = 2.5 \times 10^{-5}$.

streamwise length scale $L$ is set to the distance from the leading edge to the real part of the branch point, $L = \Re[x_b^*]$, then $x_{1b} = 1$ and

$$X = \frac{x^* - x_b^*}{L} = \left(\frac{R}{R_{\text{br}}}\right)^2 - 1. \tag{5.6.1}$$

The branch point in this frame corresponds to $X = 0$. The behavior of the branching model (5.4.1) for Case A, $F = 2.5 \times 10^{-5}$, is shown in Figure 5.5 as a function of $X$ with the actual eigenvalue evolution shown for comparison. For this case, the real parameter $\eta$ is found to be $\eta = 2.91 \times 10^{-2}$. It is evident that the disagreement in the real part of the eigenvalue $\alpha_r$ could be remedied through the inclusion of an $O(X)$ term in the branching model. These terms, however, do not appear in the lead order approximation adopted in the receptivity solution derived herein.

For Case A, we compare the integrand of (5.5.39), which we denote by

$$J_2(x_1, \omega, \beta) = \left(\sqrt{\pi}\eta \left(\frac{\eta}{\epsilon}\right)^{1/6}\right)^2 \left(Q^2\right)_{\omega,\beta} \left|\text{Ai}(\zeta) \exp\left(\epsilon^{-1}\alpha_{b,i} X\right)\right|^2, \tag{5.6.2}$$

with the analogous expression obtained in Chapter 4 under the single mode approxi-

mation

$$J_1(x_1,\omega,\beta) = \left(q^2\right)_{\omega,\beta} \left| \left( K_1^{(np)}(x_1,\omega,\beta) \right)^{-1} \right|^2 . \tag{5.6.3}$$

Figure 5.6a shows $J_1$ and $J_2$ as functions of $X$ for Case A, $F = 2.5 \times 10^{-5}$, $\beta = 0$. From a qualitative perspective, both functions peak near the branch point and decay exponentially in either direction. To emphasize the quantitative discrepancy near the branch point, Figure 5.6b provides a narrower view of the same functions on a linear scale with the neutral point indicated by a vertical dashed line.

Qualitatively, there are two fundamental differences between the two approximations, each of which represent an important physical insight. First, the smooth behavior of $J_2$ at $X = 0$ indicates that there is no strong peak in receptivity at the branch point. The singularity in $J_1$ is due to a failure in the method of approximation near the turning point rather than any physical mechanism. In cases of this kind, the approach adopted in Chapter 3 would be highly susceptible to large errors due to the proximity of the branch point to the neutral point.

The other fundamental difference between the two integrands is the oscillations that appear in $J_2$ which are absent in $J_1$. The oscillations are a result of the superposition of waves of mode 1 and 2, the phases of which are asynchronous upstream of the branch point. This constructive/destructive superposition effectively limits the length of the excitation region upstream. For $X > 0$, the phases are synchronized and no oscillations are present. This phenomenon is of course not captured in $J_1$ which takes into account only the unstable mode.

To explore the latter point further, consider the superposition $\tilde{K}_1 + \tilde{K}_2$, where, as before

$$\tilde{K}_{1,2} = \exp\left( i\epsilon^{-1} \int_{x1b}^{x_1} \alpha_{1,2}\, \mathrm{d}x_1 \right), \quad \alpha_{1,2} = \alpha_b \mp i\eta X^{1/2}. \tag{5.6.4}$$

Figure 5.7 shows the real part and the absolute value of the superposition. The quantity $2\left|\tilde{K}_1\right|$ is shown for comparison. The wavelength of the envelope is determined by the synchronization of the two waves and is much longer than the actual disturbance

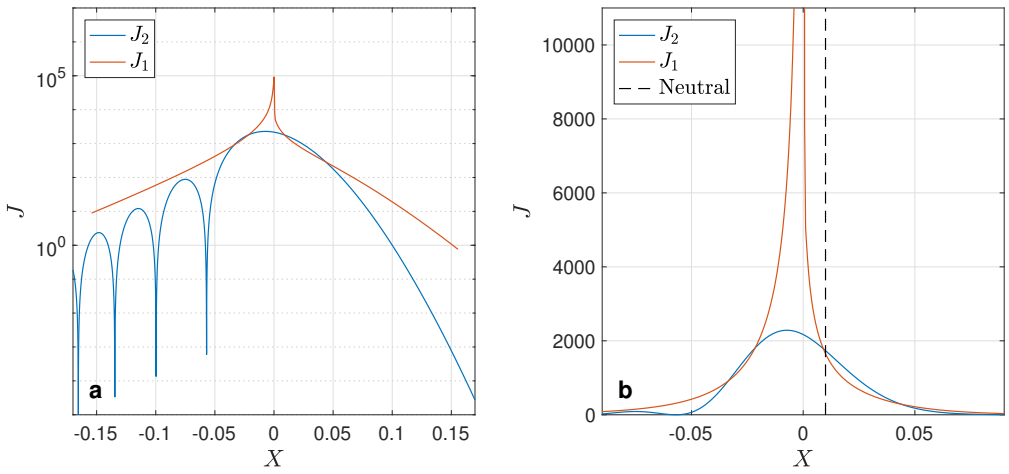


FIGURE 5.6. Comparison integrands obtained under the single-mode and two-mode approximation, Case A, $F = 2.5 \times 10^{-5}$.

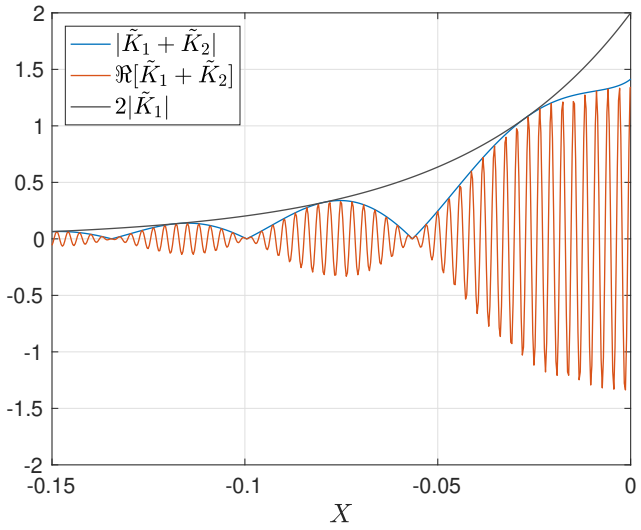


FIGURE 5.7. A demonstration of the effect of superposition of waves of mode 1 and 2 upstream of the branch point.

wavelength. This additional scale suggests a mechanism by which forcing waves with wavelength much larger than $\alpha$ could excite unstable boundary layer modes.

## 5.7 Conclusions

For many hypersonic configurations, Modes S and F are exactly or nearly synchronized just upstream of the instability onset. For such cases, the single-mode WKB approximation to the receptivity solution is singular at the branch point and is thus not applicable. The non-parallel correction to the eigenvalue evolution is also singular.

In this chapter we have resolved the singularity by accounting for two discrete modes in the synchronization region. In the two-mode approximation, the disturbance is governed locally by a forced Airy equation which may be solved explicitly. This results in the following observations. First, upstream of the branch point, the asynchrony of the two modes results in constructive-destructive cancellation, which is only accounted for under a two-mode approximation. Additionally, the smoothness of the two-mode approximation indicates that there is no singularity or strong peak in receptivity at the branch point. It also suggests that the non-parallel effect on the growth rate of either mode is not strong for the hypersonic case considered.

Our results suggest that the approach adopted in Chapter 3 should not be applied in cases where Modes S and F are nearly synchronized. In such cases, a local approximation at the neutral point could result in order of magnitude errors due to the singularity at the nearby branch point. If non-parallel effects are neglected, the approach of Chapter 4 is unlikely to yield results which exhibit order of magnitude differences from the two-mode approximation derived in this chapter. Still, the approximation adopted there conceals important features of the excitation region and can lead to misleading results when modes S and F and synchronized. The approach outlined in this chapter allows for the inclusion of non-parallel effects and yields a regular, physically consistent solution. The solutions to the KF-receptivity problem

presented herein, and particularly in Chapters 4 and 5, will allow for evaluation of the role of thermal noise in laminar-transition through comparison of theoretically predicted and experimentally observed transition locations for a broad range of hypersonic flight configurations.

# Appendix A

## A.1 Single-mode excitation region

In the literature, it is frequently asserted that excitation of the mode with neutral point eigenvalue $\alpha(x_{10}) = \alpha_0$ occurs in the region $x_1 - x_{10} = O\left(\epsilon^{1/2}\right)$, due to a contribution from forcing wavenumbers in the range $\alpha_f - \alpha_0 = O\left(\epsilon^{1/2}\right)$. A simple explanation of these claims, which is lacking in the modern literature, is as follows. Consider a general boundary layer forcing component $\boldsymbol{f}$ that varies in the streamwise direction as $\boldsymbol{f} \propto \exp\left(i\epsilon^{-1}\alpha_f x_1\right)$. The induced response may be expressed in terms of the dominant unstable mode of the discrete spectrum as

$$\hat{\boldsymbol{F}} = c(x_1)\boldsymbol{A}(y)K(x_1), \tag{A.1.1}$$

with $K$ as defined in (3.3.2). It is shown in Chapter 4 that the amplitude function $c$, in the absence of non-parallel effects, is governed by an equation of the form

$$\frac{\mathrm{d}c}{\mathrm{d}x_1} \propto \exp\left(i\epsilon^{-1}\alpha_f x_1\right) K(x_1)^{-1}. \tag{A.1.2}$$

We expect effective excitation to occur in some neighborhood of the pure resonance condition $\alpha_0 = \alpha_f$. We thus expand the unstable mode wavenumber about the neutral point as

$$\alpha = \alpha_0 + b(x_1 - x_{10}) + \cdots, \quad b = \left.\frac{\mathrm{d}\alpha}{\mathrm{d}x_1}\right|_{x_{10}}, \tag{A.1.3}$$

and consider real forcing wavenumbers of the form $\alpha_f = \alpha_0 + \delta$, where $\delta$ is a detuning parameter whose order is to be determined. Note that the eigenvalue derivative at the neutral point may be expressed as $b = b_r - i|\sigma_{x_{10}}|$, where $\sigma_{x_{10}}$ is the derivative of the growth rate at the neutral point. Inserting these expressions into (A.1.2) yields

$$\frac{\mathrm{d}c}{\mathrm{d}x_1} \propto$$
$$\exp\left(-\frac{\epsilon^{-1}|\sigma_{x_{10}}|}{2}(x_1 - x_{10})^2\right) \exp\left(i\epsilon^{-1}\left[\delta(x_1 - x_{10}) - \frac{b_r}{2}(x_1 - x_{10})^2\right]\right). \quad \text{(A.1.4)}$$

Necessary conditions for significant mode excitation are thus obtained by requiring that the first exponential in (A.1.4) is not small and that the second is not rapidly oscillating. The first requirement imposes the condition

$$x_1 - x_{10} = O\left(\sqrt{\frac{\epsilon}{|\sigma_{x_{10}}|}}\right). \quad \text{(A.1.5)}$$

Assuming the eigenvalue $\alpha$ is a slow function of $x_1$, we have $\sigma_{x_{10}} = O(1)$ and $b_r = O(1)$. This reduces (A.1.5) to the condition $x_1 - x_{10} = O\left(\epsilon^{1/2}\right)$. It also implies that the first term in the second exponential of (A.1.4) will result in rapid oscillations unless $\delta$ is sufficiently small. In particular, we must have $\delta = O\left(\epsilon^{1/2}\right)$. In summary, assuming the growth rate gradient at the neutral point is $O(1)$, necessary conditions for effective excitation are

$$x_1 - x_{10} = O\left(\epsilon^{1/2}\right), \quad \text{and} \quad \alpha_f - \alpha_0 = O\left(\epsilon^{1/2}\right). \quad \text{(A.1.6)}$$

Based on the preceding argument, we proceed by considering forcing wavenumbers $\alpha_f = \alpha_0 + \epsilon^{1/2}\gamma$, where $\gamma = O(1)$ is a parameter reflecting detuning from pure resonance.

## A.2 Definition of $\mathbf{H}_0$, $\hat{\boldsymbol{G}}^{(L)}$ and $(q^2)_{\alpha,\beta,\omega}$

The non-zero elements $H_{ij}$ of operator $\mathbf{H}_0$, reproduced from Ref. [75], are as follows, where for brevity we use the notation $D = \mathrm{d}/\mathrm{d}y$, $\mu' = \mathrm{d}\mu_s/\mathrm{d}T_s$, $m = 2(e-1)/3$,

$r = 2(e+2)/3 = m+2$, $\mu_2/\mu = \frac{2}{3}e$; $\hat{\omega} = \omega - \alpha U_s - \beta W_s$, $\chi = \left[\frac{R}{\mu_s} - ir\gamma M^2\hat{\omega}\right]^{-1}$:

$$H_{12} = H_{56} = H_{78} = 1; \quad H_{21} = \alpha^2 + \beta^2 - i\hat{\omega}\frac{R}{\mu_s T_s};$$

$$H_{22} = -\frac{D\mu_s}{\mu_s}; \quad H_{23} = -i\alpha\left[(m+1)\frac{DT_s}{T_s} + \frac{D\mu_s}{\mu_s}\right] + \frac{RDU_s}{\mu_s T_s};$$

$$H_{24} = i\frac{\alpha R}{\mu_s} + (m+1)\gamma M^2\alpha\hat{\omega}; \quad H_{25} = -(m+1)\frac{\alpha\hat{\omega}}{T_s} - \frac{D(\mu_s' DU_s)}{\mu_s};$$

$$H_{26} = -\frac{\mu_s' DU_s}{\mu_s}; \quad H_{31} = -i\alpha; \quad H_{33} = \frac{DT_s}{T_s}; \quad H_{34} = i\gamma M^2\hat{\omega}; \quad H_{35} = -\frac{i\hat{\omega}}{T_s};$$

$$H_{37} = -i\beta; \quad H_{41} = -i\alpha\chi\left(r\frac{DT_s}{T_s} + 2\frac{D\mu_s}{\mu_s}\right); \quad H_{42} = -i\alpha\chi;$$

$$H_{43} = \chi\left[-\alpha^2 - \beta^2 + r\frac{D\mu_s DT_s}{\mu_s T_s} + r\frac{D^2 T_s}{T_s} + i\frac{R\hat{\omega}}{\mu_s T_s}\right];$$

$$H_{44} = -i\chi r\gamma M^2\left[\alpha DU_s + \beta DW_s - \hat{\omega}\left(\frac{DT_s}{T_s} + \frac{D\mu_s}{\mu_s}\right)\right];$$

$$H_{45} = i\chi\left[r\frac{(\alpha DU_s + \beta DW_s)}{T_s} + \mu_s'\frac{\alpha DU_s + \beta DW_s}{\mu_s} - r\hat{\omega}\frac{D\mu_s}{\mu_s T_s}\right];$$

$$H_{46} = -i\chi\hat{\omega}\frac{r}{T_s}; \quad H_{47} = -i\beta\chi\left(r\frac{DT_s}{T_s} + 2\frac{D\mu_s}{\mu_s}\right); \quad H_{48} = -i\beta\chi;$$

$$H_{62} = -2\,\mathrm{Pr}(\gamma-1)M^2 DU_s; \quad H_{63} = R\,\mathrm{Pr}\,\frac{DT_s}{\mu_s T_s} - 2i(\gamma-1)M^2\,\mathrm{Pr}(\alpha DU_s + \beta DW_s);$$

$$H_{64} = iR\,\mathrm{Pr}\,\frac{(\gamma-1)M^2}{\mu_s}\hat{\omega};$$

$$H_{65} = \alpha^2 + \beta^2 - iR\,\mathrm{Pr}\,\frac{\hat{\omega}}{\mu_s T_s} - (\gamma-1)M^2\,\mathrm{Pr}\,\frac{\mu_s'\left[(DU_s)^2 + (DW_s)^2\right]}{\mu_s} - \frac{D^2\mu_s}{\mu_s};$$

$$H_{66} = -2\frac{D\mu_s}{\mu_s}; \quad H_{68} = -2\,\mathrm{Pr}(\gamma-1)M^2 DW_s$$

$$H_{83} = \frac{RDW_s}{\mu_s T_s} - i\beta\left[(m+1)\frac{DT_s}{T_s} + \frac{D\mu_s}{\mu_s}\right];$$

$$H_{84} = i\frac{\beta R}{\mu_s} + (m+1)\gamma M^2\beta\hat{\omega}; \quad H_{85} = -(m+1)\frac{\beta}{T}\hat{\omega} - \frac{D(\mu_s' DW_s)}{\mu_s};$$

$$H_{86} = -\frac{\mu_s' DW_s}{\mu_s}; \quad H_{87} = \alpha^2 + \beta^2 - i\hat{\omega}\frac{R}{\mu_s T_s}; \quad H_{88} = -\frac{D\mu_s}{\mu_s}.$$

The elements of the stochastic forcing vector $\hat{\boldsymbol{G}}^{(L)}$, reproduced from Ref. [39], are

$$\begin{aligned}
\hat{G}_1^{(L)} &= \hat{G}_3^{(L)} = \hat{G}_5^{(L)} = \hat{G}_7^{(L)} = 0 \\
\hat{G}_2^{(L)} &= -\frac{R}{\mu_s}\left(\frac{\partial \delta\hat{\Pi}_{xx}}{\partial x} + \frac{\partial \delta\hat{\Pi}_{xy}}{\partial y} + i\beta\delta\hat{\Pi}_{xz}\right) \\
G_4^{(L)} &= \frac{\partial \delta\hat{\Pi}_{yx}}{\partial x} + \frac{\partial \delta\hat{\Pi}_{yy}}{\partial y} + i\beta\delta\hat{\Pi}_{yz} \\
\hat{G}_6^{(L)} &= \frac{R\,\mathrm{Pr}}{\mu_s}\left(\frac{(\gamma-1)\,M^2}{\mathrm{Pr}}\right)^{1/2}\left(\frac{\partial \delta\hat{Q}_x}{\partial x} + \frac{\partial \delta\hat{Q}_y}{\partial y} + i\beta\delta\hat{Q}_z\right) - \\
&\frac{R\,\mathrm{Pr}}{\mu_s}\frac{(\gamma-1)M^2}{2}\left[\left(\delta\hat{\Pi}_{xy} + \delta\hat{\Pi}_{yx}\right)\frac{\partial U_s}{\partial y} + \left(\delta\hat{\Pi}_{yz} + \delta\hat{\Pi}_{zy}\right)\frac{\partial W_s}{\partial y}\right] \\
\hat{G}_8^{(L)} &= -\frac{R}{\mu_s}\left(\frac{\partial \delta\hat{\Pi}_{zx}}{\partial x} + \frac{\partial \delta\hat{\Pi}_{zy}}{\partial y} + i\beta\delta\hat{\Pi}_{zz}\right).
\end{aligned}$$

The spectral density $(q^2)_{\alpha,\beta,\omega}$ may be expressed as

$$(q^2)_{\alpha,\beta,\omega} = |\Gamma|^{-2}\left[j_{22} + j_{44} + j_{66} + j_{88} + 2\Re(j_{24} + j_{26} + j_{28} + j_{46} + j_{48} + j_{68})\right]$$

where

$$j_{22} = 2R^2\int_0^\infty \frac{T_s}{\mu_s}\left[r\alpha^2\left|B_2\right|^2 + \mu_s^2\left|D\left(\frac{B_2}{\mu_s}\right)\right|^2 + \beta^2\left|B_2\right|^2\right]dy$$

$$j_{44} = 2\int_0^\infty \mu_s T_s\left[\alpha^2\left|B_4\right|^2 + r\left|DB_4\right|^2 + \beta^2\left|B_4\right|^2\right]dy$$

$$j_{66} = 2\left(\gamma-1\right)M^2R^2\,\mathrm{Pr}\int_0^\infty \frac{T_s^2}{\mu_s}\left[\alpha^2\left|B_6\right|^2 + \mu_s^2\left|D\left(\frac{B_6}{\mu_s}\right)\right|^2) + \beta^2\left|B_6\right|^2\right]dy +$$
$$2\left[R\,\mathrm{Pr}(\gamma-1)M^2\right]^2\int_0^\infty \frac{T_s}{\mu_s}\left[(DU_s)^2 + (DW_s)^2\right]\left|B_6\right|^2 dy$$

$$j_{88} = 2R^2\int_0^\infty \frac{T_s}{\mu_s}\left[\alpha^2\left|B_8\right|^2 + \mu_s^2\left|D\left(\frac{B_8}{\mu_s}\right)\right|^2 + r\beta^2\left|B_8\right|^2\right]dy$$

$$j_{24} = 2i\alpha R\int_0^\infty T_s\left(mB_2DB_4^* - \left(DB_2 - B_2\left(\frac{D\mu_s}{\mu_s}\right)\right)B_4^*\right)dy$$

$$j_{26} = -2R^2 \Pr(\gamma - 1)M^2 \int_0^\infty \frac{T_s}{\mu_s} DU_s \left( DB_2 - B_2 \left( \frac{D\mu_s}{\mu_s} \right) \right) B_6^* dy$$

$$j_{28} = 2\alpha\beta R^2 \int_0^\infty \frac{T_s}{\mu_s} (m+1) B_2 B_8^* dy$$

$$j_{46} = -2R \Pr(\gamma - 1)M^2 \int_0^\infty T_s \left[ i\alpha DU_s + i\beta DW_s \right] B_4 B_6^* dy$$

$$j_{48} = 2i\beta R \int_0^\infty T_s \left[ B_4 \left( DB_8^* - B_8^* \left( \frac{D\mu_s}{\mu_s} \right) \right) - mDB_4 B_8^* \right] dy$$

$$j_{68} = -2R^2 \Pr(\gamma - 1)M^2 \int_0^\infty \frac{T_s}{\mu_s} DW_s B_6 \left( DB_8^* - B_8^* \left( \frac{D\mu_s}{\mu_s} \right) \right) dy.$$

## A.3 Expression for $c_1$ in terms of $(q^2)_{\alpha,\beta,\omega}$

The expression for amplitude $c_1$ is of the form

$$\begin{aligned} c_1(x_1) &\propto \int^{x_1} q(\eta) K(\eta)^{-1} \mathrm{d}\eta \\ &= \int^{x_1} \Gamma(\eta)^{-1} \left( \int_0^\infty \sum_{i=1}^{8} G_i B_i \mathrm{d}y \right) K(\eta)^{-1} \mathrm{d}\eta, \end{aligned}$$

where $G_i$ and $B_i$ are the elements of $\hat{\boldsymbol{G}}^{(L)}$ and $\boldsymbol{B}^{(0)}$. The order sum and inner integral may be swapped given the homogeneous boundary conditions on $\boldsymbol{B}^{(0)}$. Additionally, since $K^{-1}$ decays exponentially away from $x_{10}$, the order of the two integrals may be swapped assuming the observation point $x_1$ is sufficiently far downstream. Alternatively, we could introduce a test function guaranteeing the integrand is $L_1$. Since ultimately we consider $c_1$ in the mean square, there is no issue with convergence. To compute the above integral, we must transfer derivatives in $x$ on the stochastic forcing terms in $\hat{\boldsymbol{G}}^{(L)}$ onto known deterministic functions. The first non-zero term in the integrand, which corresponds to $i = 2$, leads to the integral

$$\int^{x_1} \frac{R}{\mu_s}\frac{\partial \delta\Pi_{xx}}{\partial x} B_2\Gamma^{-1}K^{-1}\mathrm{d}x_1 = -\int^{x_1} \delta\Pi_{xx}\frac{\partial}{\partial x}\left(\frac{R}{\mu_s}B_2\Gamma^{-1}K^{-1}\right)\mathrm{d}x_1$$
$$= \int^{x_1} i\alpha\delta\Pi_{xx}\frac{R}{\mu_s}B_2\Gamma^{-1}K^{-1} + \text{H.O.T}\,\mathrm{d}x_1,$$

where we have used the relation $\partial/\partial x = \epsilon\partial/\partial x_1$ to neglect derivatives of slow functions in $x_1$ and the exponential derivative $\partial K^{-1}/\partial x = -i\alpha K^{-1}$. Applying this reasoning to all other streamwise derivatives of forcing terms, we can write the solution for $c_1$ to leading order as

$$c_1(x_1) \propto \int^{x_1} \Gamma^{-1}\left\langle \hat{\boldsymbol{G}}_\alpha^{(L)}, \boldsymbol{B}^{(0)}\right\rangle K(\eta)^{-1}\mathrm{d}\eta,$$

where $\hat{\boldsymbol{G}}_\alpha^{(L)}$ is obtained from $\hat{\boldsymbol{G}}^{(L)}$ by making the transformation $\partial/\partial x \to i\alpha$.

## A.4 Non-parallel effects: Case 1, $T_w = 2000$, Air/CP

If the effect of non-parallel boundary layer growth is included into the analysis, the streamwise wavenumber of the discrete mode is determined as $\alpha_{\text{np}} = \alpha + \tilde{\alpha}$, where

$$\tilde{\alpha} = \Gamma^{-1}\left[\left\langle -i\frac{\partial \mathrm{H}_0}{\partial\alpha}\frac{\partial \boldsymbol{A}^{(0)}}{\partial x_1}, \boldsymbol{B}^{(0)}\right\rangle + \left\langle \mathrm{H}_3\boldsymbol{A}^{(0)}, \boldsymbol{B}^{(0)}\right\rangle\right]. \tag{A.4.1}$$

The matrix $\mathrm{H}_3$ contains stream-wise derivates of mean flow quantities and other higher order terms. Its elements can be found in Ref. [35]. The non-parallel correction to, for example, (4.2.17), is obtained by replacing $\alpha$ everywhere by $\alpha_{\text{np}}$.

Figure A.1a illustrates the effect of non-parallel boundary layer growth on $N$-factors for the Mach 10 Air case for $F = 1.40\times10^{-5}$ and $\beta = 0$. The CP case is also included for comparison. Open circles indicate $N_{\max}$ in each case. These values are, in the order of the legend entries, $N_{\max} = 9.34$, $N_{\max} = 8.82$, and $N_{\max} = 8.97$. Figure A.1b shows $(cK)_{\text{rms}}$ for the same three cases. Notably, when non-parallel effects are included, the neutral point of the mode changes dramatically from $R \approx 6955$ to

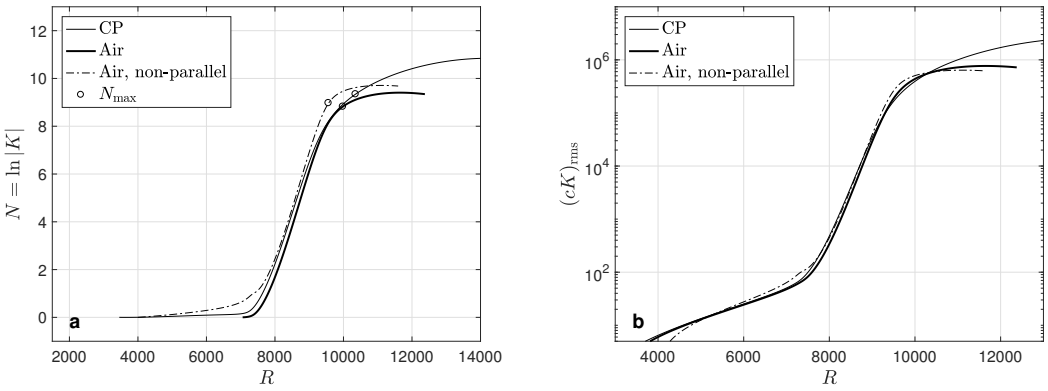


FIGURE A.1. (a) $N$-factors with $N_{\max}$ indicated by open circles and (b) the quantity $(cK)_{\text{rms}}$ as a function of observation Reynolds number for Mach 10, Air.

$R \approx 2850$. Still, the non-parallel correction increases the N-factor for Air by only about 6%. Interestingly, even as the nonparallel correction increases amplification at the observation point, it simultaneously decreases overall receptivity. As a result, the net effect on $(cK)_{\text{rms}}$ is negligible, as can be seen in Figure A.1b.

# References


[1] Balakumar, P. Receptivity of a supersonic boundary layer to acoustic disturbances. *AIAA J. 47*, 5 (2009), 1069–1078.

[2] Balakumar, P., and Kegeris, M. Receptivity of hypersonic boundary layers to acoustic and vortical disturbances. AIAA Paper 2011–371, 2011.

[3] Balakumar, P., and Kegerise, M. Receptivity of hypersonic boundary layers over straight and flared cones. Aiaa paper 2010-1065, 2010.

[4] Bamieh, B., and Dahleh, M. Energy amplification in channel flows with stochastic excitation. *Phys. Fluids 13*, 3258-3268 (2001).

[5] Bender, C., and Orszag, S. *Advanced Mathematical Methods for Scientists and Engineers: Asymptotic Methods and Perturbation Theory*. Springer, 1978.

[6] Betchov, R. Thermal agitation and turbulence. In *Proc. Second Intern. Symp. Rarified Gas Dynamics* (New York, 1961), Academic Press, pp. 308–321.

[7] Bhattacharjee, A. K., Balakrishnan, K., Garcia, A. L., Bell, J. B., and Donev, A. Fluctuating hydrodynamics of multispecies reactive mixtures. *J. Chem. Phys. 142*, 224107 (2015).

[8] Bitter, N. P., and Shepherd, J. E. Stability of highly cooled hypervelocity boundary layers. *J. Fluid Mech. 778* (2015), 586–620.

[9] Bouthier, M. Stabilité lineairé des écoulements presque paralléles. *J. de Mecanique 11*, 4 (1972), 599–621.

[10] Choudhari, M. Boundary-layer receptivity due to distributed surface imperfections of a deterministic or random nature. *Theoret. Comput. Fluid Dynamics 4*, 4 (1993), 101–117.

[11] Choudhari, M. Distributed acoustic receptivity in laminar flow control configurations. *Phys. Fluids 6* (1994), 489–506.

[12] Choudhari, M. Receptivity. In *The handbook of fluid dynamics*, R. W. Johnson, Ed. CRC Press, 1998, pp. 13–40.

[13] Chuvakhov, P. V., and Fedorov, A. Spontaneous radiation of sound by instability of a highly cooled hypersonic boundary layer. *J. Fluid Mech. 805* (2016), 188–206.

[14] Cohen, E. G. D. *Fundamental Problems in Statistical Mechanics*, e. g. d. cohen ed., vol. 1. North-Holland, Amsterdam, 1962.

[15] de Groot, S. R., and Mazur, P. *Non-equilibrium thermodynamics*. Dover Publications, 1984.

[16] de Zarate, J. M. O., and Sengers, J. V. Nonequilibrium velocity fluctuations and energy amplification in planar couette flow. *Phys. Rev. E 79*, 046308 (2009).

[17] Donev, A., de la Fuente, A., Bell, J. B., and Garcia, A. L. Diffusive transport by thermal velocity fluctuations. *Phys. Rev. Lett. 106*, 20 (2011).

[18] Donev, A., de la Fuente, A., Bell, J. B., and Garcia, A. L. Enhancement of diffusive transport by nonequilibrium thermal fluctuations. *JSTAT 2011*, P06014 (2011).

[19] Edwards, L. D., and Tumin, A. Model of distributed receptivity to kinetic fluctuations in high-speed boundary layers. *AIAA J.* (2019).

[20] Edwards, L. D., and Tumin, A. M. Real gas effects on receptivity to kinetic fluctuations. AIAA Paper 2017 – 0070, 2017.

[21] Egorov, I., Fedorov, A., and Soudakov, V. Receptivity of a hypersonic boundary layer over a flat plate with a porous coating. *J. Fluid Mech. 601* (2008), 165–87.

[22] El-Hady, N. M. On the stability of three-dimensional, compressible nonparallel boundary layers. AIAA Paper 80–1374, 1980.

[23] Farrell, B., and Ioannou, P. Stochastic forcing of the linearized navier-stokes equations. *Phys. Fluids A 5*, 2600-2609 (1993).

[24] Fedorov, A. V. *Generation and Development of instability waves in a boundary layer of a compressible gas*. Phd thesis, Moscow Institute of Physics and Technology, 1982. (in Russian).

[25] Fedorov, A. V. Excitation of Tollmien-Schlichting waves by acoustic disturbances in a compressible boundary layer. In *Laminar-Turbulent Transition* (1985), V. V. Kozlov, Ed., Springer, pp. 249 – 254. IUTAM Symposium, Novosibirsk/USSR, 1984.

[26] Fedorov, A. V. Receptivity of hypersonic boundary layer to acoustic disturbances scattered by surface roughness. AIAA Paper 2003–3731, 2003.

[27] Fedorov, A. V. Transition and stability of high-speed boundary layers. *Ann. Rev. Fluid Mech. 43* (2011), 79–95.

[28] Fedorov, A. V. Applications of the mack amplitude method to transition predictions in high-speed flows. RTO-MP-AVT-200, Paper No. 6, 2012.

[29] Fedorov, A. V. Receptivity of high-speed boundary layer to solid particulates. *J. Fluid Mech. 737* (2013), 105–131.

[30] Fedorov, A. V. Prediction and control of laminar-turbulent transition in high-speed boundary-layer flows. In *High-Speed Boundary-Layer Flows, IUTAM ABCM Symposium on Laminar-Turbulent Transition, Procedia IUTAM* (2015), vol. 14, pp. 3–14.

[31] Fedorov, A. V., and Averkin, A. N. Receptivity of a compressible boundary layer to kinetic fluctuations. In *Seventh IUTAM Symposium on Laminar-Turbulent Transition, IUTAM Bookseries* (2010), P. Schlatter and D. S. Henningson, Eds., vol. 18, Springer, pp. 485 – 488.

[32] Fedorov, A. V., and Khokhlov, A. P. Excitation of unstable modes in a supersonic boundary layer. *Fluid Dyn. 25* (1990), 531–537.

[33] Fedorov, A. V., and Khokhlov, A. P. Excitation of unstable modes in a supersonic boundary layer by acoustic waves. *Mekhanika Zhidkosti i Gaza*, 4 (1991), 67–74.

[34] Fedorov, A. V., and Khokhlov, A. P. Prehistory of instability in a hypersonic boundary layer. *Theoret. Comput. Fluid Dynamics 14* (2001), 359–375.

[35] Fedorov, A. V., and Khokhlov, A. P. Receptivity of hypersonic boundary layer to wall disturbances. *Theoret. Comput. Fluid Dynamics 15*, 4 (2002), 231–254.

[36] Fedorov, A. V., and Kozlov, M. Receptivity of high-speed boundary layer to solid particulates. AIAA Paper 2011–3925, 2011.

[37] Fedorov, A. V., and Tumin, A. M. Initial-value problem for hypersonic boundary-layer flows. *AIAA J. 41*, 3 (March 2003).

[38] Fedorov, A. V., and Tumin, A. M. High-speed boundary-layer instability: Old terminology and a new framework. *AIAA J. 49*, 8 (2011), 1647–1657.

[39] Fedorov, A. V., and Tumin, A. M. Receptivity of high-speed boundary layers to kinetic fluctuations. *AIAA J. 55*, 7 (2017), 2335 – 2348.

[40] Gaponov, S. A. Influence of nonparallel flow on the development of disturbances in a supersonic boundary layer. *Fluid Dynamics 15* (1980), 195–199.

[41] Gaster, M. On the effects of boundary layer growth on flow stability. *J. Fluid Mech. 66* (1974), 465–480.

[42] Grabert, H. Fokker-planck equation approach to fluctuations about nonequilibrium steady states. *J. Stat. Phys. 26*, 113 (1981).

[43] Gupta, R. N., Yos, J. M., Thompson, R. A., and Lee, K.-P. A review of reaction rates and thermodynamic and transport properties for an 11 species air model for chemical and thermal nonequilibrium calculations to 30 000 k. NASA Reference Publication 1232, 1990.

[44] Guschin, V. R., and Fedorov, A. V. Asymptotic analysis of inviscid perturbations in a supersonic boundary layer. *J. Appl. Mech. Tech. Phys. 30*, 1 (1989), 64–70.

[45] Guschin, V. R., and Fedorov, A. V. *Excitation and Development of Unstable Disturbances in Supersonic Boundary Layer*, vol. Vol. 25. Fluid Dynamics, 1990.

[46] Keizer, J. A theory of spontaneous fluctuations in viscous fluids far from equilibrium. *Phys. Fluids 21* (1978), 198–208.

[47] Kim, C., Nonaka, A., Bell, J., Garcia, A., and Donev, A. Fluctuating hydrodynamics of reactive liquid mixtures. *J. Chem. Phys. 149*, 084113 (2018).

[48] Klentzman, J., and Tumin, A. M. Stability and receptivity of high speed boundary layers in oxygen. AIAA Paper 2013 - 2882, 2013.

[49] Klentzman, J., and Tumin, A. M. The second mode in high-enthalpy boundary layers in chemical non-equilibrium. In *High-Speed Boundary-Layer Flows, IUTAM ABCM Symposium on Laminar-Turbulent Transition, Procedia IUTAM* (2015), vol. 14, pp. 3–14.

[50] Klimontovich, Y. L. *Statistical Physics*. Harwood Academic Publ., Amsterdam, The Netherlands, 1986.

[51] Klimontovich, Y. L. *Statistical Theory of Open Systems: A Unified Approach to Kinetic Description of Processes in Active Systems*, vol. 1. Kluwer Academic, Norwell, MA, 1995.

[52] Kondepudi, D., and Prigogine, I. *Modern Thermodynamics: From heat engines to dissipative structures*, 2 ed. John Wiley & Sons, 2015.

[53] Kubo, R. Statistical-mechanical theory of irreversible processes. i. general theory and simple applications to magnetic and conduction problems. *J. Phys. Soc. Jpn. 12* (1957), 570–586.

[54] Landau, L. D., and Lifshitz, E. M. Hydrodynamic fluctuations. *Soviet physics, JETP 5* (1957), 512–513.

[55] Landau, L. D., and Lifshitz, E. M. *Statistical Physics*, 3rd ed., vol. 5. Elsevier, 1980.

[56] Li, F. F., Choudhari, M., Chang, C.-L., Kimmel, R., and Adamczak, D. Supersonic and hypersonic quiet tunnel technology at nasa langley. AIAA Paper 2011–3414, 2011.

[57] Lifshitz, E. M., and Pitaevskii, L. P. *Statistical Physics*, vol. 9. Butterworth-Heinemann, 1980.

[58] Luchini, P. Receptivity to molecular agitation in boundary-layer transition. In *Bulletin of the American Phisical Society* (2008), vol. 53, pp. 179 – 180.

[59] Luchini, P. The role of microscopic fluctuations in transition prediction. arXiv:0804.20671v1, physics.flu-dyn., 13 Apr 2008.

[60] Luchini, P. A thermodynamic lower bound on transition-triggering disturbances. In *Seventh IUTAM Symposium on Laminar-Turbulent Transition, IUTAM Bookseries* (2010), P. Schlatter and D. S. Henningson, Eds., vol. 18, Springer, pp. 11 – 18.

[61] Luchini, P. Receptivity to thermal noise of the boundary layer over a swept wing. *AIAA J. 55*, 1 (2017), 121 – 130.

[62] Luchini, P., and Bottaro, A. Adjoint equations in stability analysis. *Ann. Rev. Fluid Mech. 46* (2014), 493 – 517.

[63] Luna, K., and Tumin, A. Receptivity of high-speed boundary layers in binary mixture of gases to kinetic fluctuations. AIAA Paper 2019-1382, 2019.

[64] Ma, Y., and Zhong, X. Receptivity of a supersonic boundary layer over a flat plate. part 1: wave structures and interactions. *J. Fluid Mech. 488* (2003), 31–78.

[65] Ma, Y., and Zhong, X. Receptivity of a supersonic boundary layer over a flat plate. part 2: receptivity to freestream sound. *J. Fluid Mech. 488* (2003), 79–121.

[66] Ma, Y., and Zhong, X. Receptivity of a supersonic boundary layer over a flat plate. part 3: effects of different types of free-stream disturbances. *J. Fluid Mech. 532* (2005), 63–109.

[67] Mack, L. M. *Boundary Layer Stability Theory*, vol. JPL Rept. 900-277. Jet Propulsion Lab., California Inst. of Technology, Pasadena, CA, 1969.

[68] Mack, L. M. Transition and laminar instability. NASA-CP-153203, 1977.

[69] Mack, L. M. Boundary-layer linear stability theory. Agard rep. 709, spec. course stab. transit. laminar flows, 1984.

[70] Malik, M. B. Prediction and control of transition in supersonic and hypersonic boundary layers. *AIAA J. 27*, 1487-93 (1989).

[71] Malik, M. B. Boundary-layer transition prediction toolkit. Aiaa paper 1997-1904, 1997.

[72] Malik, M. R. Numerical methods for hypersonic boundary layer stability. *J. Comput. Phys. 86* (1990), 376–413.

[73] Morkovin, M. V. Critical evaluation of transition from laminar to turbulent shear layers with emphasis on hypersonically travelling bodies. US Air Force Flight Dynamics laboratory, WPAFB, AFFDL-TR, 68-149, 1969.

[74] Morkovin, M. V., Reshotko, E., and Herbert, T. Transition in open flow systems – a reassessment. *Bull. A. Phys. Soc. 39* (1994), 1882.

[75] Nayfeh, A. H. Stability of three-dimensional boundary layers. *AIAA J. 18* (1980), 406–416.

[76] Nayfeh, A. H., Saric, W. S., and Mook, D. T. Stability of nonparallel flows. *Arch. Mech. 26*, 3 (1974), 401–404.

[77] Nonaka, A., Sun, Y., Bell, J. B., and Donev, A. Low mach number fluctuating hydrodynamics of binary liquid mixtures. *Comm. App. Math. and Comp. Sci. 10*, 2 (2015).

[78] Ortiz de Zarate, J. M., and Sengers, J. V. *Hydrodynamic fluctuations in fluids and fluid mixtures*. Elsevier, 2006.

[79] Ortiz de Zarate, J. M., and Sengers, J. V. Hydrodynamic fluctuations in laminar fluid flow i. fluctuating orr-somerfeld equation. *J. Stat Phys. 144* (2011), 774–792.

[80] Ortiz de Zarate, J. M., and Sengers, J. V. Hydrodynamic fluctuations in laminar fluid flow i. fluctuating squire equation. *J. Stat Phys. 150* (2013), 540–558.

[81] Padhaye, A. R., and Nayfeh, A. H. Nonparallel stability of three-dimensional flows. AIAA Paper 79–1281, 1979.

[82] Reed, H. L., Saric, W. S., and Arnal, D. Linear stability theory applied to boundary layers. *Ann. Rev. Fluid Mech. 28*, 389-428 (1996).

[83] Reshotko, E. Transition issues at hypersonic speeds. Aiaa paper 2006-707, 2006.

[84] Reshotko, E. Transition issues for atmospheric entry. *J. Spacecraft and Rockets 45* (2008), 161–164.

[85] Ronis, D., Procaccia, I., and Matcha, J. Statistical mechanics of stationary states. vi. hydrodynamic fluctuation theory far from equilibrium. *Phys. Rev. A 22*, 714 (1980).

[86] Saric, W. S., and Nayfeh, A. H. Nonparallel stability of boundary-layer flow. *Phys. Fluids 18*, 8 (1975), 945–950.

[87] Saric, W. S., and Nayfeh, A. H. Nonparallel stability of boundary layers with pressure gradients and suction. Tech. Rep. AGARD, TR CP-224, 1977.

[88] Saric, W. S., Reshotko, E., and Arnal, D. Hypersonic laminar-turbulent transition. Agrd ar-391, vol. 2, hypersonic experimental and computational capability, improvement and validation.

[89] Schlichting, H., and Gersten, K. *Boundary-Layer Theory*, 9th ed. Springer, 2017.

[90] Schmitz, R., and Cohen, E. G. D. Fluctuations in a fluid under a stationary heat flux. i. general theory. *J. Stat. Phys. 39* (1985), 285–316.

[91] Schmitz, R., and Cohen, E. G. D. Fluctuations in a fluid under a stationary heat flux. ii. slow part of the correlation matrix. *J. Stat. Phys. 40* (1985), 431–316.

[92] Schneider, S. P. Flight data for boundary-layer transition at hypersonic and supersonic speeds. *Journal of Spacecraft and Rockets 36*, 1 (1999), 8–20.

[93] Schneider, S. P. Hypersonic laminar-turbulent transition on circular cones and scramjet forebodies. *Prog. Aerosp. Sci. 40*, 1 (2004), 1–50.

[94] Schneider, S. P. Laminar-turbulent transition on reentry capsules and planetary probes. *J. Spacecraft and Rockets 43*, 6 (2006), 1153–73.

[95] Schneider, S. P. The development of hypersonic quiet tunnels. *J. Spacecraft and Rockets 45*, 4 (2008), 641–664.

[96] Schneider, S. P. Summary of hypersonic boundary-layer transition experiments on blunt bodies with roughness. *J. Spacecraft and Rockets 45*, 6 (2008), 1090–105.

[97] Sengers, J. V., and de Zarate, J. M. O. Velocity fluctuations in laminar fluid flow. *J. Non-Newtonian Fluid Mech. 165*, 925-931 (2010).

[98] Stetson, K., and Kimmel, R. On hypersonic boundary-layer stability. AIAA Paper 1992-0737, 1992.

[99] Swift, J., and Hohenberg, P. Hydrodynamic fluctuations at the convective instability. *Phys. Rev. A 15*, 319 (1977).

[100] Tumin, A. M. Three-dimensional spatial normal modes in compressible boundary layers. *J. Fluid Mech. 586* (2007), 295–322.

[101] Tumin, A. M. The biorthogonal eigenfunction system of linear stability equations: a survey of applications to receptivity problems and to analysis of experimental and computational results. AIAA Paper 2011–3244, 2011.

[102] Tumin, A. M., and Fedorov, A. V. On the weakly nonparallel flow effect on characteristics of flow stability. *Uchenye Zapiski TsAGI 13*, 6 (1982), 91–96. (in Russian).

[103] Tumin, A. M., Wang, X., and Zhong, X. Direct numerical simulation of receptivity in a hypersonic boundary layer: validation. AIAA Paper 2006–1108, 2006.

[104] Tumin, A. M., Wang, X., and Zhong, X. Direct numerical simulation and the theory of receptivity in a hypersonic boundary layer. *Phys. Fluids 19*, 1 (2007). paper 014101.

[105] W. S. Saric, H. L. Reed, E. J. K. Boundary-layer receptivity to freestream disturbances. *Ann. Rev. Fluid Mech. 34* (2002), 291–319.

[106] Wong, R. *Asymptotic Approximations of Integrals*. SIAM, Philadelphia, 2001.

[107] Wu, X. Generation of Tollmien-Schlichting waves by convective gusts interacting with sound. *J. Fluid Mech. 397* (2011), 285–316.

[108] Zaitsev, V., and Shliomis, M. Hydrodynamic fluctuations near the convection threshold. *Soviet physics, JETP 32*, 866 (1971).

[109] Zavolskii, N. A., and Reutov, V. P. Thermal excitation of waves in a boundary layer. *Fluid Dynamics 18* (1983), 701–705.

[110] Zavol'skii, N. A., Reutov, V. P., and Rybushkina, G. V. Generation of Tollmien-Schlichting waves via scattering of acoustic and vortex perturbations in boundary layer on wavy surface. *J. Appl. Mech. Tech. Phys. 24* (1983), 355–361.

[111] Zhigulev, V. N., and Fedorov, A. V. Boundary layer receptivity to acoustic disturbances. *J. Appl. Mech. Tech. Phys. 28* (1987), 28–34.

[112] Zubarev, D. N., and Morozov, V. G. Statistical mechanics of nonlinear hydrodynamic fluctuations. *Physica A 120* (1983), 411–467.

[113] Zuccher, S., and Luchini, P. Boundary layer receptivity to external disturbances using multiple scales. *Meccanica 49*, 2 (2014), 441– 467.